Universidade de Aveiro
2013
Departamento de Engenharia de Materiais e Cerâmica

Styliani Skiadopoulou

Multiferroic Behaviour of Bismuth Ferrite Porous Thin Films

Universidade de Aveiro
2012

Departamento de Engenharia de Materiais e Cerâmica

Styliani Skiadopoulou

Multiferroic Behaviour of Bismuth Ferrite Porous Thin Films

Comportamento Multiferroico de Filmes Finos Porosos de Ferrite de Bismuto

Dissertation presented to University of Aveiro to obtain the Mater degree in Materials Engineering, under the scientific guidance of Dr. Paula Celeste da Silva Ferreira, Auxiliary researcher of Centre for Research in Ceramics and Composite Materials of the University of Aveiro and Prof. Paula Maria Lousada Silveirinha Vilarinho, Associated Professor of the Department of Materials and Ceramics Engineering of University of Aveiro, Portugal.

Dissertação apresentada à Universidade de Aveiro para cumprimento dos requisitos necessários à obtenção do grau de Mestre em Engenharia de Materiais, realizada sob a orientação científica da Professora Doutora Paula Ferreira e da Professora Doutora Paula Vilarinho do Departamento de Engenharia de Materiais e Cerâmica da Universidade de Aveiro

Financial support from FCT and FEDER (QREN-COMPETE) of the project PTDC/CTM/098130/2008.

I dedicate this work to my family, for they always are my source of inspiration…

The board of Examiners

president

Prof. Dr. Jorge Ribeiro Frade
Professor at University of Aveiro

Prof. Ana Maria de Oliveira e Rocha Senos
Associate Professor at University of Aveiro

Prof. Brian Rodriguez
Professor at University College Dublin

Dr. Paula Celeste da Silva Ferreira
Post-Doctoral Research Assistant at CICECO-Centre for Research in Ceramics & Composite Materials, University of Aveiro (Supervisor)

Prof. Dr. Paula Maria Lousada Silveirinha Vilarinho
Associate Professor at University of Aveiro (Co-supervisor)

Acknowledgements

Most importantly, I would like to thank my supervisors, Dr. Paula Ferreira and Prof. Paula Vilarinho, for the support and faithful dedication in this work. Furthermore, I'm grateful for being part of the FCT financed project PTDC/CTM/098130/2008.

Thank you to Marta Ferro from the Microscopy Laboratory of the Department of Materials and Ceramics Engineering for her guidance and support during the Scanning Electron Microscopy sessions.

I would like to thank Dr. Liliana Ferreira from Physics Department of Faculty of Science of University of Lisbon for the magnetic characterization.

In particular, I would like to thank Alichandra Castro for her support in XRD analyses, Scanning Electron Microscopy and principally the endless hours of inspiring discussions.

I would also like to thank Carla Silva for the moral support and the suggestions of smart solutions at difficult times.

Lastly, I would like to thank my father, mother and sister who are always there for me, an enormous source of inspiration and cheerfulness.

keywords Multiferroic porous films, sol-gel, dip-coating, piezoresponse force microscopy

abstract

An enormous contribution in the scientific community of material engineering is being made by the exceptionally rapid evolution of the field of multifunctional materials. Multiferroics combine simultaneously at least two of the three ferroic properties: ferroelectricity, ferromagnetism and ferroelasticity. Magnetoelectric multiferroics' ability of magnetic field manipulation via electric fields or vice versa can be extremely promising for information storage applications, leading to thinner, as well as flexible devices, with significantly high energetic efficiencies and elevated capacities.

The aim of this work is the preparation and characterization of bismuth ferrite porous thin films, having as further objective to be able to serve as matrices for future functionalization. The strategy of this work consists of: a) dense film preparation with varying deposition velocities, b) porous film preparation with varying solution template quantities, inorganic precursor concentration and deposition velocities. Annealing temperature studies were also required, for the obtainment of the desired properties and control of microstructure. The methodologies for the film preparation in use were: a) sol-gel process, b) Evaporation Induced Self-Assembly (EISA), for the induction of porosity, and c) dip-coating technique.

A series of dense films with varying deposition velocities were produced, serving as means of comparison for the porous thin films. Increasing the sol-gel deposition velocity led to increasing thickness. Piezoresponse Force Microscopy (PFM) characterization was conducted, revealing the expected ferroelectric domains. By the same technique, local piezoelectric hysteresis loops were obtained, showing increase of polarization saturation with increasing thickness. Lastly, magnetic moment measurements were carried out by the use of Superconducting Quantum Interference Device (SQUID), presenting decrease of remnant magnetization with increasing thickness.

Varying template concentration was introduced in order to obtain a homogenous porous network. Homogeneity and lack of cracks in the films were successfully achieved, by decreasing solution template mass, for a given solution concentration. Thermal treatment studies revealed loss of porous network ordering at elevated annealing temperatures, required for the obtainment of crystallization and enhanced multiferroic properties. Local piezoelectric hysteresis loops showed increase of the effective piezoelectric coefficient with increasing thickness. SQUID characterization presented increasing remnant magnetization with increasing porosity. Lastly, increasing inorganic precursors concentration resulted in better control of porosity order and increase in the piezoelectric coefficient.

palavras-chave

Filmes porosos multiferroicos, sol-gel, dip-coating, microscopia de força de piezoresposta

resumo

Uma enorme contribuição na comunidade científica da Engenharia de Materiais tem sido feita pela evolução excecionalmente rápida no âmbito dos materiais multifuncionais. Os multiferróicos combinam simultaneamente pelo menos duas das três propriedades ferróicas: ferroeletricidade, ferromagnetismo e ferroelasticidade. Os multiferróicos magnetoelétricos que permitem a manipulação do campo magnético através do campo elétrico e vice versa são extremamente promissores para aplicações de armazenamento de informação, levando a dispositivos mais finos e flexíveis com eficiência energética significativamente mais alta e elevadas capacidades.

O objetivo deste trabalho é a preparação e caracterização de filmes porosos de ferrite de bismuto, com vista a serem capazes a uma futura funcionalização. A estratégia deste trabalho consiste: a) preparação de filme denso variando a velocidade de deposição, b) preparação de filme poroso variando o *template* da solução concentração do precursor inorgânico, e velocidades de deposição. Os estudos sobre temperatura de calcinação são também necessários, para a obtenção das propriedades requeridas e o controlo da microestrutura. As metodologias para a preparação dos filmes foram: a) sol-gel, b) *Evaporation Induced Self-Assembly*, para a indução da porosidade, e c) *dip-coating*.

Foi preparada uma série de filmes densos variando a velocidade de deposição, servindo como meio de comparação para os filmes porosos. Aumento da velocidade de deposição resulta em aumento da espessura dos filmes. Foi utilizada a caracterização por *piezoresponse force microscopy* (PFM), revelando domínios ferroelétricos como esperado. Pela mesma técnica, foram obtidas curvas de histerese piezoelétricas locais mostrando o aumento da saturação da polarização com o aumento da espessura. Por fim, as medidas dos momentos magnéticos foram obtidos através do *Superconducting Quantum Interference Device* (SQUID), apresentando uma diminuição da magnetização remanescente com o aumento da espessura.

A variação da concentração do *template* foi introduzida de modo a obter uma porosidade homogénea. A homogeneidade e ausência de fissuras nos filmes foi conseguida com sucesso pela diminuição da massa do *template* da solução, para uma determinada concentração da solução. Os estudos do tratamento térmico revelou a perda da porosidade ordenada para temperaturas mais elevadas, necessárias para a obtenção da cristalização e melhoria das propriedades multiferróicas. As curvas de histerese piezoelétrica local mostraram um aumento do coeficiente efetivo piezoelétrico com o aumento da espessura. A caracterização por SQUID apresentou um aumento da magnetização remanescente com o aumento da porosidade. Por fim, o aumento da concentração dos precursores inorgânicos resulta em um melhor controlo da ordem da porosidade e aumento do coeficiente piezoelétrico.

TABLE OF CONTENTS

INDEX OF FIGURES

INDEX OF TABLES

ABBREVIATIONS

AFM	Atomic Froce Microscopy
BFO	Bismuth Ferrite
EISA	Evaporation Self-Induced Assembly
EtOH	Ethanol
ME	Magnetoelectric
MFM	Magnetic Force Microscopy
PFM	Piezoresponse Force Microscopy
PS-b-PEO	Polystyrene-Poly(ethylene oxide)
SEM	Scanning Electron Microscopy
STM	Scanning Tunneling Microscopy
SQUID	Superconductor Quantum Interference Device
THF	Tetrahydrofuran
XRD	X-Ray Diffraction

CHAPTER 1

Introduction

1. Introduction

1.1 Objectives

Porous matrices have a great importance for a large range of applications. Firstly, the presence of porosity can provide lighter devices. In addition, novel architectures can be achieved by the incorporation of diverse materials in the pores, producing multifunctional films. Importantly, these structures are ideal for the field of sensors and actuators, since porosity confers enhanced pyroelectric properties, by decreasing the dielectric constant, which results in increase in the figure of merit.[1,2] Lastly, for the case of antiferromagnetic materials, the high surface area owing to the porous network can result in elevated magnetization.[3,4]

This thesis aims at understanding the effect of porosity and thickness on the multiferroic properties of Bismuth Ferrite ($BiFeO_3$, BFO) thin films. For this purpose, a series of BFO films were prepared, with varying porosity and thickness, having as a starting and comparison point dense and relatively thick films (~300nm).

Films were prepared via a sequence of simple and low cost processes: sol-gel, Evaporation Induced Self-Assembly (EISA) and dip-coating for the deposition of the films on silicon platinised substrates. The porosity was tailored by the polymer and inorganic precursors concentration. Processing variables, as deposition, drying and annealing temperatures, were modified for maximized control of the microstructure and properties.

1.2 Structure of the Thesis

The thesis consists of 5 chapters. Chapter 2 is dedicated to the State of the Art, the fundamental theories and ideas, which led to the definition of the experimental strategy. Chapter 3 comprises the detailed description of the experimental and the characterization procedure used along this work. In Chapter 4, a comprehensive discussion of the obtained results is conducted. Finally, in Chapter 5, general conclusions and proposed future work are presented.

CHAPTER 1 Introduction

CHAPTER 2

State of the Art

2. State of the Art

2.1 Microelectronics

If 50 years took us to get from the room-sized computer of the 60's to the 9 mm-thick ultra-books of the 00's, we are just on the threshold of the era of electrically controllable nanoscale storage, which will lead to thinner, lighter, portable and flexible devices, with significantly high energetic efficiencies and huge capacities (**Figure 2.1**).

Figure 2.1 Computer evolution from the 60's up to the 00's, with decreasing cost and dimensions and increasing capacity and velocity (adapted from reference [5]).

An enormous contribution to the scientific community of materials engineering is being made by the exceptionally rapid evolution of the field of multifunctional materials. The limitations of Moore's law, which predicted the exponential increase over time of the number of components in integrated circuits,[6] have led to a high demand for alternatives in the field of microelectronics. Indeed, since 2007 the International Technology Roadmap for Semiconductors [7] has been addressing the concept of functional diversification under the title "More than Moore". As a consequence, the combination of the miniaturization of the components (Moore's law) and the use of novel material architectures ("More than Moore") makes possible the integration of digital and non-digital functionalities into compact systems. Within this context multiferroics hold great promise.

Multiferroics combine simultaneously at least two of the three ferroic properties: ferroelectricity, ferromagnetism and ferroelasticity.[8–11] The magnetoelectric multiferroics offer the ability of magnetic field manipulation via electric fields or vice versa. A wide range of applications, such as information storage, sensing, actuation and spintronics, await pioneering strategies of producing robust magnetoelectric coupling at room temperature.[11]

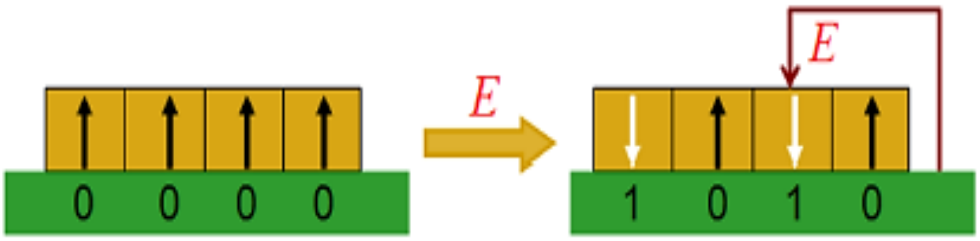

Figure 2.2 Schematic simplification of the electric-driven magnetic recording mechanism in magnetic hard disk drive (adapted from Hu *et al.*[12]).

Data storage, probably the most crucial battlefield of the tough and consuming expedition for miniaturization, is mainly focused on the development of Ferroelectric and Magnetic Random Access Memories (FeRAMs and MRAMs respectively), which have limited efficiencies.[13] The use of multiferroics can provide electrically written and magnetically read devices, thus faster, low-energy consumption and with a non-destructive magnetic read operation.

In **Figure 2.2**, we can observe a simplified example of a magnetoelectric device on a magnetic hard drive disk. By the application of an electric field *E*, opposite magnetization domains are formed on the magnetic hard drive disk, corresponding to 0-1 magnetic bits.[12]

In **Figure 2.3**, a Magnetoelectric Random Access Memory (MERAM) is presented, where an electric field $\boldsymbol{E}$ is applied on the magnetoelectric material (blue), inducing a magnetic moment $\boldsymbol{\Delta m_{ME}}$ which provides a magnetic flux density $\boldsymbol{B}$ through a magnetic phase (grey).[14] A magnetic ‘’bit’’ is written on the moving track of the hard disk, which has a constant velocity $\boldsymbol{v}$. Switching of the magnetization direction corresponds to opposite orientations, thus 0-1 magnetic bit configuration.

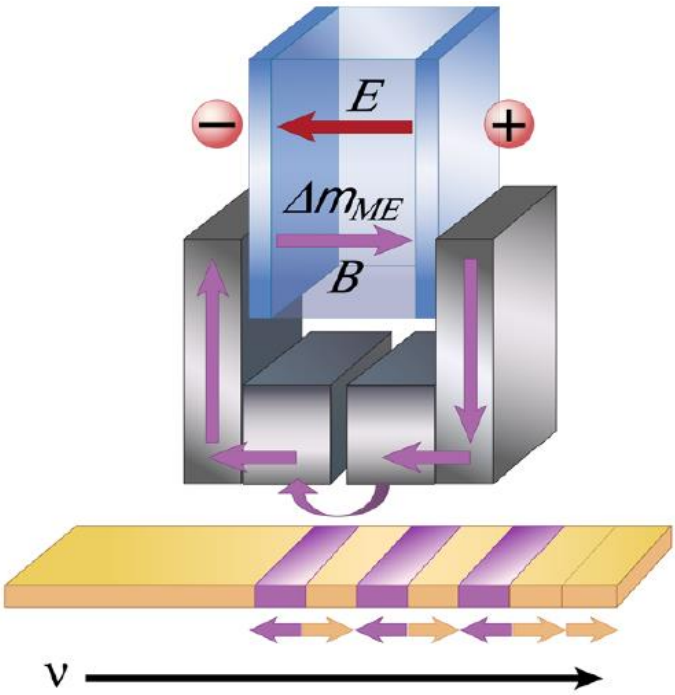

Figure 2.3 Schematic representation of a Magnetolectric Random Access Memory (MERAM).[14]

Lastly, lead-based compounds, due to their excellent ferroelectric properties, have dominated the electronics field through the years. However, lead's high toxicity, in combination with the lack of device recycling, leads to contamination of the soil, air, water and the human and animal population. High levels of lead concentration in the human body can provoke a series of complications, culminating with madness. In addition, lead exposure is very dangerous for children, since it affects the neurodevelopment and it can even provoke lowering of the IQ.[15] For these reasons, the European Union, in 1 July of 2006, banned the use of lead in some electronic equipment, under the Restriction of Hazardous Substances.[16] Therefore, a significant support to a global environmental consciousness has been made lately, propelling a generalized search for lead-free materials for electronic applications.

2.2 Ferroelectrics

Ferroelectrics correspond to insulating systems, which present two or more stable or metastable states of nonzero electric polarization in the absence of electric field, known as spontaneous polarization.[17–20] The polarization in a bulk or film is organized in domains and, by reversing the applied electric field, switching of the domains' orientation takes place. For a finite system, the polarization simply corresponds to the charge density, while for infinite crystalline structures, is the result of the integrated current through the transformation of one variant to another, else known as Berry phase. Ferroelectrics belong to 10 polar point groups, a subcategory of the 20 non-centrosymmetric piezoelectric point groups.[17]

The ferroelectric phenomenon was firstly observed by Valasek in 1920.[19] Initially, the research was limited to the study of hydrogen-bonded materials, such as Rochelle salt (Potassium Sodium Tartrate ($KNaC_4H_6O_6.4H_2O$)) and Monopotassium Phosphate (KH_2PO_4). In 1949, Barium Titanate's ($BaTiO_3$) ferroelectric properties were discovered and the route for understanding ferroelectricity was simplified.

There are various groups of materials that present ferroelectric properties. To name a few: perovskites ($BaTiO_3$, $PbTiO_3$, $BiFeO_3$, $SrTiO_3$), trigonal paraelectrics ($LiNbO_3$), layered oxide ferroelectrics (Aurivillius phases consisting of layered bismuth oxides), other ferroelectric oxide families (tungsten bronzes, boracites), magnetic ferroelectric oxides (hexagonal manganites, such as $YMnO_3$), electronic ferroelectrics ($BaBiO_3$, $LuFeO_4$, $YFeO_4$) and ferroelectric polymers (PVDF, liquid crystals).[17]

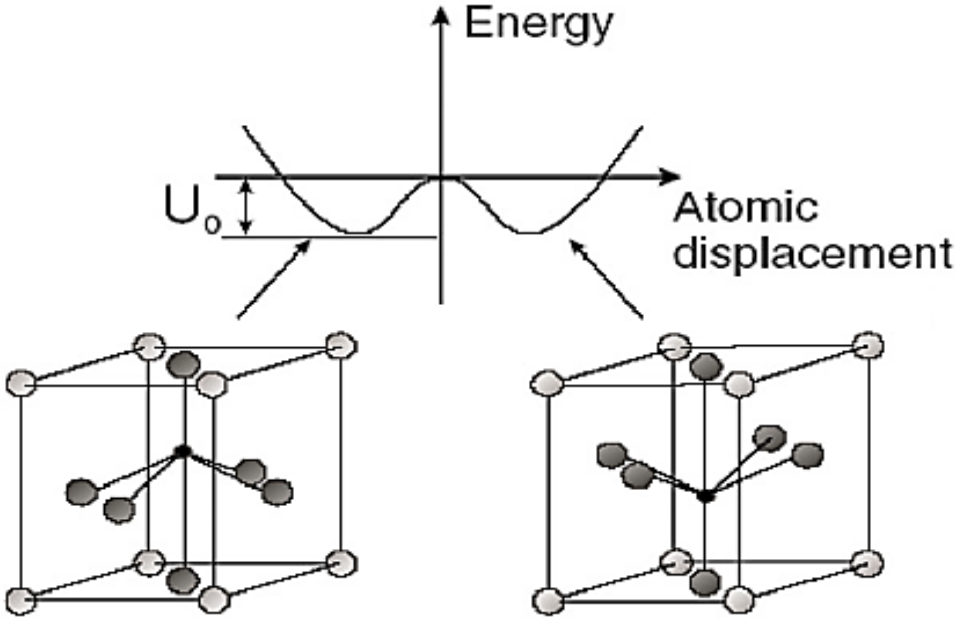

Figure 2.4 Displacement of cation B in the perovskite structure ABO_3 and the respective double-well potential of the two polarization states.[21]

However, the most widely studied and used class of ferroelectrics in industry are the perovskites. Their structure is ABO_3, having cation A at the corners of the unit cell, B at the centre and O at the midpoint of each edge, creating an oxygen octahedra net, with B at the centre of each one of them (**Figure 2.4**). Not all perovskites present ferroelectric properties, since the latter are intimately linked with the size and position of the oxygen octahedra. The ion fitting in a perovskite unit cell can be calculated by Eq.1, known as Goldschmid tolerance factor *t*, which corresponds to the ionic distance between cation A and its closest oxygen divided by the length of the octahedral edge:

$$t = \frac{r_A + r_O}{\sqrt{2}(r_B + r_O)} \qquad \text{Eq. 1}$$

where r_A, r_B and r_O are the radii of the A, B and O ions respectively.[17] Depending on the ionic radii, Eq. 1 yields three cases: cubic structure for $t \approx 1$, hexagonal structures with small polar distortion for $t > 1$ and orthorhombic or rhombohedral structures with strong polar distortion for $t < 1$. As seen in **Figure 2.4**, the vertical displacement of central cation B breaks the symmetry of the cubic structure and, by changing the distribution of charge in the unit cell, provokes polarization.[21] The double-well potential, also shown in **Figure 2.4**, presents the two stable states (lower energy states) of the spontaneous polarization.

An important characteristic of ferroelectrics is the hysteretic behaviour of polarization with the application of an electric field.[22,23] In **Figure 2.5**, an almost ideal case of hysteresis loop is presented. As the electric field is increased, polarization increases until a certain value, which corresponds to the saturation polarization P_S. By removal of the bias voltage, a large part of the polarized regions maintain their distorted positions and, subsequently, at zero field a remanent polarization P_R is reached. The same behaviour is followed for the case of negative bias. The two points where the hysteresis loop meets the voltage axis correspond to the forward and reverse coercive voltages, V^+ and V^- respectively. High values of the coercive field account for easily polarizable materials, which retain their polarization. Finally, the area of the loop provides the work necessary for polarization switching.[22]

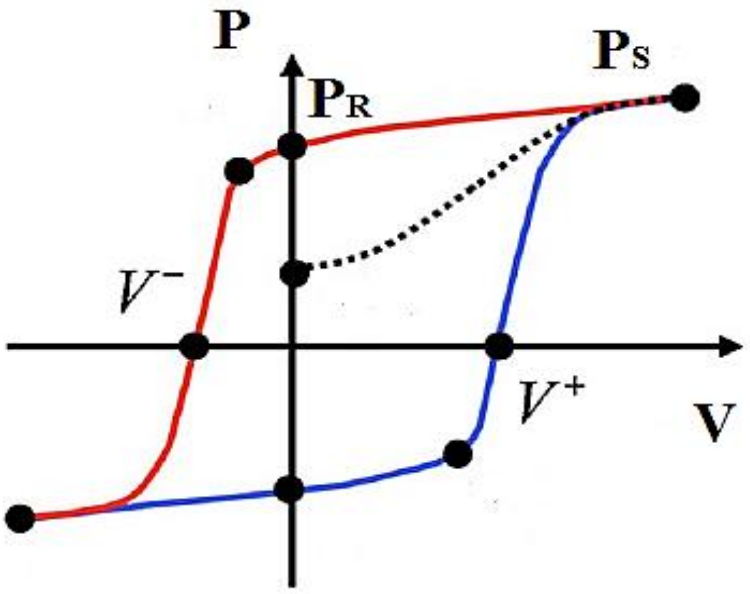

Figure 2.5 Schematic representation of a well-saturated electromechanical hysteresis loop. The two axes represent the applied voltage V and the resulting polarization P. P_S and P_R correspond to the saturation and remanent polarization, whereas V^+ and V^- to the forward and reverse coercive voltage.[22]

2.3 Ferromagnetics

The magnetic behaviour of matter, thus attraction or repulsion of some materials by others, owes its origin to the existence of magnetic moments throughout various material structures.[24] Magnetic moments could be described as small magnets, with polar character. As known by classical electromagnetism, movement of electrically charged elements generates magnetic fields. Therefore, the origin of magnetization (accumulation of magnetic moments in a material) is the orbiting and spinning electrons of the atoms (**Figure 2.6**).

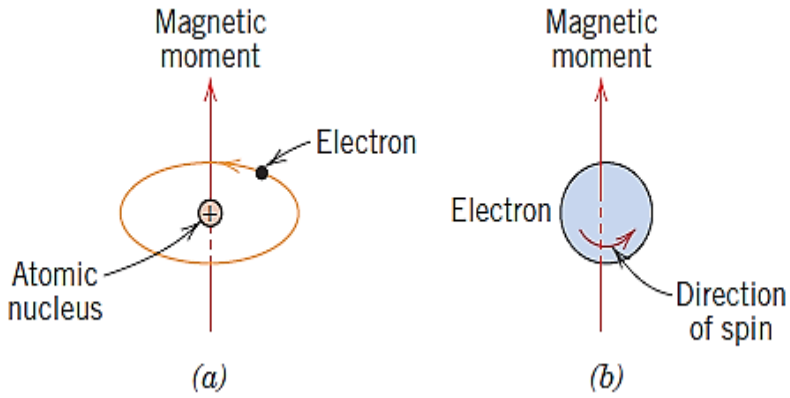

Figure 2.6 The two different origins of magnetic moment: (a) Orbiting electron and (b) Electron spin.[24]

Ferromagnetism is one of the five different existing magnetic behaviours of matter: diamagnetism, paramagnetism, antiferromagnetism, ferromagnetism and ferrimagnetism, as shown in **Figure 2.7** (diamagnetism is not included since no magnetic moments are present with absence of magnetic field).[24,25] Ferromagnets owe their elevated and spontaneous magnetization to aligned magnetic dipoles, which maintain their orientation even when no magnetic field is applied. Paramagnetic materials reveal randomly oriented magnetic moments, thus an approximately zero macroscopic magnetization, which at the presence of a magnetic field are rotated and aligned, resulting in increase of magnetization. Antiferromagnetism corresponds to a zero overall magnetization, since cancellation of the equally distributed antiparallel magnetic moments occurs (**Figure 2.7**). Lastly, ferrimagnetic behaviour is similar to the antiferromagnetic, however, since different ion

types originate the magnetic moments, conferring them different magnitudes, total magnetization is non-zero.

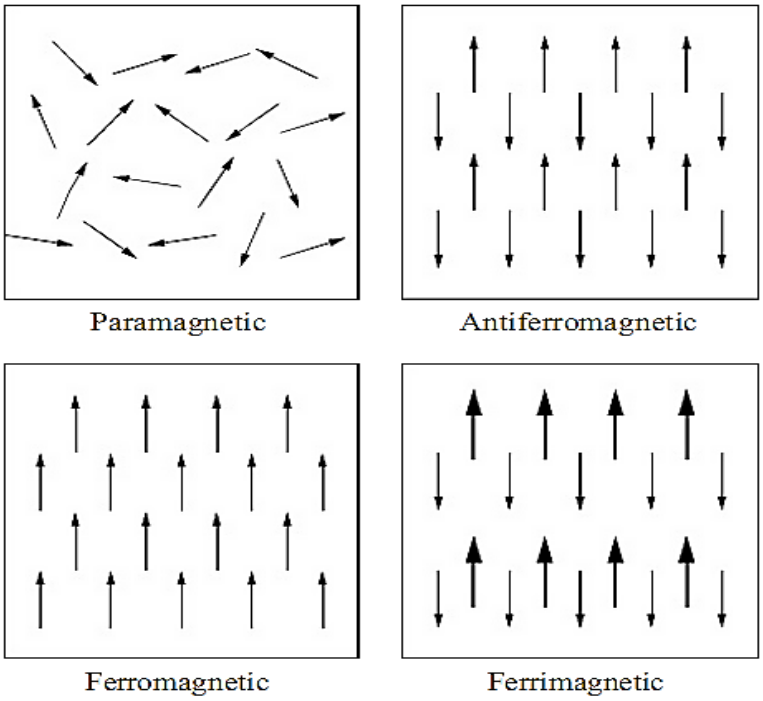

Figure 2.7 The different magnetic states of matter: paramagnetic, antiferromagnetic, ferromagnetic and ferromagnetic.[25]

Like in ferroelectrics, hysteresis loop is an unbreakable proof of the ferromagnetic character. In **Figure 2.8**, magnetic induction *B* (corresponds to the magnetic flux density and is linearly related to the magnetization *M*) is presented as a function of the magnetic field *H* for a ferromagnet and a ferrimagnet.[25] Both loops have hysteretic character. Initially, for zero magnetic field the magnetization is zero. With the increase of *H*, alignment of magnetic moments results in the increase of *B*, reaching a saturation point B_S, when no further alignment is possible. The reverse process provokes a small decrease in *B*, however it never reaches zero, having instead a significant residual magnetization B_r at *H=O*. For negative orientation of *H*, one gets negative orientation of *B*. The coercive magnetic field H_C corresponds to the point at which magnetization is switched, therefore higher H_C means high resistance in demagnetization. The outer loop, presenting larger B_S, B_r and H_C, corresponds to a ferromagnet and the inner one to a ferrimagnet, since magnetic moment cancellation attenuates magnetic behaviour, as discussed above.

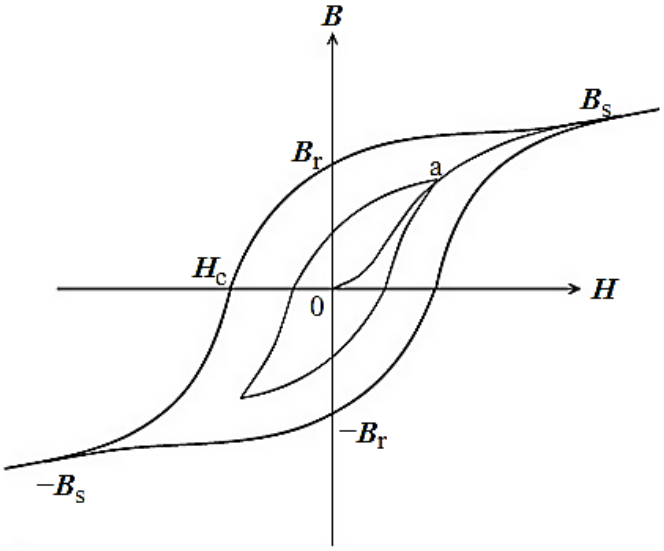

Figure 2.8 Hysteresis loop of a ferromagnetic (outer curve, large saturation and residual magnetic induction, B_s and B_r respectively) and a ferrimagnetic material (inner curve, low saturation and residual magnetic induction, B_s and B_r respectively).[25]

A large variety of ferromagnetic materials have been studied and used for various applications. Apart from the conventional pure metals (Fe, Co, Ni) and rare-earth magnets, a series of compounds present significant ferromagnetic properties, such as the alloy $TbDyFe_2$ (Terfenol-D), the spinels γ-Fe_2O_3, $CoFe_2O_4$ and $NiFe_2O_4$, the corundum α-Fe_2O_3, the manganites $LaSrMnO_3$ and $LaCaMnO_3$ and the magnetic semiconductors, like ZnO and GaN.[9,26]

2.4 Multiferroics

Ferroelectricity, ferromagnetism and ferroelasticity are defined by switching of the alignment of electric dipole-moment, electron spin and strain via electric, magnetic and stress fields, respectively.[11]

Multiferroic materials combine at least two of these three properties.[8–12,27] However, apart from this multifunctional character, multiferroics present the remarkable phenomenon of coupling the different properties, in a sense that the stimulating fields (electric, magnetic and stress) can also provoke the manifestation of the responses which do not correspond to their counterparts (**Figure 2.9**). Consequently, an electric field *E* can induce strain ***ε*** or magnetization *M*, a magnetic field *B* polarization *P* or strain *ε*, and, finally, stress field *σ* polarization *P* or magnetization *M*, certainly depending on the material characteristics.

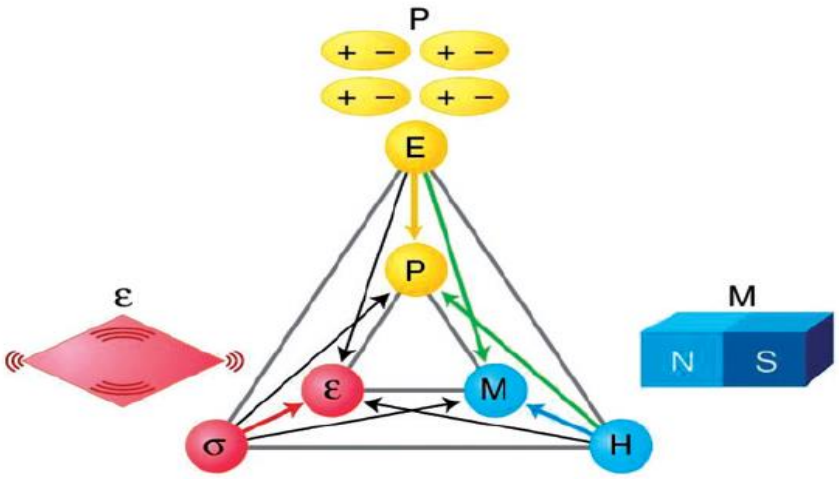

Figure 2.9 Representation of multiferroicity concept, with the different cases of coupling that can occur by the presence of the three different fields: electric, magnetic and stress.[27]

2.4.1 Single-phase

Magnetoelectric multiferroics correspond to the coupling of ferroelectricity and ferromagnetism. In single-phase magnetoelectrics, the multiferroic behaviour is dominated by the linear magnetoelectric effect. In mathematical terms, partial derivation of the free energy of a material F (given by Eq. 2) over the electric E and magnetic field H, results in

the expressions for spontaneous polarization P^S and magnetization M^S, Eq. 3 and Eq. 4 respectively:

$$F(\vec{E},\vec{H}) = F_o - P_i^S E_i - M_i^S H_i - \frac{1}{2}\varepsilon_o \varepsilon_{ij} E_i E_j - \frac{1}{2}\mu_o \mu_{ij} H_i H_j -$$

$$-\frac{1}{2}\beta_{ijk} E_i H_j H_k - \frac{1}{2}\gamma_{ijk} H_i E_j E_k - \ldots \quad \text{Eq. 2}$$

$$P_i(\vec{E},\vec{H}) = -\frac{\partial F}{\partial E_i} = P_i^S + \varepsilon_o \varepsilon_{ij} E_j + \alpha_{ij} H_j + \frac{1}{2}\beta_{ijk} H_j H_k + \gamma_{ijk} H_i E_j - \ldots \quad \text{Eq. 3}$$

$$M_i(\vec{E},\vec{H}) = -\frac{\partial F}{\partial H_i} = M_i^S + \mu_o \mu_{ij} H_j + \alpha_{ij} E_j + \beta_{ijk} H_j E_\iota + \frac{1}{2}\gamma_{ijk} H_i E_j + \ldots \quad \text{Eq. 4}$$

where i,j,k are the spatial coordinates, F_o the ground state free energy, ε_o and μ_o the dielectric and magnetic susceptibilities respectively, α_{ij} the linear magnetoelectric coefficient and β_{ijk} and γ_{ijk} third-order tensor coefficients.[27,28] The latter also can manifest magnetoelectric effect, however of smaller range. The linear magnetoelectric coefficient α_{ij} corresponds to magnetic field-induced polarization or electric field-induced magnetization, as shown in Eq. 5:

$$\alpha_{ij} = \frac{\partial P_i}{\partial H_j} = \frac{\partial M_i}{\partial E_j} \quad \text{Eq. 5}$$

However, contradictory theories concerning their basic physics principles result in a very limited number of magnetoelectrics in nature.[9,11] The main reason for that fact is that ferroelectric properties require strong insulators, whereas ferromagnets are principally conducting metals. Additionally, symmetry breaking in ferroelectrics, thus polarization, is provided by the empty *d* shells, whereas partially filled *d* orbitals of transition metals are responsible for magnetization. Intensive research is being made since the 70s, which has led to a series of recipes for single phase multiferroics.

The most studied case is the perovskite bismuth ferrite ($BiFeO_3$), which falls in the wider group of materials that combine two different cation types with the properties mentioned above. Another group is that of the non-centrosymmetric magnetic ordering which leads to the rise of polarization, even with the presence of atomic centrosymmetricity, such as chromium chrysoberyl (Cr_2BeO_4), terbium manganite ($TbMnO_3$), as well as the manganites $TbMn_2O_5$ and Ca_3CoMnO_6. A combination of polar tilts and rotations of the anionic sublattice which occurs in rare-earth manganites and in

barium nickel fluoride ($BaNiF_4$), also results in symmetry breaking, thus induction of polarization. Finally, attempts to provoke off-centering structures for cations with partially filled *d* orbitals have been made via epitaxial strain.[11]

2.4.2 Composites

Due to the limited number of single-phase multiferroics, great efforts have been made in order to develop composites, whose two or more components will present the desired properties. It has been proved that the magnetoelectric coupling effect in multiferroic composites can be significantly enhanced.[29–34] The architecture of these composites is mainly based in three different heterostructures: horizontal, vertical and particulate (**Figure 2.10**).[8,9]

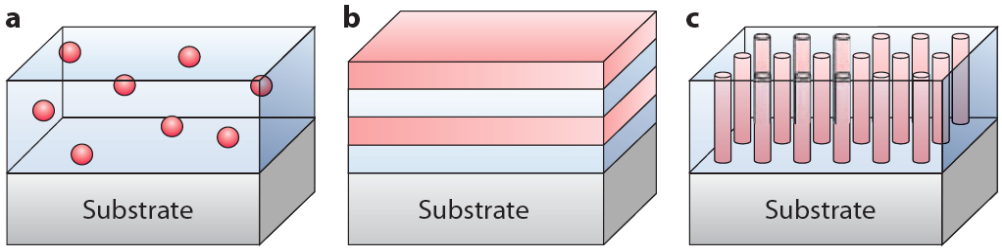

Figure 2.10 Illustration of the three multiferroic composite heterostructures: (a) Particulate, (b) Horizontal and (c) Vertical.[8]

In the last years, aiming at higher efficiencies and smaller dimensions, the scientific community has focused particularly on nanostructures, decreasing the thickness and increasing the interfaces between the two components. Therefore, as discussed in Section 2.5.3, surface anisotropies together with coupled properties of composites' components, such as piezoelectricity and magnetostriction, can produce gigantic magnetoelectric coefficients. Recently, Jahns *et al.*[35] presented a bilayer heterostructure of Aluminium Nitride (AIN) and FeCoSiB coumpound, whose magnetoelectric coefficient reached the value of 9.7 kV/cm·Oe, the highest measurement ever recorded at normal pressure.

For such heterostructures, a series of ferroelectric ($BaTiO_3$, $PbTiO_3$, $Pb(Zr,Ti)O_3$, $BiFeO_3$) and ferromagnetic ($CoFe_2O_4$, $NiFe_2O_4$, α-Fe_2O_3) materials have been combined. However, due to the toxic character of lead-based compounds,[15–17] despite their excellent ferroelectric properties, more and more research groups are searching for lead-free solutions.

2.5 Bismuth Ferrite: The Model Multiferroic

$BiFeO_3$ (BFO) is the only single-phase multiferroic, presenting simultaneously magnetic and ferroelectric order at room temperature, thus, as mentioned above, is the most studied.[9,11,36–38] It exhibits a strong ferroelectric behaviour, however the apparent antiferromagnetic order of magnetic moments results in weak magnetic response. Concerning its chemical behaviour, BFO is a metastable and off-stoichiometric compound, easily forming secondary phases, like Bi_2O_3, $Bi_2Fe_4O_9$ and sillenite $Bi_{25}FeO_{39}$.[36]

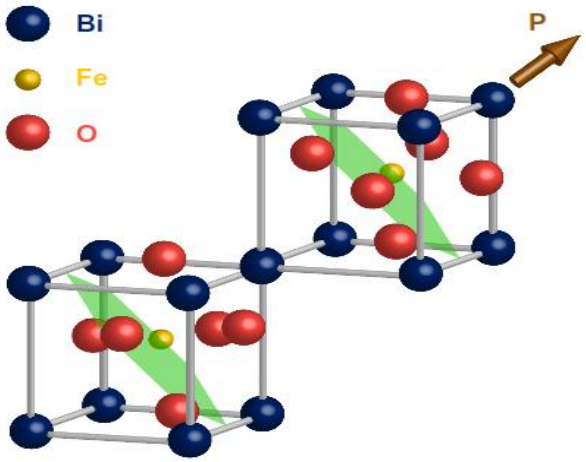

Figure 2.11 Bismuth Ferrite unit cell structure with the oxygen octahedra rotation and the Fe ion shifting.[39]

2.5.1 Ferroelectricity

BFO owes its ferroelectric properties to the two distorted perovskite blocks, connected along the pseudocubic-[111], building a rhombohedral unit cell (**Figure 2.11**). A clockwise and a counterclockwise rotation of the two oxygen octahedra connected along the [111], as well as a shift of the Fe ion also along the [111], are responsible for conferring spontaneous polarization. The Godschmid tolerance factor (Section 0) for BFO is equal to 0.88, which yields a rhombohedral or orthorhombic symmetry. BFO's ferroelectric Curie temperature, or else the temperature at which the ferroelectric to paraelectric transition takes place, corresponds to 1100 K.[37,38]

BFO's piezoelectric constant (d_{33}) is substantially low, reaching a maximum of approximately 100μC/cm^2, whereas other perovskites extend to 100-1000μC/cm^2. The

reason for the presence of such a large difference is BFO's small dielectric constant at room temperature, which corresponds to approximately 30. This can be easily understood by the definition of the effective piezoelectric coefficient, as shown in Eq. 6:

$$d_{33}^{eff} = \frac{\partial s}{\partial E} = \frac{\partial s}{\partial P}\frac{\partial P}{\partial E} = 2QP\varepsilon \qquad \text{Eq. 6}$$

where s, P, E, Q and ε stand for strain, polarization, electric field, electrostrictive coefficient and dielectric constant respectively.

Since the value of Q does not diverge much from the ones of other perovskites, dielectric constant accounts for such behaviour. The dielectric constant evaluation is inseparably linked with polarizability measurements. The relatively small electric fields required for dielectric measurements cannot affect the highly saturated polarization at room temperature, due to the elevated Curie temperature of BFO (1100K). Another assumption coming from experimental results places emphasis on the possible existence of a difference between the A-site and B-site cation originated polarizations, with the A-site case present at BFO being the lower.[37]

This relatively small piezoelectric coefficient is also responsible for the weak contribution of strain-induced polarization in epitaxially grown BFO thin films. As a result, an increase in effective piezoelectric coefficient with increasing film thickness is observed (**Figure 2.12**). [29]

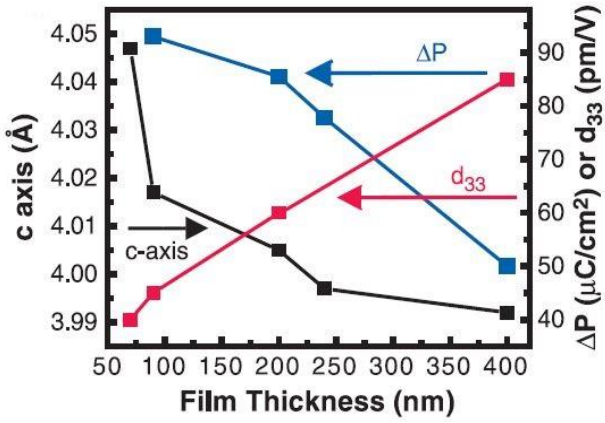

Figure 2.12 Effective piezoelectric coefficient as a function of film thickness for epitaxially grown $BiFeO_3$ thin films.[29]

Finally, the [111] oriented polarization in BFO is bound to switching by the application of an external electrical field. There are three possible rotations: 71°, 109° and 180° (**Figure 2.13**). The first two also result in the rotation of the antiferromagnetic planes, hence providing evidence for a magnetoelectric behaviour. The antiparallel case of 180° for symmetry reasons maintains the initial magnetic ordering. Zhao *et al.*[40] and Zavaliche *et al.*[41] showed the influence of polarization rotation in the antiferromagnetic domains, by the combination of Piezoresponse Force Microscopy (PFM) and Photoemission Electron Microscopy (PEEM) techniques.

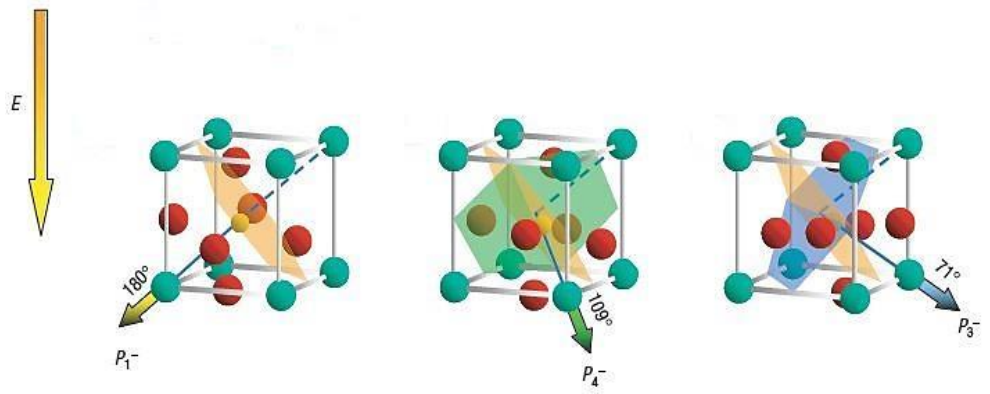

Figure 2.13 The three possible rotations of polarization orientation in $BiFeO_3$ by the application of an external electric field.[40]

2.5.2 Phase Transitions

A great polemic prevails over the complex matter of phase transitions occurring in the $BiFeO_3$ structure. BFO's crystallographic structure determine both its ferroelectric and magnetic properties, often in a way that the cause becomes the effect and vice-versa. This entanglement of causality, in combination with BFO's intricate magnetic behaviour and the presence of impurities, hinders the characterization process.[37,42]

The different BFO phases already observed and proposed by a series of techniques are: rhombohedral, orthorhombic, monoclinic and cubic. The ground phase, or referred to as α-phase, corresponds to a rhombohedral crystal system (R3c). A ferroelectric to paraelectric transition at 825 °C (~1100 K) is clearly detected, presenting simultaneously an impulsive volume contraction. However, the nature of this apparent β-phase remains in question. Apart from the relatively safe agreement of the community for a centrosymmetric

structure, the majority of X-Ray and Neutron Diffraction studies incline towards a mixed rhombohedral-orthorhombic phase. Propositions for the presence of tetragonal or pseudotetragonal systems are mainly rejected due to the observed domain structure. Furthermore, the monoclinic case argument does not agree with the XRD patterns and the most controversial rhombohedral symmetry retainment through the α-β transition is precluded by the occurrence of ferroelastic transition. The higher-temperature γ-phase presents a cubic symmetry, though usually obscured by the presence of parasitic phases, such as $Bi_2Fe_4O_9$ and Fe_2O_3. Lastly, anomalies reported in dielectric constant measurements reveal low-temperature (50 K and 200 K) weak coupling, probably of magnetic or magnetoelastic nature, as well as a possible magnetoelectric coupling at 370 ^oC (30^oC bellow antiferromagnetic Néel temperature 673 K).

A proposition of the possible phase transitions as a function of temperature and pressure occurring in $BiFeO_3$ is presented in **Figure 2.14**. A coincidence in the sequence of the main occurring transitions (rhombohedral → orthorhombic → cubic) can be observed both for temperature and pressure increase. There is a slight rise of the antiferromagnetic Néel temperature with increasing pressure.

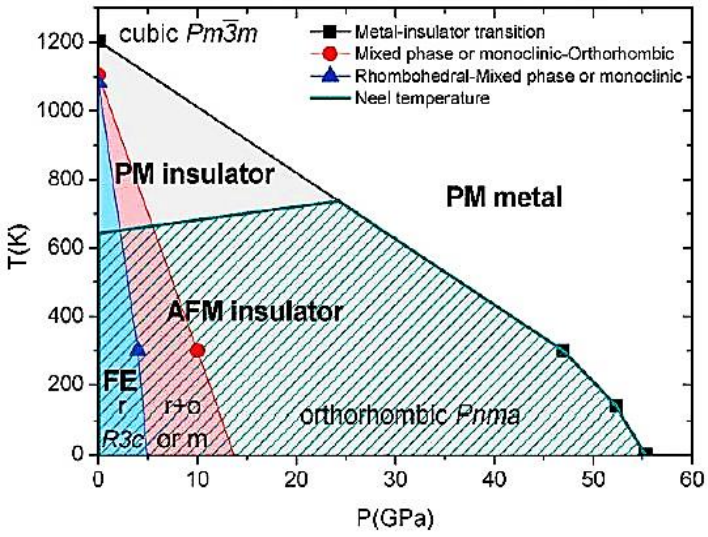

Figure 2.14 Phase transition diagram for $BiFeO_3$ as a function of temperature and pressure. Solid points correspond to experimental data. Blue region presents the ferroelectric rhombohedral phase (R3c). Light red region represents the paraelectric β-phase, primarily suggested by the majority as a rhombohedral-orthorombic mixed phase or the less supported monoclinic. White region shows the cubic γ-phase and along the black-green line the metal-insulator transition. Green line indicates the antiferromagnetic to paramagnetic transition (Néel temperature).[37]

2.5.3 Magnetism

A combination of various scenarios seems to give rise to the complex magnetic behaviour of BFO.

One of the most widely accepted theories is that of G-type antiferromagnetic ordering, resulting from the ferromagnetically and antiferromagnetically ordered Fe magnetic moments along the [111] axis and between the adjacent planes, respectively (**Figure 2.15**(a)).[37,43] BFO's antiferromagnetic to paramagnetic transition happens at the antiferromagnetic Néel temperature of 673K.

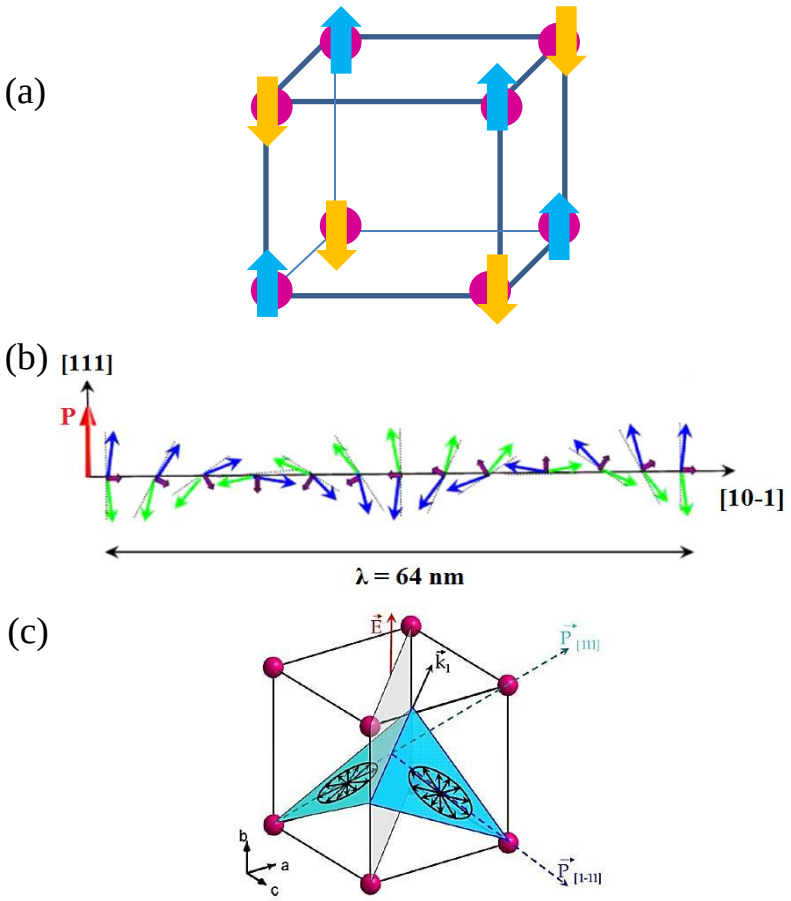

Figure 2.15 (a) G-type antiferromagnetic order in $BiFeO_3$. (b) Spin cycloid order with wavelength period of 64nm. (c) Cycloidal spin-induced polarization and magnetoelectric coupling due to change in the orientation of the cycloid plane by 71^{o} rotation in polarization.[44]

Most studies are based on Dzyaloshinskii-Moriya interaction, which corresponds to the spin-exchange accompanied by spin-orbit coupling, leading to canting of the magnetic sublattices.[43] The latter phenomenon together with the rotation of the oxygen octahedra

yields weak macroscopic ferromagnetism. The lattice distortion impact on BFO's ferromagnetic character can be also understood by the relatively low Godschmid tolerance factor (Section 2.5.1), a fact that allows for buckling of the oxygen octahedra, hence change in the angle between Fe-O-Fe.[37]

Another proposal for the apparent magnetic activity in BFO, first published by Sosnowska *et al.*[45], is the presence of a cycloidal spin arrangement of the antiferromagnetic sublattices, following a wavelength period of 64nm and propagating perpendicularly to [111] pseudocubic axis (**Figure 2.15**(b)). Suppression of the cycloidal spin structure, due to epitaxial strain in thin films[43] or grain-particle size[3,4,46,47], can lead to the emergence of uncompensated magnetic moments. In addition, this long-range superstructure can result in the induction of an additional polarization, giving rise to magnetoelectric coupling.[44] As shown in (**Figure 2.15**(c)), a rotation by 71^{o} in polarization orientation can result in change in the magnetic cycloid plane, providing strong evidence for magnetoelectric coupling. In bulk architectures cycloid spin structure can induce canting angles of 2.25^{o}, introducing a significant contribution to the overall magnetoelectric effect. In thin films, cycloidal magnetic moment order appears to result in smaller canting angles (~0.2^{o}), leaving Dzyaloshinkii-Moriya interactions accounting for coupling manifestation.

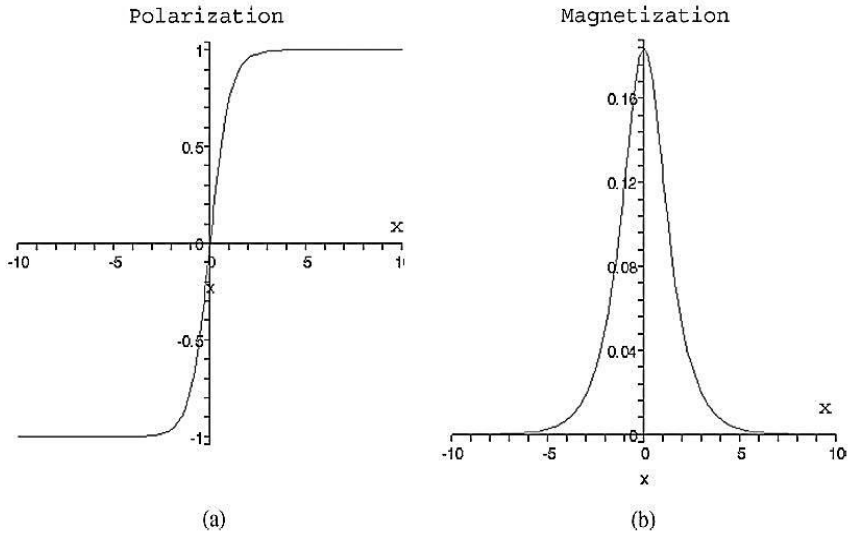

Figure 2.16 (a) Polarization and (b) magnetization magnitude as a function of ferroelectric domain wall thickness x.[48]

Furthermore, ferroelectric domain walls appear to play an important role to magnetization generation, as shown by Privratska *et al.*[49] and later by Darakrchiev *et al.*.[48] The symmetry breaking and lack of homogeneity in domain walls can produce significant spontaneous magnetization (**Figure 2.16**). This fact is accentuated by the considerable occupying volume fraction of walls in thin films, due to smaller grain sizes. In addition, Kay-Dunn law reveals a power dependence between the domain wall thickness d and the resulting coercive electric field E, as can be seen in Eq. 7:

$$E = A \cdot d^{-\frac{2}{3}} \qquad \text{Eq. 7}$$

As wall thickness decreases, higher fields are generated and the anisotropy degree is substantially increased, hence enhanced magnetoelectric coupling can occur.

Finally, as mentioned above, any anisotropy may lead to the rise of magnetism, among which the megnetocrystalline, surface and shape related are the most important.[50,51] For the case of thin films, perpendicular surface anisotropy can be responsible for ferromagnetic ordering, even for antiferromagnetic materials. Surface influence in anisotropy is much stronger than that caused by volume fractions, a solid explication for the comparable magnetizations observed between bulk and thin films. Wang *et al.*[29] in 2003, showed that magnetization increases with decreasing film thickness in BFO thin films.

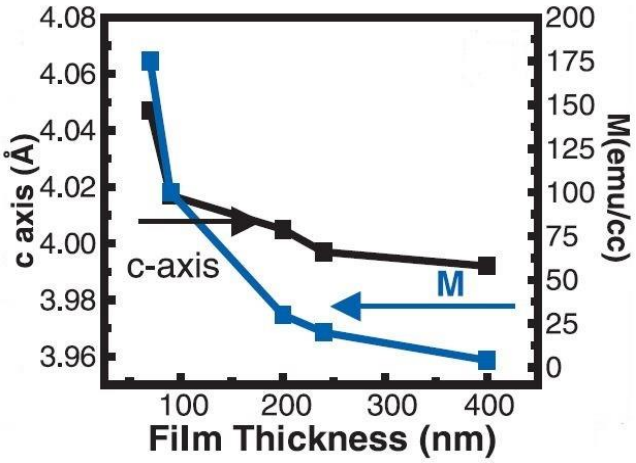

Figure 2.17 Magnetization of BFO films as a function of film thickness.[29]

2.6 The Strategy for Porous Thin Film Preparation

2.6.1 Sol-gel Process

A plethora of thin film preparation techniques has been developed over the years, such as Molecular Beam Epitaxy (MBE), Pulsed Layer Deposition (PLD), Radio Frequency Sputtering (RFS), Metalorganic Chemical Vapor Deposition (MOC-VD), Chemical Solution Deposition (CSD), to name a few.[9] The latter corresponds to a simple and cost-effective chemical method and consists of the preparation of a solution and its subsequent deposition on a substrate.

The sol-gel process, one if the CSD methods, corresponds to the hydrolysis of inorganic or metal organic reactive precursors in aqueous or organic solvents, followed by condensation reactions, which result in the so-called gel.[38,52,53]

Sol is a colloidal suspension of well dispersed solid particles in a liquid.[54] Due to the small dimensions of the dispersed phase, Van der Waals forces and surface charge interactions surpass the gravitational field influence. Gel corresponds to a porous three-dimensional solid network and, depending on the medium that fills the pores, it can be aquagel, hydrogel, alcogel, aerogel or cryogel. The various steps of the sol-gel procedure are the following: preparation of a homogeneous solution, conversion to sol, gel formation (polycondensation), gel shaping (thin films, fibres, spheres or grains) and sintering.[54]

For the case of a metal alkoxide $M(OR)_n$ with valence n, the following reactions take place:

$$M(OR)_n + H_2O \rightarrow M(OR)_{n-1}\,OH + ROH \qquad \text{(Hydrolysis)}$$

$$M(OR)_{n-1}\,OH + M(OR)_n \rightarrow (RO)_{n-1}\,M\text{-}O\text{-}M\,(OR)_{n-1} + ROH \qquad \text{(Condensation)}$$

The first reaction corresponds to the hydrolysis of the alkoxy groups and the second one to the polycondensation. The result is a gel with a mixture of weakly bonded polymers and highly condensed particles.[53]

2.6.2 Dip-coating Deposition

Some of the deposition techniques for the preparation of thin films are spray-coating, meniscus-coating, dip-coating and spin-coating.[55] One of the most widely used is dip-coating, mainly due to its simplicity, the ability of producing homogenous films with controlled thickness, the lack of waste and, certainly, its low-cost.[52,53,56]

For film deposition via dip-coating, the substrate is dipped into the sol-gel and subsequently withdrawn at a constant speed.[56] Since sol-gel's nature is non-newtonian, evaporation of the solvents takes place during deposition, which is determinant for the film formation. Many factors are influenced by the evaporation mode, such as viscosity, density, surface tension, pH and local accumulation of precursors. Another important factor that necessitates scholastic control is the hydrolysis and condensation reaction kinetics taking place throughout the whole procedure, until the final heat treatment, which affect the degree of condensation, the density and the species' structure.

In **Figure 2.18** (a), one can observe the gradual evaporation of the solvents, the formation of meniscus and the decrease of the film thickness, during the deposition. Although, phenomenologically, we expect an increase in the thickness by increasing withdrawal velocity due to draining phenomenon, in reality, there are two regimes that govern the process: a capillary/evaporation regime for very low withdrawal velocities and a draining/evaporation regime for higher values (**Figure 2.18** (b, c)). The first behaviour is owing to capillary phenomena, which lead to a linear evaporation, thus obstruction of otherwise expected draining.

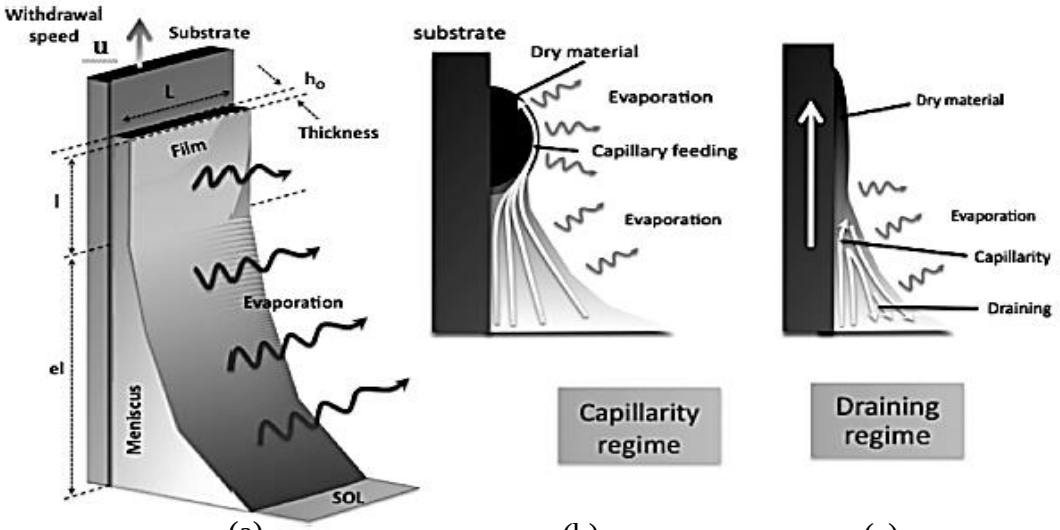

Figure 2.18 (a) Schematic illustration of sol-gel process. (b, c) The two different regimes taking place through dip-coating method: (b) capillary and (c) draining, for slow and fast film withdrawing, respectively.[56]

Faustini *et al.*[56] conducted a comparison between an experimental procedure (using a sol-gel derived from the mixture of tetraethyl and methyltriethyl orthosilicates with Pluronic F127 copolymer), a capillarity model and a draining model, as shown in **Figure 2.19**. There is a very good correlation between the experimental results and the combination of the two models incorporating the capillary and draining regimes.

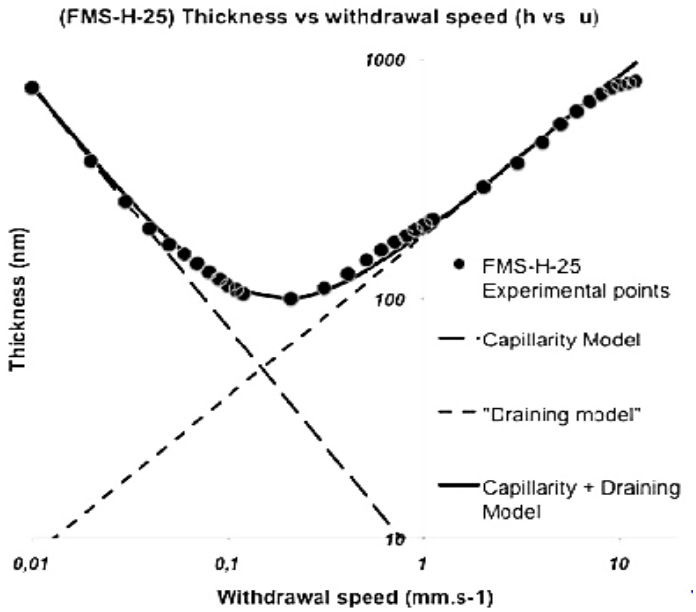

Figure 2.19 Thickness of the deposited film as a function of withdrawal speed. Draining, capillary and combination of the two models are presented along with an experimental sol-gel deposition points.[56]

2.6.3 Evaporation Self-Induced Assembly (EISA)

There are various chemical and physical methods for the induction of porosity in thin films, however, Evaporation Induced Self-Assembly (EISA) is one of the most popular, owing to its simplicity and rapid production of patterned pores.[57–59] EISA is based on the use of micellar and lyotropic liquid-crystal phases, which act as templates, regulating the nucleation, growth, morphology and orientation of inorganic crystals, and, after evaporation during the thermal treatment, eventually, they form periodically organised porous structures.[55,57,60]

As shown in **Figure 2.20**, there are 4 main steps during the EISA process: solvent evaporation, which ends with the gel formation, water equilibrium, mesostructuration, which result in the hybrid organic/inorganic structure and, finally, condensation through treatment and removal of the templates. Throughout the whole procedure, overlapping of the different stages might occur.

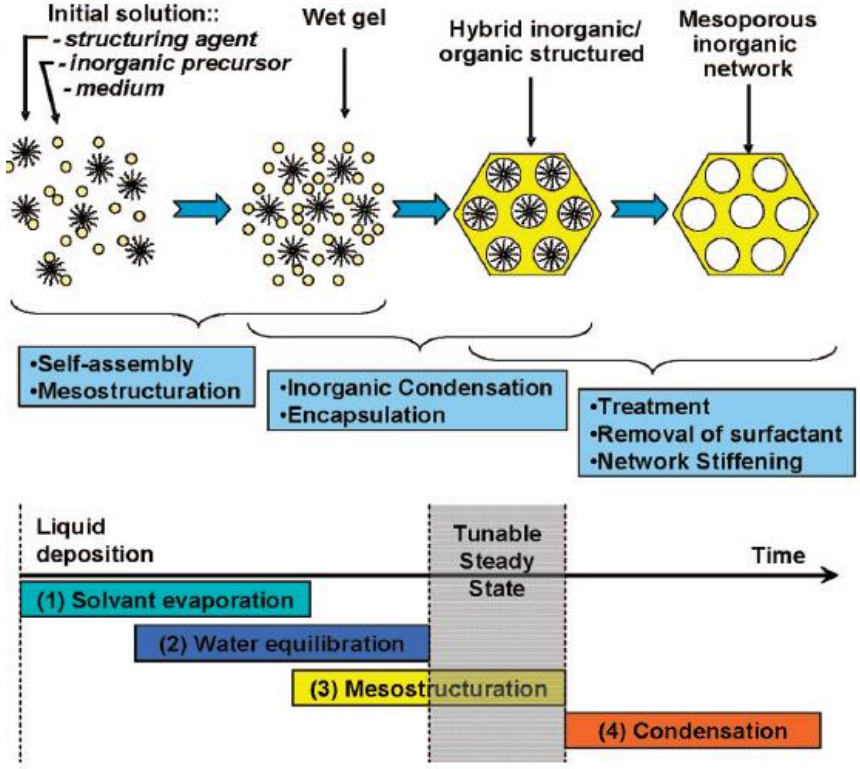

Figure 2.20 Schematic illustration of the different steps occurring through the evaporation-induced self-assembly for the formation of mesoporous structures.[55]

The templates consist of hydrophilic and hydrophobic parts. The hydrophilic tails are selectively brought in contact with water, bringing the hydrophobic ones shielded within the spherical or cylindrical micelle.

By increasing the templates molecular weight and, as the critical micelle concentration has been exceeded, spherical and cylindrical micelles are formed, thus different pore sizes can be produced (**Figure 2.21**). Further increasing of the templates concentration, periodic hexagonal, cubic or lamellar structures can be achieved.[57]

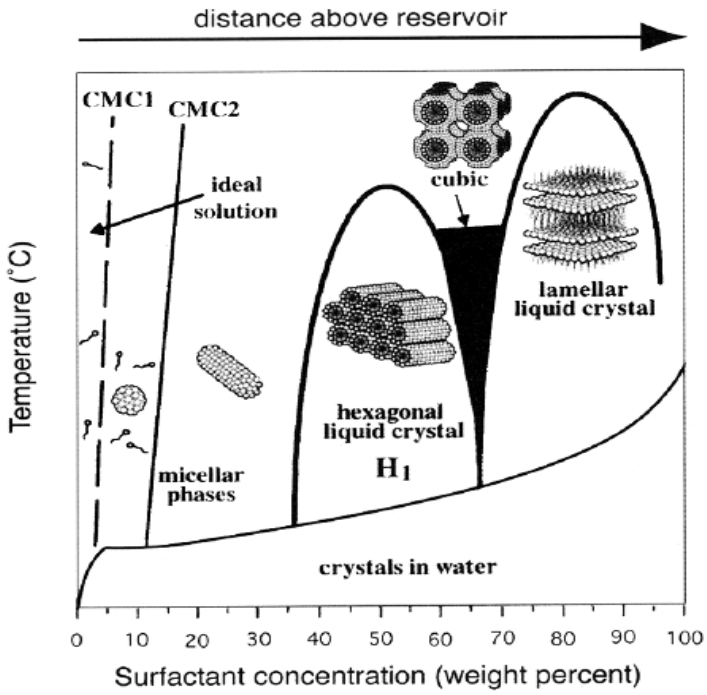

Figure 2.21 Presentation of the different geometries for cetyltrimethylammonium boride (CTAB) as a function of temperature and surfactant concentration.[57]

2.7 Piezoresponse Force Microscopy (PFM)

Piezoresponse Force Microscopy (PFM), currently one of the most popular techniques of ferroelectrics' characterization via Scanning Probe Microscopy (SPM), allows a nondestructive visualization of domain structures at the nanoscale in thin films and bulk materials.

2.7.1 Historical Review

The historical starting point for the wider family of Scanning Probe Microscopy takes place in 1981, with the invention of Scanning Tunneling Microscope (STM) by Gerd Binnig and Heinrich Rohrer, to whom subsequently the Nobel Prize in Physics was attributed in 1986 for their so-called "candid cameras of the nanoworld".[61,62] STM's function is based on the quantum-mechanical phenomenon of electron tunnelling, occurring by the application of a relatively small electric potential between an atomically sharp conducting tip and the surface of a conducting or semi-conducting sample. By measuring the resulting current of those electrons that manage to overcome the barrier, the topography of the sample surface can be given down to atomic resolution. In 1990, the world's smallest logo was created by such a microscope. I.B.M.'s initials were formed by arranging 35 individual xenon atoms (**Figure 2.22**).[63] That was the moment that the message was passed along even outside the scientific community and "sneaking" into the atomic world became "messing" with the actual atoms!

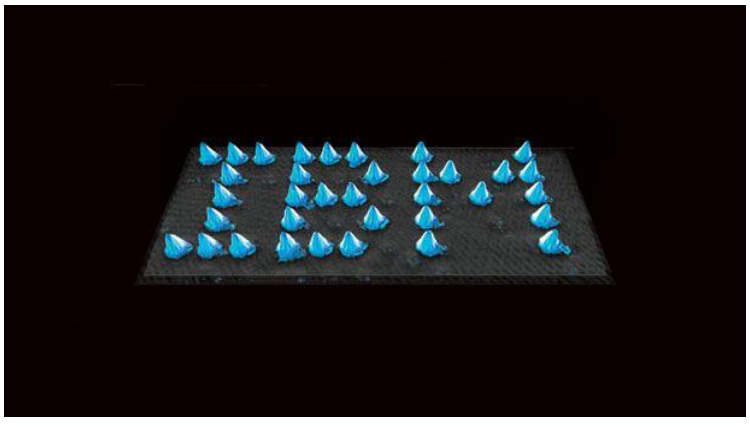

Figure 2.22 The world's smallest logo. I.B.M.'s initials presented by 35 individual xenon atoms, by the use of Scanning Tunneling Microscope (STM) (image published in 1990 by Eigler & Schweizer in Nature [63], but artistically adapted by IBM Research [64]).

However, STM's limitation to conducting and semi-conducting materials, lead to the development of Atomic Force Microscopy (AFM), in 1986 by Binnig *et al.*.[65] This time the basic functioning principle is even simpler, since the only measurement is the deflection of the tip as it passes over the sample surface, therefore no conduction is needed and the range of materials is substantially widened, particularly for the ample field of biomolecular analysis. Different modes have been developed since, such as contact, non-contact and tapping mode, to mention the most important ones, depending on the material and the properties in question.

In 1991, Birk *et al.* publish the first measurements made by Piezoresponse Force Microscopy (PFM) for Vinylidenefluoride Trifluoroethylene (VDF-TrFE) thin films.[66] In 1992, Guthner *et al.* refer to a new ferroelectric storage technique (write-read) by local poling, as well as the crucial ferroelectric domain size effect due to tip geometry and film thickness. However, the systematic studies carried out by Gruverman *et al.*[67,68] highlight the importance and utility of PFM technique for a profound insight into the ferroelectric behaviour of materials.

2.7.2 Principles of Operation

PFM technique is based on a very simple method, yet without preventing high accuracy and reliability. The general idea derives from the principles of inverse piezoelectric effect, or else the conversion of electrical energy to mechanical. In that way, the measurement is realized by detecting the electromechanical interaction between the sample surface and a conductive tip, induced by the application of an external ac voltage.[67,68]

AFM technique is grounded in Hooke's law and the oscillatory behaviour of the force sensor, which consists of two parts: a cantilever-type spring with position parallel to the sample surface and a sharp tip placed at the edge of the cantilever perpendicularly to both surface and cantilever (**Figure 2.23** (a, b)). A laser beam is deflected on the top-side of the cantilever and, subsequently collected by a Position Sensor Detector (PSD), usually a quadrupole-electrode geometry photodiode (**Figure 2.23** (c)). The detection precision corresponds to sub-Å scale. A piezoelectric scanner with nanometric precision is responsible for the sample movement relative to the tip, allowing for lateral and vertical

movements. In order to achieve a topography image, the cantilever deflection must be kept constant.

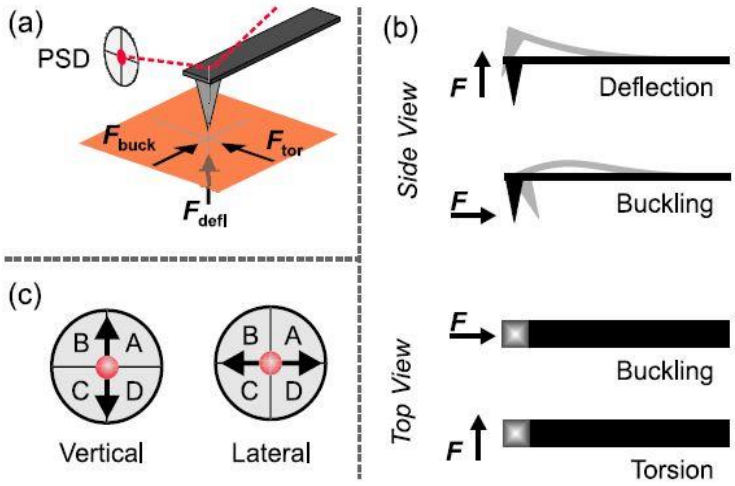

Figure 2.23 (a) Schematic illustration of cantilever-tip geometry and position. Red dashed line represents the laser deflection on the Position Sensing Detector (PSD). F_{defl}, F_{buck} and F_{tor} are the forces which result in tip's deflection, buckling and torsion effects respectively. (b) Cantilever's vertical deflection, buckling and torsion effects. (c) Vertical (caused by F_{defl} and F_{buck}) and lateral (F_{tor}) signals of cantilever movement detected by a quadrupole-electrode geometry of the detector (PSD).[69]

As mentioned above, there are various AFM modes for the obtainment of different information. For the case of piezoelectricity, contact mode is necessary for sensing the vibration of the sample surface. Surface reaction to the applied field is characterized by short-range repulsive interatomic forces, thus the contact requirement, unlike the non-contact case, intended for the detection of long-range interactions, such as magnetic, electrostatic and Van der Waals.[68]

The external voltage applied between the tip and the surface consists of a dc and an ac component, as shown in Eq. 8:

$$V_{ex} = V_{dc} + V_{ac}\cos \omega t \qquad \text{Eq. 8}$$

where ω is the frequency of ac component. A lock-in technique is used to modulate the output signal, in a sense that topographic and piezoresponse signals to be separated, providing the two images simultaneously. For a homogeneously polarized material, the vertical displacement under voltage V, as a function of the piezoelectric and electrostrictive coefficients, d_{33} and Q_{33} respectively can be expressed as:

$$\Delta z = d_{33}V + \frac{Q_{33}}{t}V^2 \quad \text{Eq. 9}$$

where t is the sample thickness.[70] Since lock-in technique does not measure the dc component, the vertical displacement Δz via Eq. 8 becomes:

$$\Delta z = d_{33}V_{ac}(cos\omega t + \varphi) + 2\frac{Q_{333}}{t}V_{dc}V_{ac}(cos\omega t + \varphi) \quad \text{Eq. 10}$$

where φ the phase difference between the ac input and the piezoreponse output signal, related to the polarization direction.[20] Eq. 10, corresponds to the first harmonics of the signal and its first part is linked to the piezoelectric effect. The second part, as well as the second harmonics can be neglected, since they are basically related to the electrostrictive effect, which is much weaker and it only produces a dc offset. Thus, a PFM image is composed by:

$$\Delta z = d_{33}V_{ac}\cos(\omega t + \varphi) \quad \text{Eq. 11}$$

Depending on the information in question, both mapping of amplitude $d_{33}V_{ac}$ and phase φ can be conducted.

A series of reasons have established PFM technique as one of the most accepted and popular methods for the investigation of piezoelectric properties. Firstly, its high spatial resolution, lack of special sample preparation and normal conditions operation lead to cost and time-effective studies. In addition, its high vertical sensitivity prevents any destructive considerations. A variety of phenomena linked with piezoelectric behaviour can be easily studied, such as switching mechanisms, writing-reading in micrometric scale, microstructure-domain correlation, domain wall investigation and degradation effects. Importantly, as mentioned before, it gives the opportunity of a simultaneous representation of the surface topography and the piezoelectric response. By choosing the adequate cantilever-tip, one can work with a wide range of surface roughness and hardness. Furthermore, contact mode is not susceptible to screening effects, usually caused by charge absorption when non-conduct, hence no veiling of domain mapping can occur. It should be mentioned that PFM imaging is favourably used for thin film characterization than bulk cases, due to lack of uniformity of the applied electric field. Lastly, the ability of measuring piezoelectric properties locally at a nanoscale provides an insight to more complicated structures, such as polycrystalline or inhomogeneous samples.[67,68,71]

2.7.3 PFM Studies of Bismuth Ferrite

BFO's good ferroelectric behaviour, and most importantly its large remanent polarization, allows for extended studies via PFM technique. Compared to pure ferroelectrics, BFO's multiferroic character induces bigger domains, due to magnetoelectric coupling occurring at the domain walls.[48,72]

Three main domain structures have been observed in BFO thin films by the use of PFM technique. For film thicknesses of about a few hundreds of nanometres, the domain patterns are mostly striped (**Figure 2.24** (a)). However, decrease in the thickness originates an irregular domain structure, accompanied by a fractal configuration along the domain walls (**Figure 2.24** (b)). Mosaic-like structures are observed by domain imaging of polycrystalline samples, such as films deposited via sol-gel method (**Figure 2.24** (c)).[73]

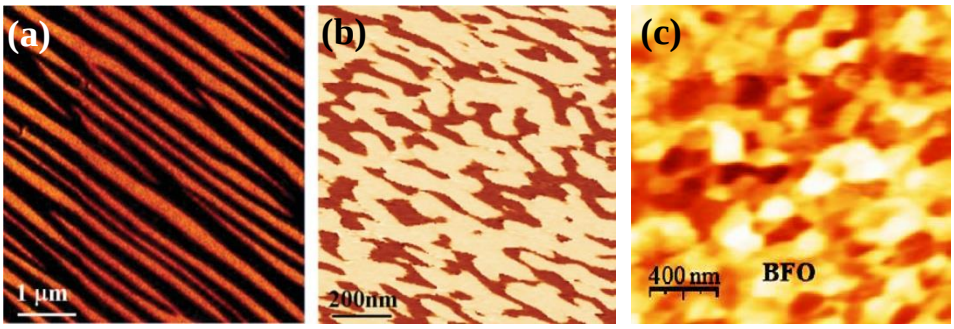

Figure 2.24 The three main domain structures observed by PFM in BFO thin films: (a) Striped and (b) irregular domains in epitaxially grown thin and ultrathin films respectively,[37] and (c) mosaic-like in polycrystaline sol-gel deposited thin film.[73]

As mentioned in Section 2.5.1, the three polarization rotations, taking place by the application of the electric field, were studied by Zavaliche *et al.*[32,74] and are presented in **Figure 2.25**. In-plane PFM images show a higher contrast between the domains, due to polarization orientation. An external dc electric field of -12V magnitude was applied to the samples. The dark square in **Figure 2.25** (b) denotes the poled area, thus much more intense in the out-of-plane imaging. Relevant pattern can be observed also for the respective in-plane piezoeresponse in **Figure 2.25** (c). In **Figure 2.25** (c, d, e) we can see clearly the three polarization rotations: P_1^{-1} switches to P_1^{+1} and P_3^{-1} by 180^o and 71^o respectively and P_4^{-1} is rotated by 109^o.

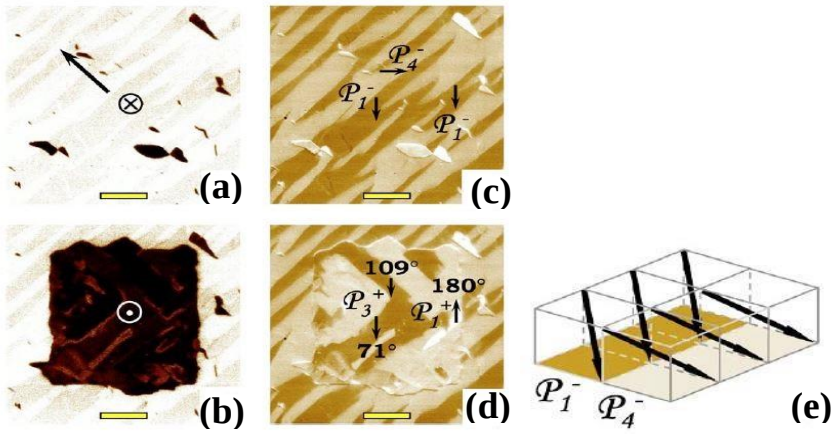

Figure 2.25 (a, b) Out-of-plane and (c. d) in-plane PFM images, before (a, c) and after (b, d) poling of the sample with the application of -12V dc. (e) Schematic representation of polarization orientations noted in (c, d). The bars are of 1μm.[41]

Magnetic Force Microscopy is based on a combination of tapping and non-contact mode, for topography and magnetic response mapping of the same area, by the use of magnetically coated conductive tips. However, unlike PFM technique, the two images are not taken simultaneously. The tip after taking the tapping signal of one scanning line, draws further from the surface in order to detect magnetic interactions.

Unfortunately, the antiferromagnetic nature of BFO makes impossible the visualization of magnetic domains via Magnetic Force Microscopy (MFM). Nevertheless, the magnetoelectric coupling in composite heterostructures, such as the ferromagnetic $CoFe_2O_4$ nanopilars in $BiFeO_3$ matrix shown in **Figure 2.26**, is of great interest and it produces good description of magnetic domains, originated by the nanopilars, and their switching under dc bias of -16V.

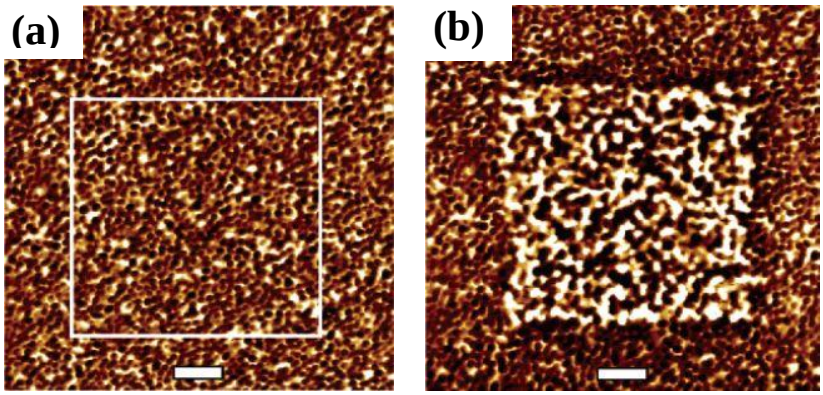

Figure 2.26 MFM images of magnetized $CoFe_2O_4$-$BiFeO_3$ vertical heterostructure (a) before and (b) after poling at -16V. The bars are of 2μm.[32]

CHAPTER 3

Experimental Procedure

3. Experimental Procedure

In this chapter the experimental procedure conducted in this work is described. It consists of three main parts: i) the preparation of dense thin films with varying withdrawal velocities, ii) the preparation of porous thin films with varying solution template concentration and withdrawal velocities, accompanied by annealing temperature studies, and iii) the characterization tools and strategy (**Figure 3.1**).

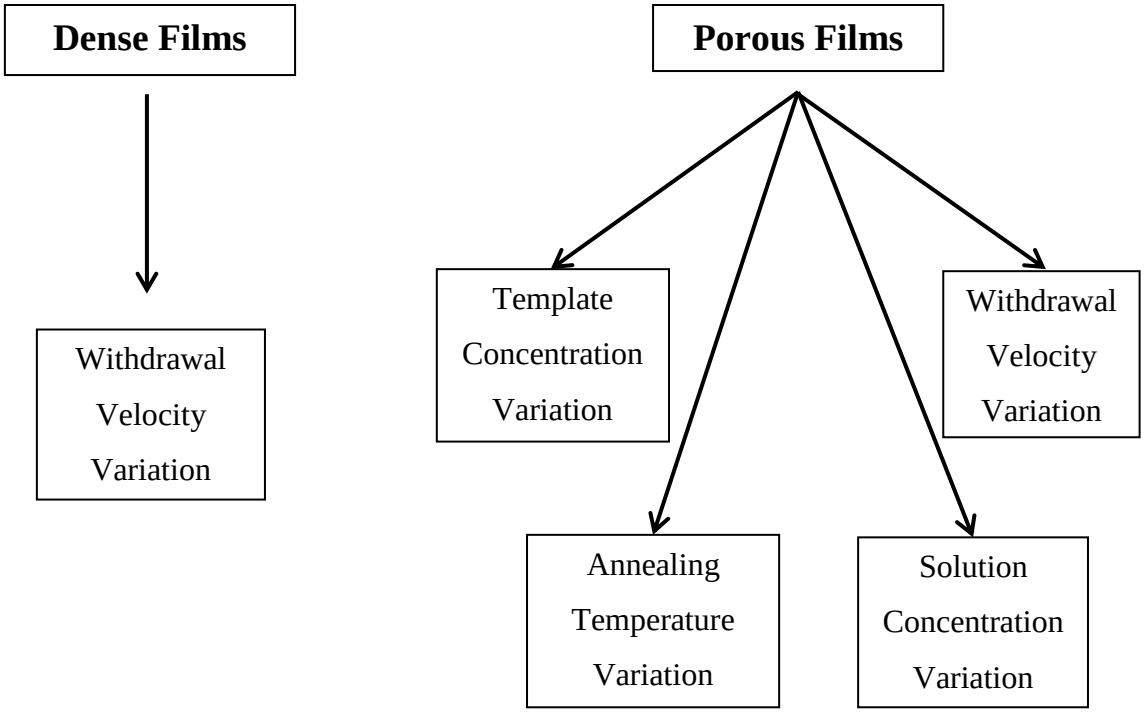

Figure 3.1 Schematic representation of the strategy of the current work.

3.1 Dense Films

The preparation of dense films basically aims at obtaining means of comparison and reference point for the properties of porous films, which is naturally the main subject of this work. Although during the whole procedure of this work, a series of approaches to prepare dense films have been conducted, the most effective one will be reported.

For the obtainment of the dense films, three main steps were followed: i) sol-gel preparation, ii) dip-coating deposition, and iii) drying and annealing (**Figure 3.2**).

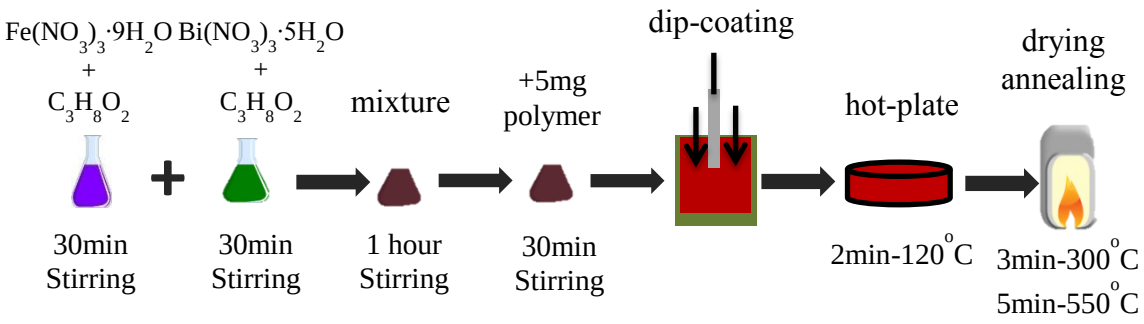

Figure 3.2 Flow diagram for the preparation of dense films.

3.1.1 Sol-gel Process

For the preparation of the sols the following reagents were used: bismuth (III) nitrate pentahydrate (*Aldrich*, purity ≥98%), iron (III) nitrate nonahydrate (*Aldrich*, purity 98%), 2-methoxyethanol (*Aldrich*, purity 99.8%) and pluronic F127 copolymer (*Polymer Source*, purity 100%). The procedure was based on the strategy followed by Coondoo *et al.*[73], yet with some alterations. The sols were prepared with a concentration of 0.5 M, 0.2 mL final volume and 1:1 stoichiometry for the two inorganic precursors, iron (III) nitrate nonahydrate ($Fe(NO_3)_3.9H_2O$) and bismuth (III) nitrate pentahydrate ($Bi(NO_3)_3.5H_2O$). Each precursor was dissolved with 0.1 mL of 2-methoxyethanol ($C_3H_8O_2$), left stirring for 30 min and subsequently the two solutions were mixed. The mixture was kept at constant stirring for 1 h, unlike the case of Coondoo *et al.* that propose a 24 h stirring. Both procedures were tested, however no differences were observed. Another adjustment to the referred strategy was the introduction of a small quantity of

Pluronic F127 copolymer, aiming at the enhancement of the adhesion of the sol on the substrate. For that purpose, 5 mg of copolymer were added to the mixture of the two precursors, followed by 30 min stirring (**Figure 3.2**). The mass and volume quantities used for the three-step procedure, until obtaining the final solution, are presented in **Table 3.1**.

Table 3.1 The three steps of sol-gel preparation with used reagents mass and volume quantities and respective purity and suppliers.

	Reagents	**Mass (g)**	**Volume (mL)**	**Purity**	**Brand**
Precursor 1	$Bi(NO_3)_3.5H_2O$	0.2425	-	≥98%	Aldrich
	2-Methoxyethanol	-	0.1	99.8%	Aldrich
Precursor 2	$Fe(NO_3)_3.9H_2O$	0.2020	-	98%	Aldrich
	2-Methoxyethanol	-	0.1	99.8%	Aldrich
Final Solution	Pluronic F127	0.0050	-	100%	Polymer Source

3.1.2 Dip-coating Deposition

Dip-coating technique was used for the film deposition, mainly due to its simplicity, time and cost-efficiency, as well as the production of homogeneous thickness, as mentioned in Section 2.6.2. The same methodology was employed for dense and porous films. The dip-coater used for the deposition was from *KSV*, model *DC/D/LM*, adapted with a homemade drying chamber.

Prior to the deposition step, the $Pt(111)/TiO_2/SiO_2/Si(100)$ substrates were cut in rectangles of 2 cm x 1 cm and subsequently ultrasonically cleaned with ethanol (EtOH) and acetone during 10 min respectively.

One of the main parameters studied for the preparation of the films was the drying temperature, employed to maximise the adhesion of the sol on the substrate. High temperature during the deposition, between 40 and 90 ^{o}C depending on the solvents in use, facilitates the solvent evaporation process, allowing for domination of the viscous drag upon gravity forces, thus inducing a faster growth of the film.[56] For that purpose, a temperature controller was adjusted to the dip-coater, in such way that the substrate would

be under constant temperature along the entire withdrawal trajectory. After testing the deposition at 40, 50 and 70 ^{o}C, the last one was used, as it resulted in better adhesion for all the range of withdrawal velocities.

Based on Faustini *et al.* studies [56], six different withdrawal velocities were used, as seen in **Table 3.2**. These values correspond to low, medium and high velocities. The purpose was to develop films with increasing thickness, as discussed in Section 4.1.

Table 3.2 Dip-coating withdrawal velocities and respective sample identification.

Sample Identification	Withdrawal Velocities (mm/min)
D5	5.58
D10	10.58
D29	29.58
D45	45.66
D150	150
D180	180

3.1.3 Drying and Annealing Process

A variety of drying and annealing profiles were studied, since preparing a dense structure without changing significantly the porous film-based recipe proved to be substantially difficult. Indeed, it was verified that the polymer used as adhesion regulator led to the formation of pores and cracks. Thus, a more controlled procedure for evaporation of solvents and polymer removal was followed.

Apart from the temperature control during deposition, two drying steps were introduced before annealing. Immediately after the deposition, the film was placed on a hot-plate at 120 ^{o}C for 2 min and subsequently fired at 300 ^{o}C for 3 min.[73] Finally, the films were annealed at 550 ^{o}C for 5 min in air, in order to establish the required crystallization. As discussed in Sections 4.1 and 4.2.2, mainly due to dense-porous comparison reasons, the films were additionally annealed at 600 ^{o}C for 5 min.

3.2 Porous Films

The porous thin film preparation procedure consists also of three main steps: i) sol-gel process, ii) dip-coating deposition, and iii) annealing (**Figure 3.3**).

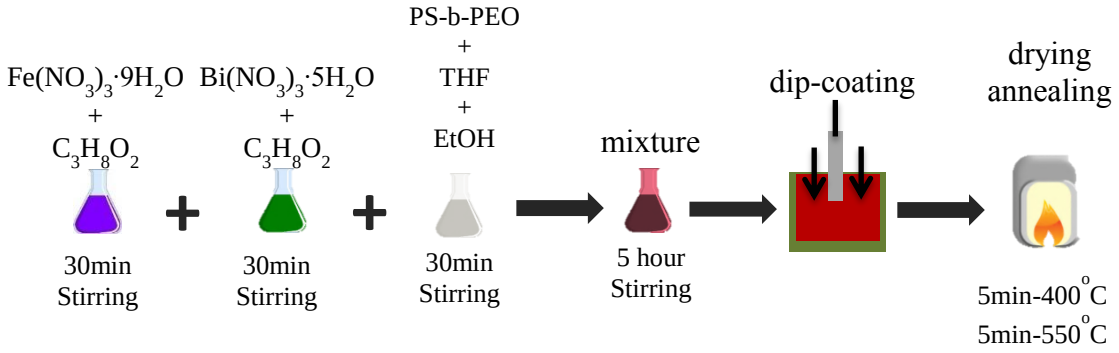

Figure 3.3 Flow diagram for the preparation of porous thin films.

3.2.1 Sol-gel Process

The sol-gel process for the case of porous thin films differs from that of dense, principally due to the introduction of the templates, employed for the induction of porosity. Thus, the initial solutions for the inorganic precursors are prepared as for the dense case, yet with different quantities for solids and solvent (**Table 3.3** and **Table 3.4**).

The template used in this task is polystyrene-poly(ethylene oxide) (PS-b-PEO) block copolymer, which consists of two polymer blocks, a hydrophilic (PEO) and a hydrophobic (PS). Its polymer molecular weight is 40,000 g/mol (PS) - 53,000 g/mol (PEO) (*Polymer Source*). The template dissolution was realized by the use of tetrahydrofuran (THF, *Aldrich*, purity ≥99.5%) and ethanol (EtOH, *Panreac*, purity P.A.). PEO and PS present relatively similar degree of affinity with THF, thus the latter is initially introduced, resulting in the formation of a homogeneous solution with the copolymer chains separated. By adding EtOH, which has a hydrophilic character, the PEO part of the chain is oriented towards the EtOH molecules and the PS parts, being hydrophobic, are approached to each other. The result of this molecular rearrangement is the formation of micelles, which are composed by a central PS sphere and an outer co-central PEO cell (**Figure 3.4**).[75]

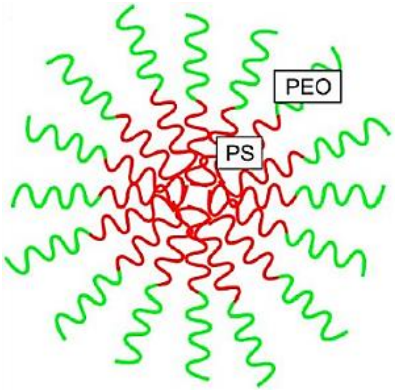

Figure 3.4 Schematic illustration of a micelle formed by PS-b-PEO block copolymer.[76]

In order to achieve equilibrium between the two activities and prevent precipitation, mainly provoked by surpassing the critical micelle concentration due to EtOH excess, a volume ratio between THF and EtOH of 1:3 is required. In order to assist the dissolution procedure, for each solvent step the solution was kept in the oven at 60 - 70 ^{o}C for 10 - 15 min, depending on the template concentration. When the template solution was sufficiently dissolved, the mixture of the inorganic precursors was introduced drop by drop, avoiding sudden expansion of micelles, caused by the polar character of 2-methoxyehtanol. As discussed in Sections 2.6.2 and 2.6.3, the formation of micelles is a continuous procedure, which lasts until the final thermal treatment, thus it is influenced by every step and its respective parameters, such as solvents character and quantities, dip-coating withdrawal velocity and temperature and, finally, thermal treatment.

Two principal studies were conducted for the case of porous thin films; the role of the concentrations of: a) the template and b) the inorganic precursors, which implied adjustments in the initial solution. For the first case, 5 different solutions with varying template quantities and fixed inorganic precursors concentration of 0.3 M were produced (**Table 3.3**). For the second case, three different solutions with varying concentrations and fixed template mass at 30 mg were prepared (**Table 3.4**).

Table 3.3 Series of solutions with respective reagents quantities for the case of template concentration study, with fixed inorganic precursors concentration of 0.3 M.

Sample Identification	Template Mass (mg)	$Bi(NO_3)_3.5H_2O$	$Fe(NO_3)_3.9H_2O$	$C_3H_8O_2$	THF	EtOH
P60	60	0.1455 g	0.1212 g	0.67 mL + 0.67 mL*	0.17 mL	0.5 mL
P48	48					
P36	36					
P30	30					
P24	24					

*The quantities referred are for each inorganic precursor.

Table 3.4 Series of solutions with the respective reagents quantities for the case of the inorganic precursors concentration study, with fixed template mass of 30mg.

Sample Identification	Concentration	$Bi(NO_3)_3.5H_2O$	$Fe(NO_3)_3.9H_2O$	$C_3H_8O_2$	THF	EtOH
P0.3	0.3 M	0.1455 g	0.1212 g	0.67 mL + 0.67 mL*	0.17 mL	0.5 mL
P0.4	0.4 M	0.1940 g	0.1616 g			
P0.5	0.5 M	0.2425 g	0.2020 g			

* The quantities referred are for each inorganic precursor.

3.2.2 Dip-coating Deposition

The step of sol-gel deposition on substrates is similar to that of the dense films, discussed in Section 3.1.2, however the used temperature deposition was 90 ^{o}C, based on the studies discussed in Section 4.2.1. For the investigation of the withdrawal velocity effect on the multiferroic properties of porous thin films the selected solution was that of 0.3 M concentration of the inorganic precursors and 24 mg of solution template mass, since

it presented the best results concerning the porous network ordering. The different withdrawal velocities and the respective sample identification are presented in **Table 3.5**.

Table 3.5 Dip-coating withdrawal velocities and respective sample identification.

Sample Identification	Withdrawal Velocities (mm/min)
P5	5.58
P10	10.58
P29	29.58
P45	45.66
P100	100
P150	150

3.2.3 Annealing Process

All porous films were treated under the same annealing profiles. Initially, the chosen temperature was 400 ^{o}C for 5 min, aiming at the removal of the templates. Subsequently, the films were annealed at 550 ^{o}C and 600 ^{o}C for 5 min each, in order to study the multiferroic properties for both temperatures.

Nevertheless, since the disappearance of the ordering of the porous structure was observed at elevated temperatures, required for the crystallization of the films, two annealing temperature/time studies were conducted for the case of sample P30 (Section 4.2.2). For the first case, the films were annealed at 400, 450, 500, 550, 600 and 650 ^{o}C for 5 min each, in order to observe the effect of the annealing temperature on the microstructure development. The second study aimed at investigating the effect of annealing time on the crystallization and densification of the sample. In this case the films were annealed at 450 and 500 ^{o}C for 5, 10, 20, 30 and 60 min for each temperature.

3.3 Characterization

The structural, microstructural and ferroic properties of the thin films were assessed through a series of characterization methods.

Crystallinity and formed crystalline phases of the annealed films were characterized by X-Ray Diffraction, using *Philips X-Pert MPD* equipment, with Cu-Kα X-Ray radiation and λ = 1.5406 Å.

Scanning Electron Microscopy (SEM) mainly serve for microstructure and thickness characterization. The equipment used for SEM characterization was *Hitachi*® model *S4100*, and in some cases *Hitachi*® model *SU-70*. The acceleration voltages utilized for dense and porous films were 15 and 25 kV respectively, since higher values permit a better penetration for a 3D visualization of the porous network.

The study for the presence of BFO's rhombohedral phase presence was assisted by Raman Spectroscopy. The equipment used was *JY Horiba LabRam* model *HR800*, with a high resolution 800 mm focal length spectrometer. The laser beam utilized was Argon at 532 nm (*Ventus*).

Ferroelectric properties were investigated via Piezoresponse Force Microscopy (PFM). The microscope used was *Veeco*, equipped with *Nanoscope III, Digital Instruments*. The silicon cantilever-tips used were coated with Al, produced by *NANOSENSORS*^{TM} model *PPP-NCHR*, with length of 125 μm, resonant frequency of 204-497 kHz and force constant of 10-130 N/m.

Magnetic properties were measured by Superconducting Quantum Interference Device (SQUID). The measurements were conducted under constant temperature at 300 K and for varying magnetic field. The equipment used was *Quantum Design – MPMS* (Centro de Física Matéria Condensada, Faculdade de Ciências, Universidade de Lisboa).

CHAPTER 4

Results and Discussion

4. Results and Discussion

4.1 $BiFeO_3$ Dense Films

As mentioned in Section 3.1.1, a series of efforts were conducted in order to prepare the necessary BFO dense thin films, our reference point for the investigation of the role of porosity. In order to create the best possible conditions, so that a reasonable comparison between the two structures could be made, the same preparation conditions were used, i.e. the same type of solvents and same annealing temperatures.

However, due to the weak adhesion of the sol on the substrate, a small amount of Pluronic F127 polymer (5mg) was added. Since in this case some porosity was observed, an extra drying step was applied, by placing the deposited film on a hot-plate at 120 ^{o}C for 2 min, prior to the thermal treatment for template removal and crystallization annealing, as proposed by Coondoo *et al.*[73]. Deposition temperature control (70 ^{o}C), in combination with the immediate contact with the hot-plate, and the subsequent treatment at 300 ^{o}C for 3 min, solved the problems of pore occurrence, for medium and high withdrawal velocities.

4.1.1 Effect of Withdrawal Velocity on Film Thickness

Table 4.1 presents the different cases of withdrawal velocities used for the preparation of dense films, together with the respective thicknesses, as measured by the cross-section SEM images (**Figure 4.1**), with the help of the image processing program *ImageJ*. Sample D100 was not characterized, mainly due to stabilization difficulties on the sample holder. Cross-section images require perpendicular positioning of the sample and owing to disproportionate dimensions, there is always a small movement during the acquisition of the images, resulting in distortion of the real dimensions. It should be mentioned that some inhomogeneity was detected in the film thickness, thus the thicknesses presented in **Table 4.1** were calculated as the average of measurements taken in various positions of the cross-section SEM images.

Table 4.1 Dip-coating withdrawal velocities and respective thicknesses for BFO dense films, annealed at 600 ^{o} C.

Sample Identification	Withdrawal Velocities (mm/min)	Thickness (nm)
D5	5.58	100 ± 14
D10	10.58	125 ± 6
D29	29.58	195 ± 10
D45	45.66	215 ± 8
D100	100	-
D150	150	230 ± 7
D180	180	285 ± 6

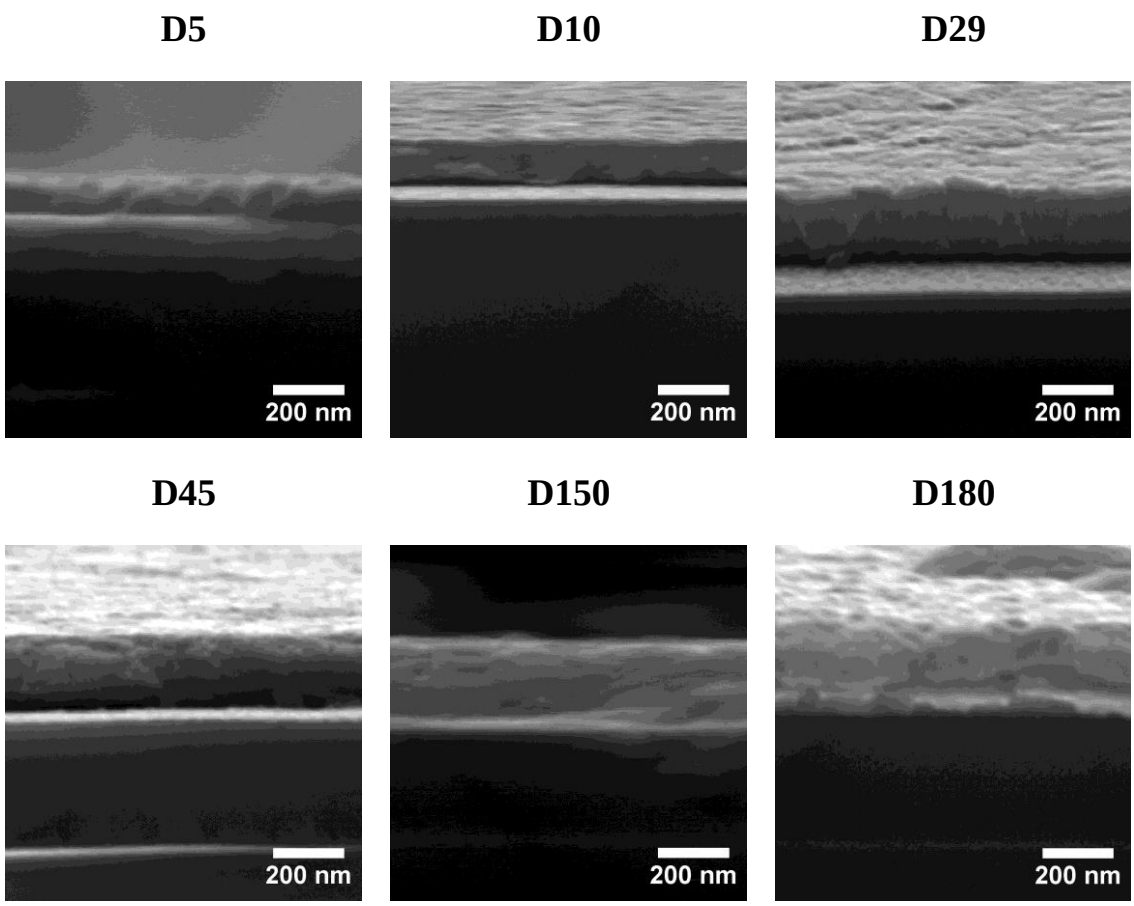

Figure 4.1 Cross-section SEM images for dense BFO films prepared with different withdrawal velocities ranging from 5.58 to 180 mm/min. Film thickness increases with increasing withdrawal velocity.

The thickness of BFO dense films varied between 100 and 285 nm, as can be seen in **Table 4.1** and **Figure 4.1**. Thickness increases with increasing withdrawal velocity, meaning that the velocities chosen belong to the draining regime (Section 2.6.2, **Figure 2.19**).[53,56] Lower velocities were also tested, however due to adhesion problems the films presented inhomogeneous zones with clear difference in deposited mater, hence thickness.

In **Figure 4.2**, the effect of the withdrawal velocity on the film thickness is presented. A logarithmic scale was used for the x-axis and the units are presented in mm/s, instead of mm/min that appear in **Table 4.1**, in order to be able to make a comparison with Faustini *et al.*[56]. As shown in Section 2.6.2, the draining regime exists for withdrawal velocities higher than 0.1 mm/s, which is also observed for the current case. However, no direct conclusions can be made concerning the limits of the draining regime. Undoubtedly, withdrawal velocity-thickness relation depends on the nature of solvents, precursors, solution viscosity, chamber temperature and humidity. In addition, no lower withdrawal velocities were possible to investigate, which gives no clues about the capillary regime for the specific solution. Importantly, viscosity measurements are required for inclusion of such extreme values of withdrawal velocities.

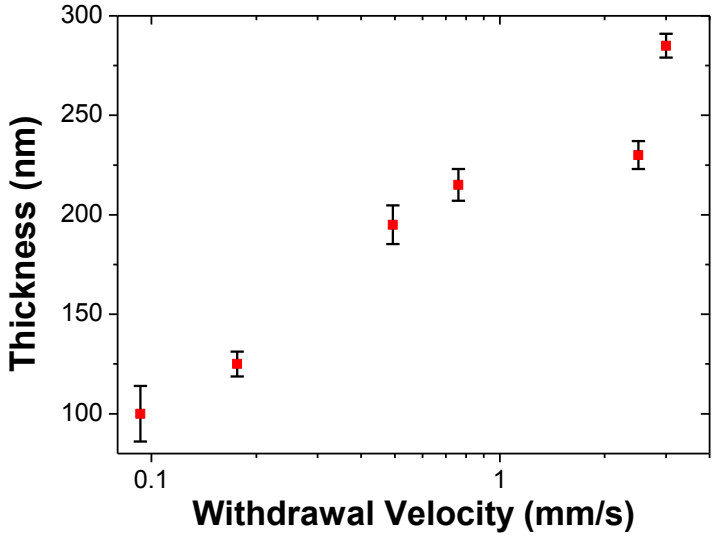

Figure 4.2 Withdrawal velocity effect on thickness for the BFO dense thin films, showing increase of film thickness with increasing withdrawal velocity.

In **Figure 4.3**, the top view SEM microstructures of the BFO films for different withdrawal velocities are presented. For higher velocities that correspond to thicker films a more dense structure was obtained and samples D29, D45, D100 and D150 show a considerably higher densification, apart from some inhomogeneity in grain distribution and the appearance of some individual pores. At these velocities, the draining regime dominates and the films are thicker. Drying process in thicker films lasts longer, since it occurs with the evaporation of the exterior surface and, apart from the increase of the gel aging time, there is more time for the particle ordering.[53] However, samples D5 and D10, deposited at lower withdrawal speeds, present a clear porous structure. This can be explained by the fact that at low withdrawal velocities, at which capillary forces start to influence the solvent-inorganic precursor interaction, solvent evaporation occurs faster than the motion of the drying line between the vapour, the liquid and the solid phase.[56] This results in inhomogeneous film formation.

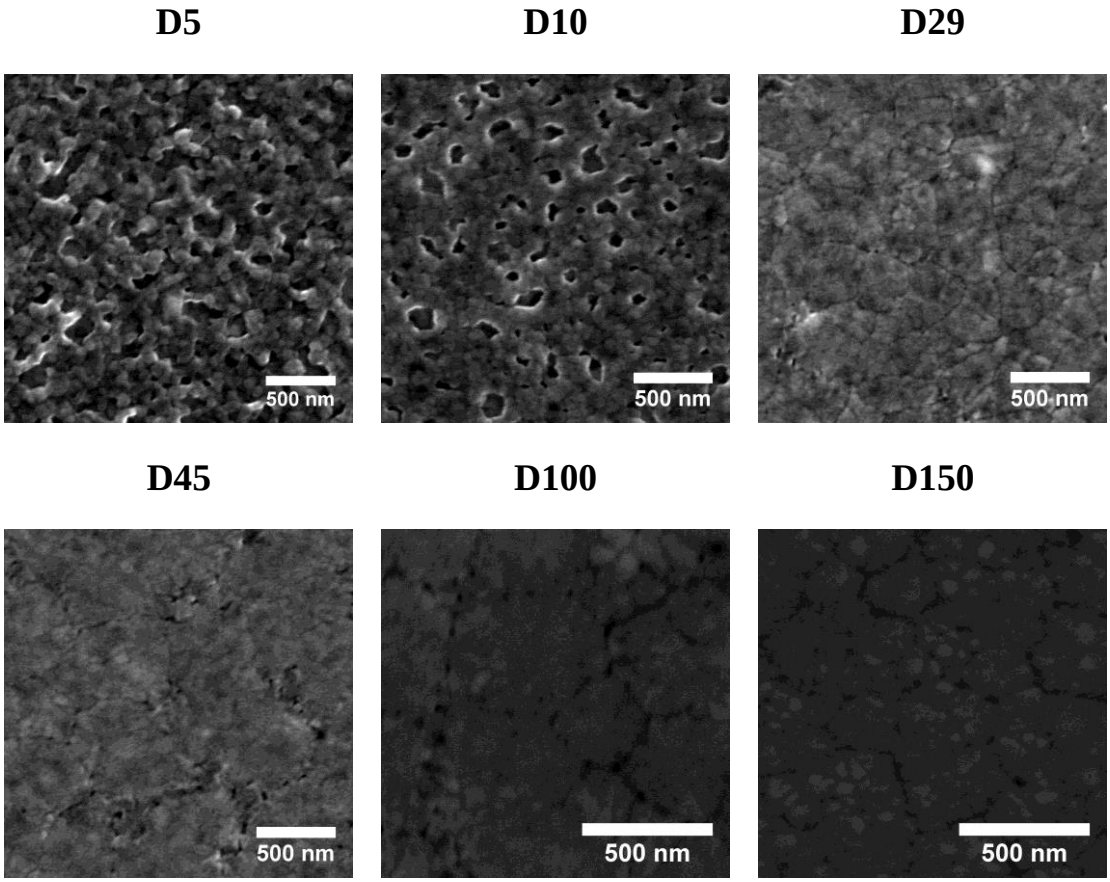

Figure 4.3 Top view SEM micrographs of BFO dense films prepared with different withdrawal velocities and annealed at 600 ^{o}C. Increasing withdrawal velocity led to enhanced film densification.

4.1.2 XRD Results

The XRD patterns of the BFO films with varying thickness of 100, 195 and 230 nm (samples D5, D29 and D150 respectively) are presented in **Figure 4.4**. All films present the main peaks of the rhombohedral phase of BFO. The peak appearing at around 29 2θ ^{o} can be attributed to the $Bi_2Fe_4O_9$ secondary phase, with cubic structure and (121) orientation. The flattening close to 46 2θ ^{o} can be due to a combination of the Pt peak with orientation (200) and the BFO monoclinic phase, which presents three intense peaks in that region. However, also monoclinic $BiFeO_3$ and rhombohedral Fe_2O_3 impurities can contribute for the occurrence of multiple peaks close to that region, concerning the rhombohedral and monoclinic phases of $BiFeO_3$, as well as the secondary phases. Since D150 film is thicker (230 nm thick), more intense peaks are visible, whereas for the D5 case (100 nm thick), substrate clamping could have provoked the formation of off-stoichiometric phases, as well as monoclinic symmetry.

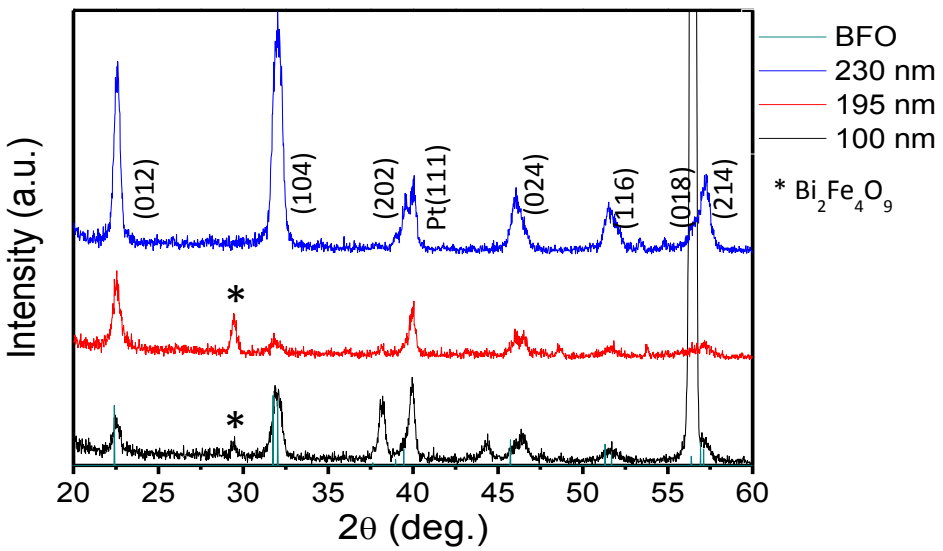

Figure 4.4 XRD patterns of dense BFO films, 100, 195 and 230 nm thick (samples D5, D29 and D150) and annealed at 600^{o}C.

4.1.3 PFM Studies

By the use of Piezoresponse Force Microscopy (PFM), topography and PFM images of dense samples were obtained simultaneously. All images were composed with detection of the vertical signal, thus imaging of out-of-plane polarization was conducted. The amplitude of the applied ac voltage was 5 V and the frequency 50 kHz.

As shown in **Figure 4.5**, the first column corresponds to the topography image and the second to the piezoresponse. Topography basically images the film surface, where light regions correspond to heights and dark ones to lows. However, due to the use of contact mode, required for the monitoring of piezoelectric behaviour, size effects take place resulting in misrepresentation of the real grain size and morphology of the sample in investigation.

The PFM images are composed by dark, medium and light domains. The first correspond to ferroelectric domains with substrate-oriented polarization (downwards, notation ⊗) and the light ones to tip-oriented polarization (upwards, notation ⊙) (**Figure 4.5**). The medium domains could result owing to a series of cases.[68] Firstly, the polycrystalline nature of thin films produced via sol-gel process induces a random polarization. Integration of the piezoelectric response over film thickness results in zero total polarization. In addition, the relatively small grains, comparing to the film thickness, tend to reinforce polarization annihilation, since naturally domains are related with the grain structure. The latter statement should not be confused with topography-piezoresponse correlation, which in order to reveal truthful piezoelectric response demands independence between the two images. In other words, domain contrast should not coincide with grain contrast, which is related to the topography. Another case, usually characteristic of the stripe-like epitaxial BFO thin films (Section 2.7.3), is that of the in-plane oriented domains, which of course for the case of out-of-pane imaging have very low or even zero contribution. Furthermore, lack of polarized domains could result from the highly complex multiphasic character of BFO, with the occurrence of non-ferroelectric phases (orthorhombic, monoclinic and cubic), secondary phases and impurities (Section 2.5.2). Lastly, if the amplitude of the ac voltage used for the visualization of the domains is close to the magnitude of the coercive field, switching of the polarization could take place, following the same frequency, thus producing no domain contrast.

The topography and PFM images for samples with increasing thickness D5, D29 and D150 are presented in **Figure 4.5**. The samples were annealed at 600 ^{o}C. All samples present similar domain geometry and distribution. The domain configuration appears to be continuous, apart from the case of D29, which presents some areas with no response, mainly due to topography anomalies, as can be confirmed by the respective topography image.

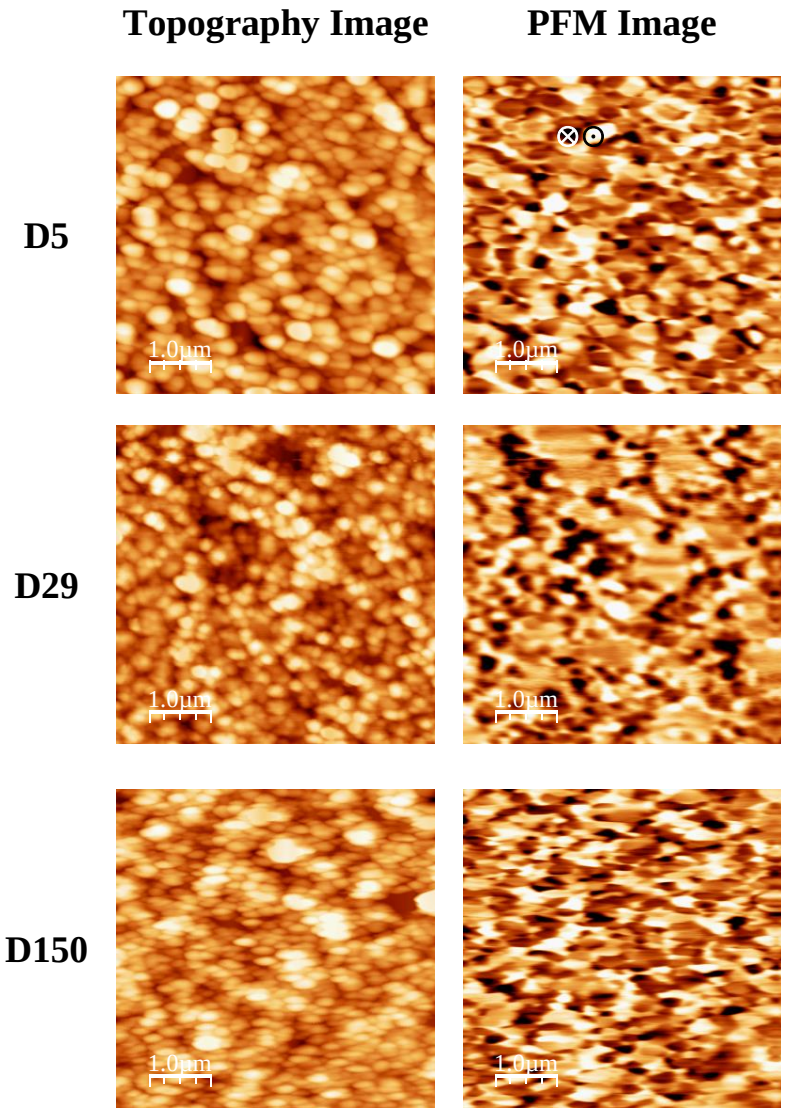

Figure 4.5 Topography and PFM images of 5μm x 5μm scanning area for samples with increasing thickness of 100, 195 and 230 nm (samples D5, D29 and D150 respectively), annealed at 600^{o}C. Notations ⊙ and ⊗, for upwards and downwards domain orientation respectively.

The ferroelectric domains show a mosaic-like structure, similar to the one presented by Coondoo *et al.* for BFO films prepared by sol-gel.[73] Such a pattern differs from the stripe-like domains of BFO epitaxially grown thin films, mostly due to the polycrystalline character of sol-gel derived films, as well as the random grain formation and growth during crystallization. Although BFO's piezoelectric coefficient is smaller than other perovskites, as referred in Section 2.5.1, the domains present high intensity and relatively large size, possibly due to the multiferroic character of BFO and the occurring magnetoelectric coupling taking place mostly at the domain walls, as discussed in Sections 2.5.3 and 2.7.3.

BFO films with 230 nm thickness (sample D150) were thoroughly studied, due to a more regular and homogenous surface morphology. In **Figure 4.6**, the topography and PFM images for different scanning areas of 5 μm x 5 μm, 3 μm x 3 μm, 2 μm x 2 μm and 1 μm x 1μm are shown. Upwards and downwards polarized domains are equally distributed, however the appearance of regions with intermediate contrast is highly frequent.

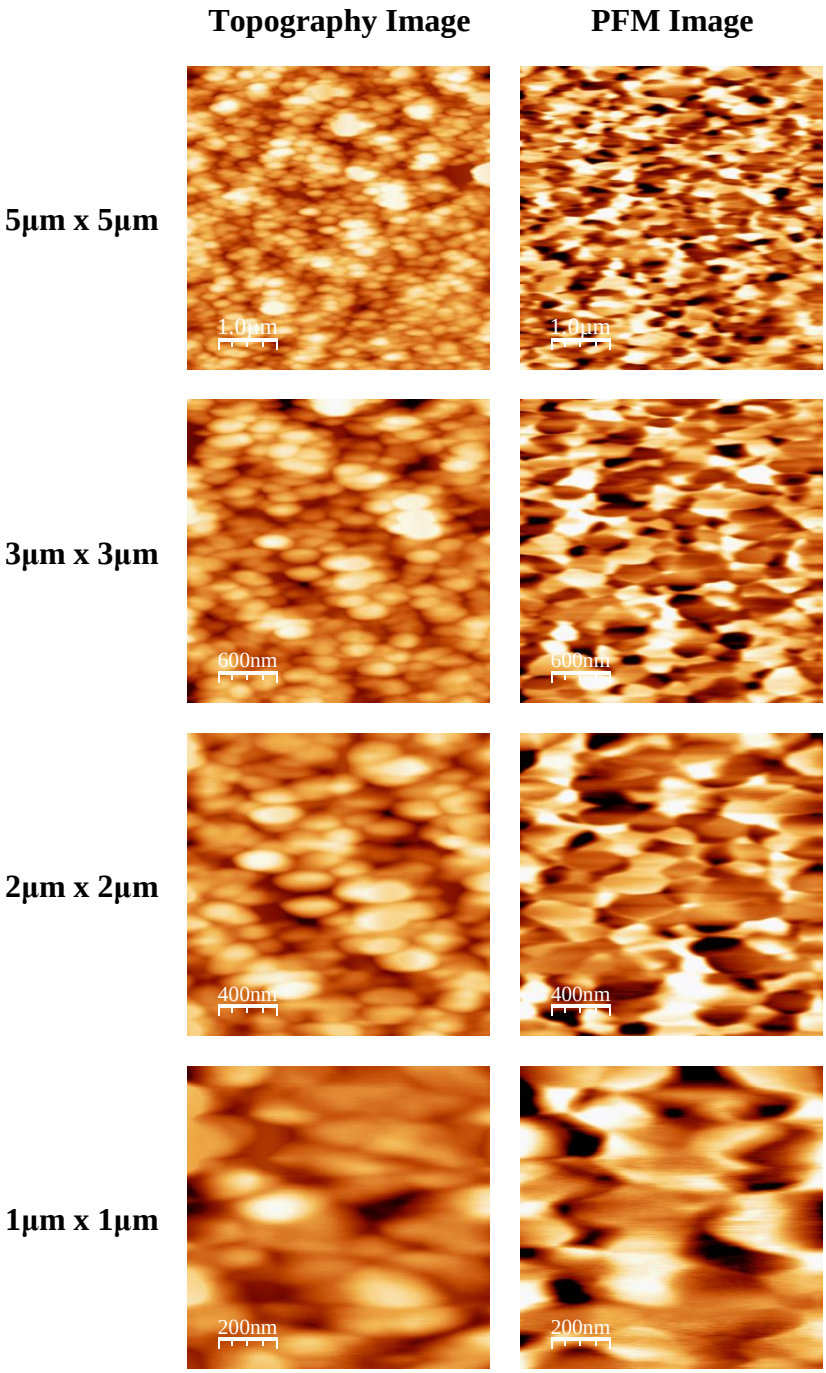

Figure 4.6 Topography and PFM images of 230 nm thick BFO dense film (sample D150) annealed at 600 ^{o}C.

The relatively low roughness of the surface makes the verification of genuine domains less complicated, since irregular topography can provoke artefacts in the piezoresponse image, easily confused with ferroelectric domains. To avoid such confusion, areas in the topography image presenting homogenous grain colour (thus situated at the

same height) were chosen and correlated with the respective area in the PFM image. If domains with contrast can be observed for such a region, then the domains in question correspond to real ferroelectric domains.

Figure 4.6 depicts the smaller scanning areas (2 μm x 2 μm and 3 μm x 3 μm) of sample D150, taken by zooming in the first image (5 μm x 5 μm), except for the case of 1μm x 1μm. Domain structure, of course apart from the loss of resolution due to amplification, maintains exactly the same morphology and contrast.

Small scanning areas also facilitate the local piezoelectric hysteresis loop measurements. The latter technique is based on the application of dc voltage pulses, which are subjected to a loop-like increase and decrease of the amplitude, with the necessary application of negative potential, for induction of polarization switching. In order to carry out these measurements, a ferroelectric domain should be chosen and the tip should stand still to a specific point on the domain. Hence, amplification of domains makes sure that the tip will be standing on a ferroelectric domain and not on a non-ferroelectric one or an inter-domain region.

Figure 4.7 presents the dc voltage pulses applied for the measurement of the local piezoelectric hysteresis loop, with pulse duration of 2 seconds and intervals of zero voltage of 1 second. Apart from the dc voltage required for the stimulation of piezoelectric behaviour, an ac field is applied simultaneously, mainly for the detection of the film reaction during the zero voltage intervals between the pulses. This ac voltage should be relatively low comparing to the dc bias, so that polarization removal would be avoided during piezoresponse reading. The small ac voltage had amplitude of 2 V and 50 kHz frequency. The maximum dc voltage was of 15 V and the step between each pulse is 1.5 V.

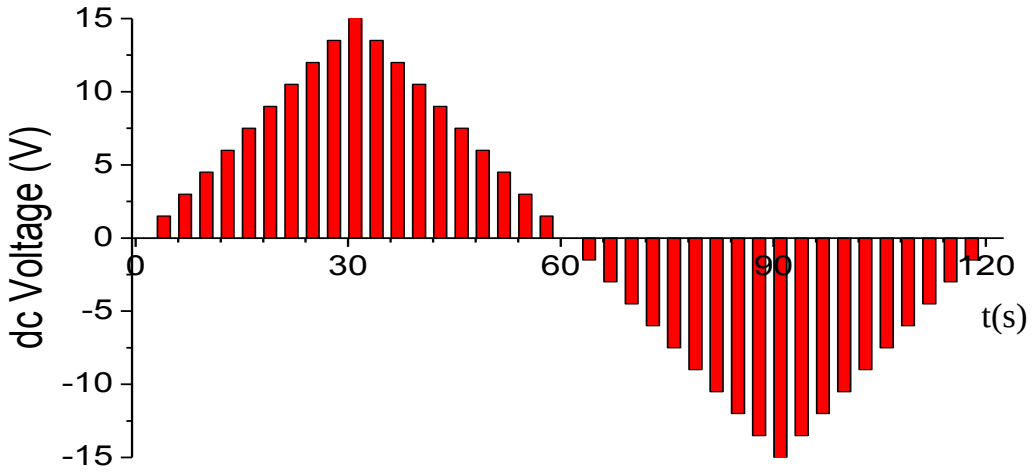

Figure 4.7 Dc voltage pulses applied for the local piezoelectric hysteresis loop measurements. Each pulse lasts for 2 sec and the zero voltage intervals for 1 sec.

In **Figure 4.8**, the local piezoelectric hysteresis loops for samples with increasing thickness of 100, 195 and 230 nm (samples D5, D29 and D150 respectively) are presented. Measurements were conducted at various domains for each film, preferably the most intense ones in order to ensure the occurrence of the polarization switching, the cases which presented the medium polarization saturation were used for comparison between the samples.

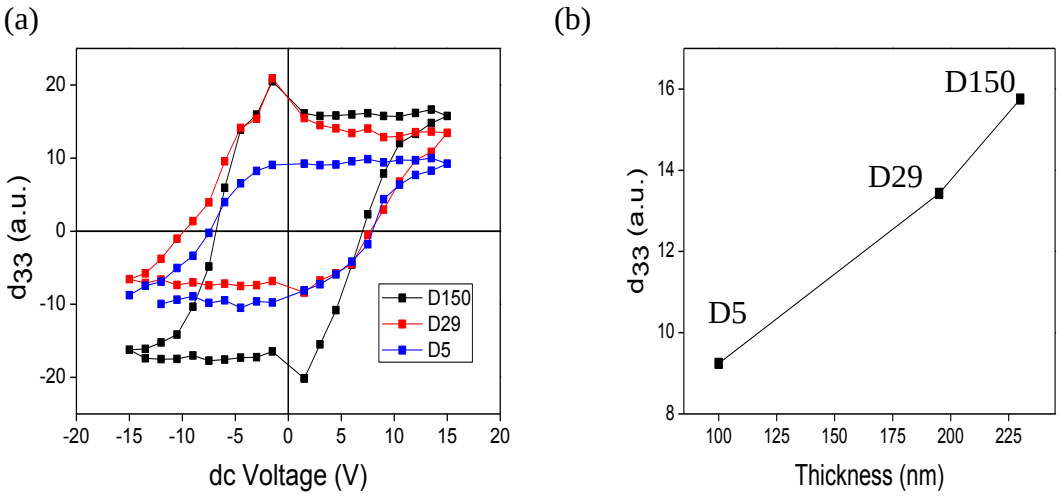

Figure 4.8 (a) Local ferroelectric hysteresis loop for BFO films of 100, 195 and 230 nm thickness (samples D5, D29 and D150 respectively). (b) Piezoelectric coefficient as a function of film thickness, showing increase with increasing thickness.

A slight increase in the saturation polarization with increasing thickness can be observed. High thickness corresponds to large grain and crystallite size, which results in the slightly stronger piezoelectric response. Nevertheless, thickness is a macroscopic characteristic of the films, whereas the current piezoresponse measurements are local, which implies that no absolute and direct correlation can be made. In some cases, impurities and elevated inhomogeneity can result in the formation of highly polarized domains, while at the same time large regions of the film present zero piezoresponse. The piezoelectric coefficient measured in these cases reaches even higher values than those observed in the thickest films (~230nm).

4.1.4 Magnetic Characterization Results

The magnetic properties of dense BFO films were measured by Superconducting Quantum Interference Device (SQUID). In order to subtract the substrate signal from the one produced by the film, a measurement of the magnetization of the substrate under the same magnetic field variation and the same temperature (300 K) was carried out.

The magnetic moment measurements at 300 K for the BFO films have great importance, revealing for this model case of single-phase magnetoelectric multiferroic the uniqueness of room temperature multiferroic behaviour. A mass normalization is normally required, in order to present the apparent magnetization related to a specific amount of matter. For the current measurements the samples were cut in squares of 0.5 cm x 0.5 cm. Unfortunately, no easy and approachable technique was possible to be followed in order to measure the quantity of the mass deposited on such small areas. Hence, in all the SQUID results presented in this work, the magnetic response is given by the total magnetic moment measurement. As a result, a comparison with magnetization values referred in literature cannot be made.

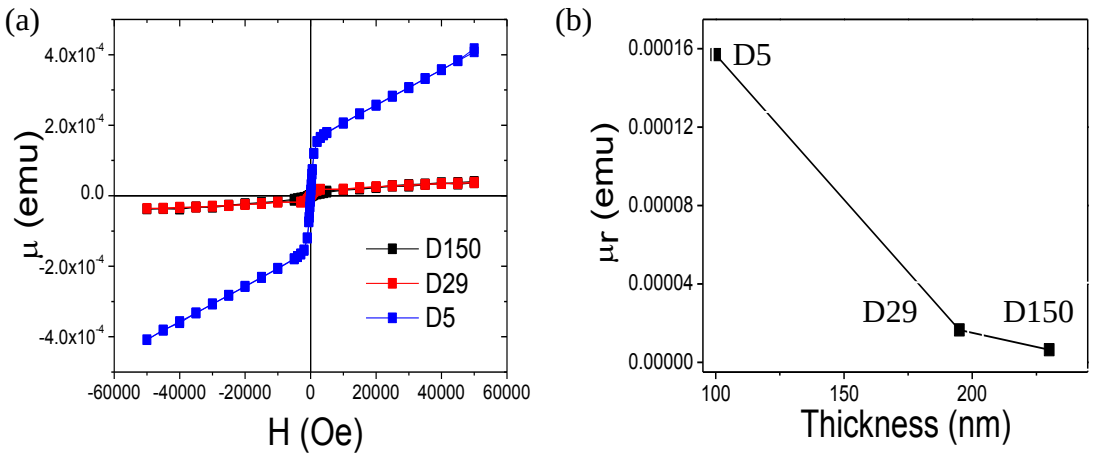

Figure 4.9 (a) Magnetic moment measurements under magnetic field variation at 300 K for BFO dense films of 100, 195 and 230 nm thickness (samples D5, D29 and D150 respectively), annealed at 600 ^{o}C. (b) Remanent magnetization as a function of thickness for the dense samples D5, D29 and D150.

In **Figure 4.9**, the magnetic moment measurements of samples with increasing thickness D5, D29 and D150 are presented. The antiferromagnetic behaviour displays an approximately linear relation between the applied magnetic field and the resulting magnetization and it dominates the magnetic response at higher magnetic fields. The magnetization increasing rate with the application of the magnetic field corresponds to the antiferromagnetic susceptibility of the material. For low magnetic fields, one can observe the manifestation of a slight hysteretic behaviour due to uncompensated magnetic moments.

An intense difference can be observed for the case of 100 nm thick BFO films (sample D5), in comparison to the other samples. This can be interpreted by the possible occurrence of impurities, as discussed in Section 4.1.2, which could present ferromagnetic behaviour, resulting in the emergence of the low field weak ferromagnetic response. Furthermore, the highly porous microstructure observed for these films can be an additional factor for such a divergence. As discussed in Section 2.5.3, large surface anisotropies due to low film thickness, in combination with high roughness, relatively small grains (average size of 30nm), low crystallinity texture and possible presence of out-of-plane surface spin structure, give rise to uncompensated magnetic moments, thus increased magnetization.[3,4,46,47] As a result, decrease of remanent magnetization with increasing film thickness can be observed in **Figure 4.9** (b).

In **Table 4.2**, the antiferromagnetic susceptibility χ_{AF} and the remanent magnetization μ_r are presented for the BFO dense films 100, 195 and 230 nm thick (samples D5, D29 and D150). The antiferromagnetic susceptibility, characteristic of the material and derived from the slope of the graph at high magnetic field values, should have been the same for all the samples. However, since the total magnetic moment measured was not normalized concerning the mass contribution, there is a slight increase with increasing withdrawal velocity, due to the thickness increase. The samples' magnetic response can be obtained by the remanent magnetization, which corresponds to the point at which the referred slope line meets the y-axis. Nevertheless, this assumption should be considered with care, due to the possible error introduced by the lack of normalization in the antiferromagnetic susceptibility.

Table 4.2 Antiferromagnetic susceptibility and remanent magnetization for samples D5, D29 and D150, annealed at 600 ^{o}C.

Sample Identification	**Thickness (nm)**	**χ_{AF} (10^{-10} emu/Oe)**	**μ_r (10^{-5} emu)**
D5	100 ± 14	50 ± 0.2	15.7·± 1.5
D29	195 ± 10	4.32·± 0.2	1.65·± 1.5
D150	230 ± 7	7.86·± 0.2	0.63·± 1.5

Summarising for the BFO dense films, increase in withdrawal velocity results in increasing thickness, which leads to increase in the local piezoelectric coefficient d_{33} and decrease in the remanent magnetization μ_r.

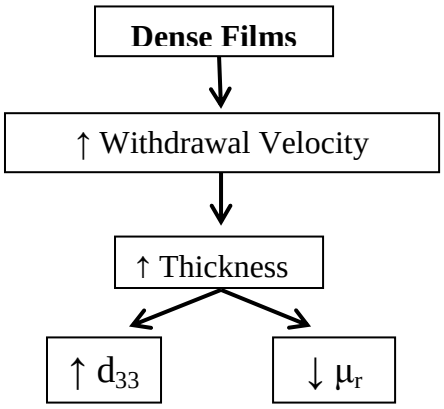

Figure 4.10 Schematic representation of the withdrawal velocity effect on thickness and multiferroic properties for the series of dense films.

4.2 $BiFeO_3$ Porous Films

4.2.1 Studies of the Template Concentration Effect

In **Table 4.3**, the different samples prepared by increasing the solution template quantity are presented. All films were deposited at a velocity of 29.58 mm/min. The initial use of 60 mg in the solution presented highly inhomogeneous microstructure, hence the content of the template was decreased for a better micelle distribution along the film.

Table 4.3 Template quantities used in the preparation of BFO porous films and the respective film porosity densities, pore size and porosity contribution. The pore size corresponds to the pore diameter. The porosity density relates to the number of pores for a specific area. The surface porosity contribution corresponds to the ration between the surface area occupied by the pores and the total area of the film.

Sample Identification	Template Mass (mg)	Porosity Density (10^{-4} nm^{-2})	Pore Size (nm)	Surface Porosity Contribution (%)
P24	24	2.2·± 0.05	38 ± 1.9	25 ± 2.6
P30	30	1.8·± 0.09	52 ± 2.6	38 ±4
P36	36	1.6·± 0.09	70 ± 3.5	62 ± 6.3
P48	48	1.3·± 0.10	74 ± 3.7	56 ± 5.7
P60	60	0.7·±0.15	81 ± 4	36 ± 3.7

In **Figure 4.11**, the SEM micrographs of P60, P48, P36, P30 and P24 (with the content of the template decreasing with this order) are presented. All the BFO films are visibly porous and the size and degree of order of the porosity varies with the content of the polymer. It is clearly visible that as the content of polymer increases the porosity of the films increases, but pore organization is also directly affected by the polymer content. An enhanced degree of order was obtained for the films with the lowest content of polymer, the cases of P30 and P24 films. For the films with the highest polymer content (sample P60), the excess of template lead to the coalescence of the porosity and also to the formation of bigger pores in comparison with the films prepared with lower polymer

contents. P48 films show an organised network of pores with the biggest pore size among these organised pore networks; the pore size was calculated to be ~ 74 nm. It is also visible and related with the amount of the template that in this case the pore walls are thinner than for the films with lower polymer amounts. As the polymer content decreases the pore size decreases and the pore organization increases.

Pore size, porosity density and surface porosity contribution were calculated by the SEM images (**Figure 4.11**) by the use of the image processing program *Image J*, as presented in **Table 4.3**. The pore size corresponds to the pore diameter. The porosity density was measured as the number of pores for a specific area. Finally, surface porosity contribution was calculated by the ratio between the surface area occupied by the pores and the total area of the film. Calculation of the actual porosity density along the whole film volume was very difficult, since cross-section SEM images lacked resolution. Thus, the presented densities correspond to the surface porosity density and not to the bulk density.

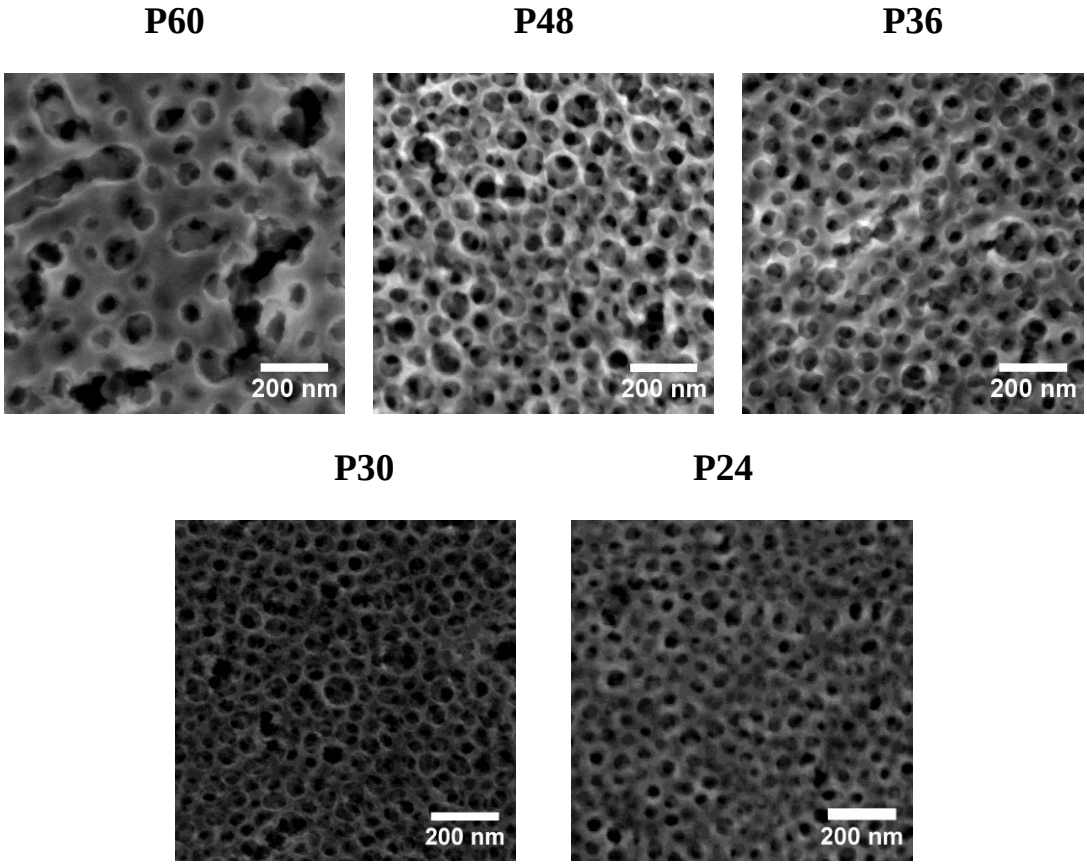

Figure 4.11 SEM micrographs of BFO porous films P60, P48, P36, P30 and P24, deposited with a velocity of 29.58mm/min and annealed at 400^{o}C.

Increasing the template quantity resulted in increasing pore size and decreasing porosity density (**Figure 4.12** (a) and (b) respectively). The decrease in the surface porosity contribution as a function of the solution template mass for samples P48 and P60 (**Figure 4.12** (c)) results from the formation of large micelles, as well as the presence of large template aggregates, which led to the coalescence of the pores and the formation of big craters.

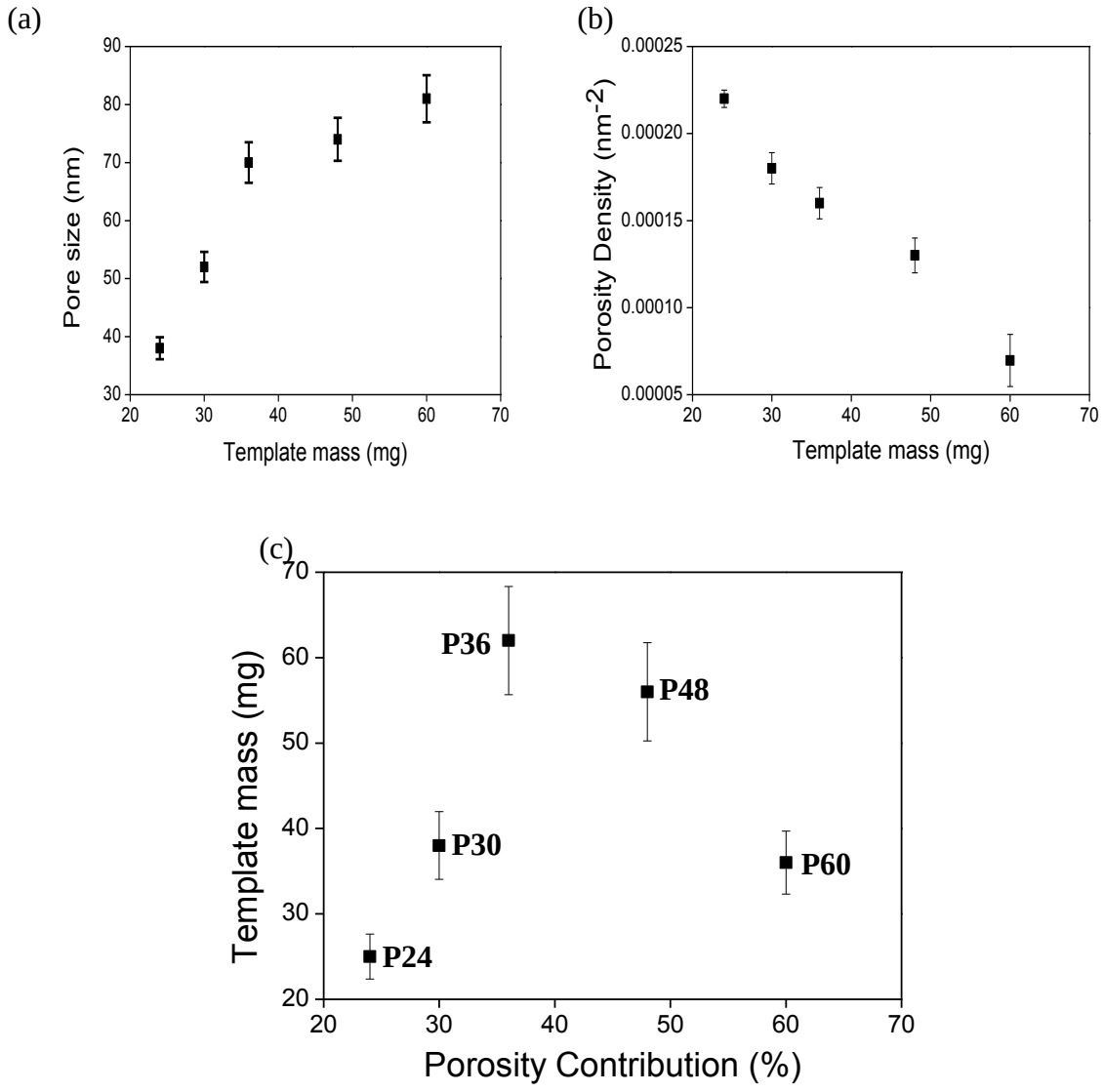

Figure 4.12 (a) Pore size, (b) surface porosity density and (c) surface porosity contribution as a function of solution template mass for BFO films annealed at 600 ^{o}C.

- **XRD Results**

In **Figure 4.13**, XRD patterns for the samples P24, P30 and P60, annealed at 600 ^{o}C, are presented. The most intense peaks correspond to the $BiFeO_3$ rhombohedral phase. Samples P24 and P60 present higher degree of crystallinity, which results from the lower porosity contribution, as presented in **Table 4.3**. For samples P24 and P60, the peak appearing at around 28 2θ ^{o}. implies the presence of $Bi_2Fe_4O_9$.

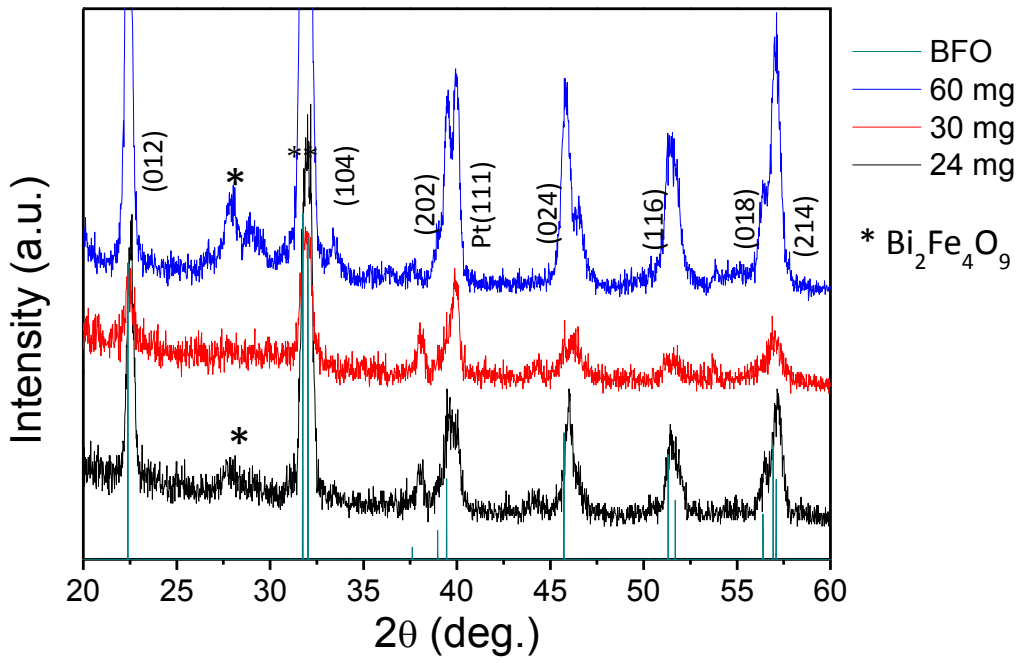

Figure 4.13 XRD patterns for BFO porous films with 24, 30 and 60 mg of solution template mass, with 29.58 mm/min withdrawal velocity and 600 ^{o}C annealing temperature.

- **PFM Studies**

In **Figure 4.14**, the topography and PFM images of samples P24, P30 and P60 are presented. The same conditions as those of the dense film characterization were used. All samples present similar domain configuration. However, the high degree of surface inhomogeneity for the sample P60 made difficult the acquisition of the images, thus the topography image presents grain deformation. The elevated roughness also affected the detection of piezoresponse, revealing regions with zero polarization.

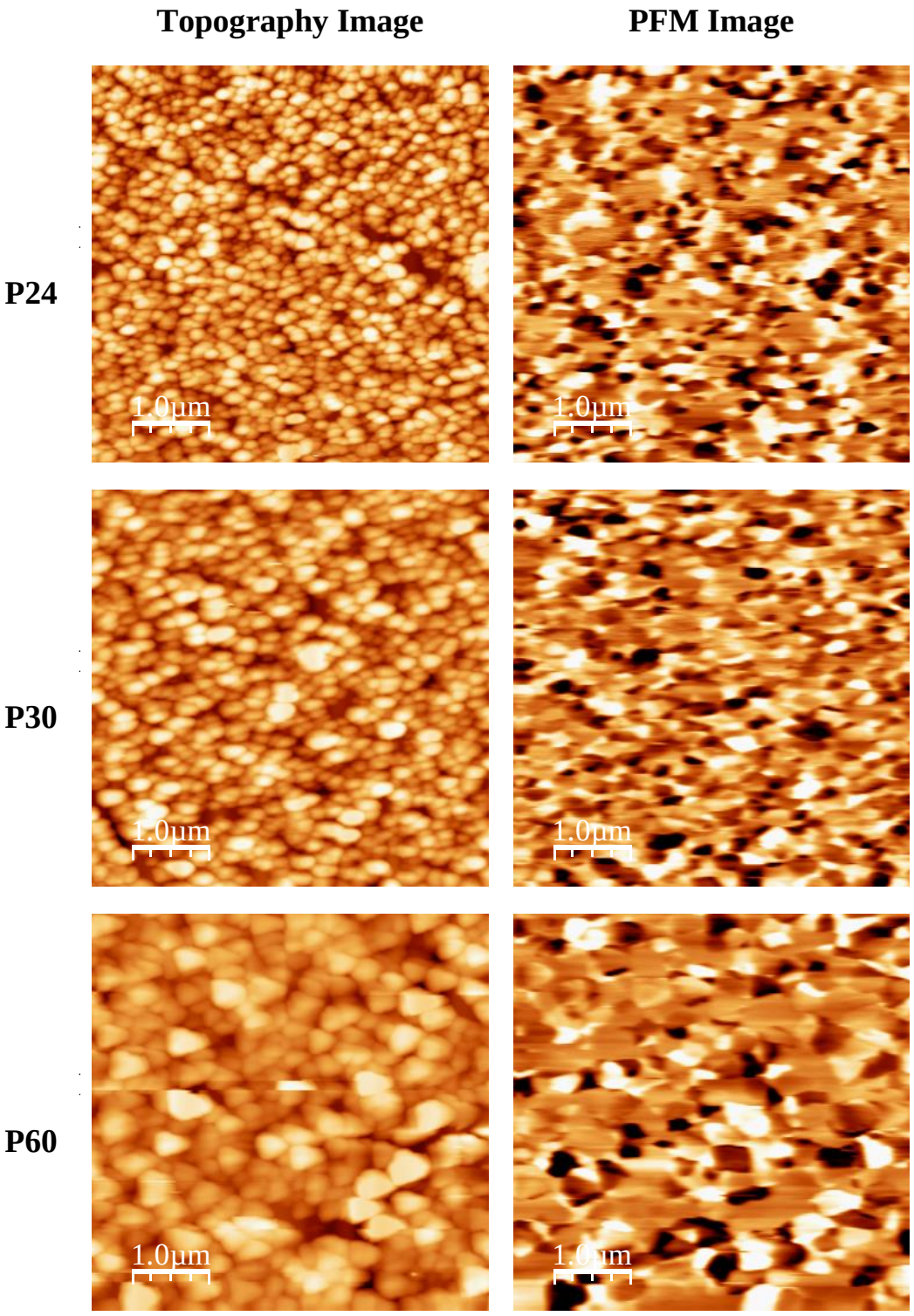

Figure 4.14 Topography and PFM images for BFO porous films with increasing template quantity (samples P24, P30 and P60), annealed at 600 ^{o}C, for 5 µm x 5 µm scanning area.

The local piezoelectric hysteresis loops were measured for P24, P30 and P60 films. P30 films show smaller saturation polarization, probably due to the thinner inorganic network induced by the higher porosity contribution, as seen in **Figure 4.11** and **Figure 4.12** (c). The increase of template mass in the solution caused increase of the pore size and decrease of porosity density. As a result, the formation of larger grains was allowed for samples with lower degree of pore distribution, and since the most intense domains were selected for the current study, higher piezoelectric coefficients were detected for samples P24 and P60. Once again, the phenomenon of strong polarized domains, isolated by surrounding areas with weak polarization was repeatedly observed in highly inhomogeneous samples.

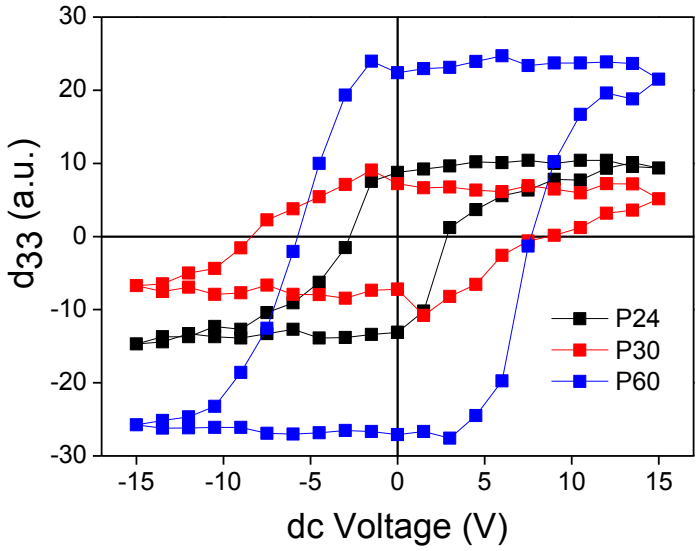

Figure 4.15 Local piezoelectric hysteresis loop measurements for BFO porous films P24, P48 and P60, annealed at 600 ^{o}C. Higher piezoelectric response was observed for the porous films with lower degree of porosity contribution (films P24 and P60).

- **Magnetic Characterization Results**

In order to investigate the effect of template concentration on the magnetic behaviour of the porous films, magnetic moment measurements upon increasing magnetic field at 300 K were carried out for the porous films P24 and P60 and compared with the dense films D29 (prepared with the same withdrawal velocity and annealed at 600 ^{o}C), as presented in **Figure 4.16**.

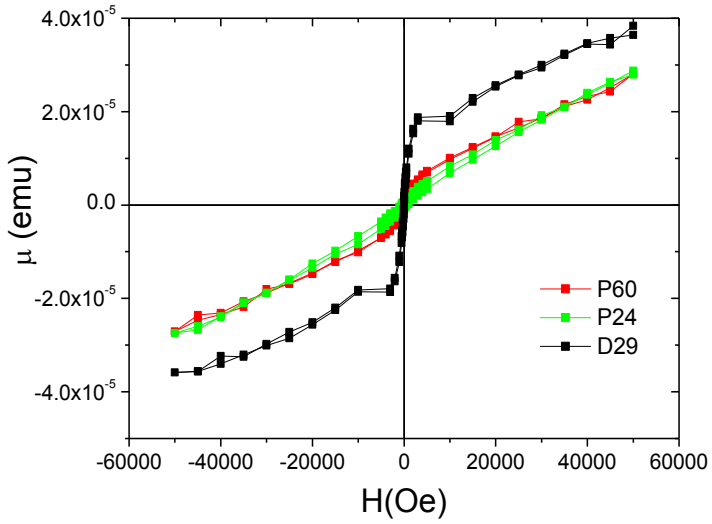

Figure 4.16 Magnetic moment measurements under magnetic field variation at 300K for samples D29, P24 and P60, annealed at 600^{o}C.

A comparison between the magnetic response, the thickness and the surface porosity contribution is presented in **Table 4.4**. For the case of the dense films porosity contribution is considered to be 0%.

Table 4.4 Antiferromagnetic susceptibility and remanent magnetization, thickness and surface porosity contribution for BFO porous P24 and P60 and dense D29 films, annealed at 600 ^{o}C.

Sample Identification	**Thickness (nm)**	**Porosity Contribution (%)**	**χ_{AF} (10^{-10} emu/Oe)**	**μ_r (10^{-5} emu)**
D29	195 ± 10	0	4.32 ± 0.2	1.65·± 1.5
P24	170 ± 8.5	25 ± 2.6	4.27·± 0.2	0.61·± 1.5
P60	160 ±7	36 ± 3.7	5.42·± 0.2	0.18·± 1.5

There is again a slight divergence in the values of the antiferromagnetic susceptibility, due to lack of mass normalization in the measurements. The results show the opposite behaviour of what was expected, as increase in remanent magnetization with decreasing porosity contribution is presented. In addition, the otherwise predicted effect of thickness on magnetization is not observed in this case, since there is increase in magnetic response with increasing thickness. Both phenomena should have yielded increase in the uncompensated magnetic moments, due to higher degree of surface roughness and anisotropy. The explanation lies in the lack of thorough investigation of each sample, since a more reliable technique for the thickness and porosity characterization should have been employed. Nevertheless, the higher frequency of ferroelectric domains observed for the samples D29 and P24 signifies enhanced ferroelectric behaviour and naturally higher magnetoelectric coupling, in addition to the domain wall induced magnetization.[48,49] Furthermore, the random grain size distribution together with the larger grains observed in P60 can stimulate the formation of larger ferroelectric domains, thus smaller wall network.

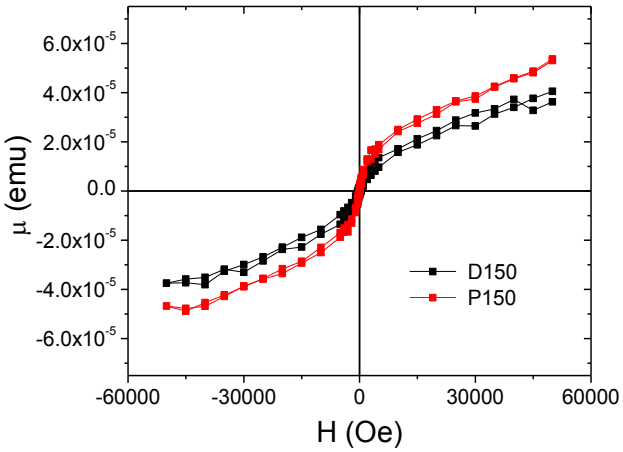

Figure 4.17 Magnetic moment measurements under varying magnetic field at 300K for samples P150 and D150.

In **Figure 4.17**, a comparison between a dense and a porous film is presented. For the case of higher withdrawal velocity of 150 mm/min (**Figure 4.17**), porous sample P150 shows a higher remanent magnetization, as expected by the presence of surface anomaly induced magnetization. The two thicknesses do not present large deviation, with 230 nm and 240 nm for P150 and D150 respectively, thus the uncompensated spins result mainly from the presence of porosity.

4.2.2 Studies of the Annealing Temperature

The loss of porosity order at elevated temperatures led to the need of a deeper understanding of grain growth and crystallization procedure, and how this affects the porosity network. The sample chosen for this study is P30 (with 29.58 mm/min withdrawal velocity, 0.3 M sol-gel concentration and 30 mg solution template mass), since it presented a relatively homogeneous porous structure.

Figure 4.18 presents the SEM micrographs of P30 films for six different annealing temperatures, ranging from 400 to 650 ^{o}C with a dwell time of 5 min. The gradual loss of porous structure can be observed above 550 ^{o}C, which corresponds to the beginning of the crystallization process.

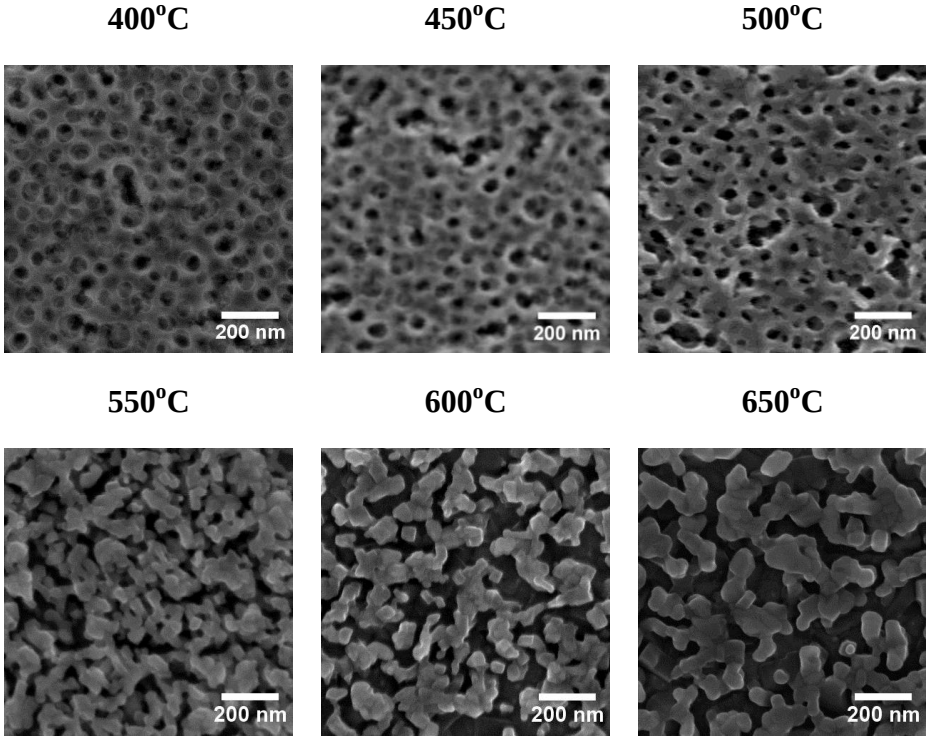

Figure 4.18 SEM micrographs of BFO porous P30 for different annealing temperatures, ranging from 400 to 650 ^{o}C for 5 min.

Figure 4.19, depicts the variation of the microstructure of sample P30 with the increase of the annealing time for 450 and 500 ^{o}C. At 450 ^{o}C there is no significant change concerning the porous order, as the annealing time increases. However, after 1 h of thermal treatment, break of symmetry in grain interfaces due to the presence of porosity results in random densification of the films.

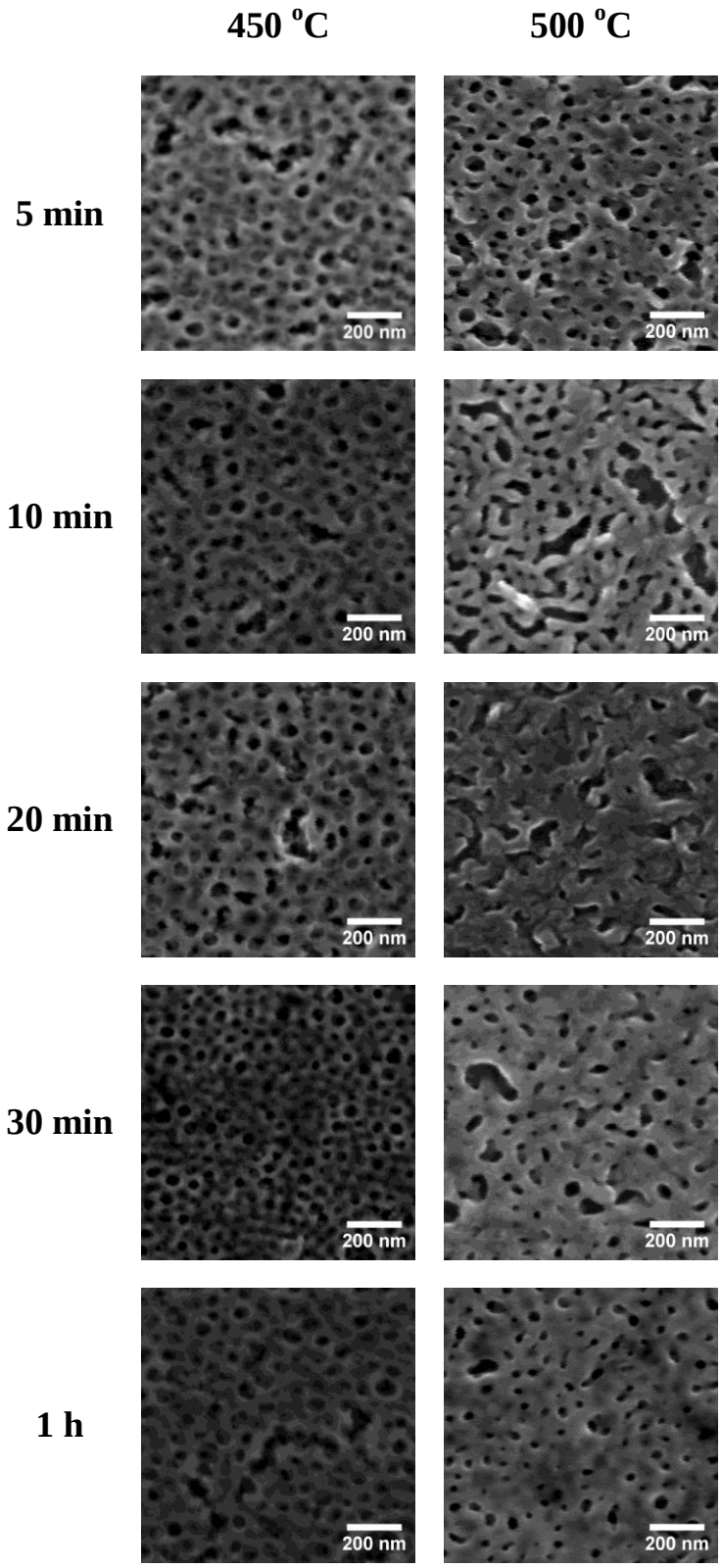

Figure 4.19 SEM micrographs of BFO porous P30 films annealed at 450 and 500 °C for increasing annealing times.

This effect becomes clear for the films annealed at 500 ^{o}C, where the ordered array gives rise to large gaps of matter, creating a labyrinth-like porous motif. As the annealing time increases the film densification takes place and the degree of porosity decreases, but the ordering of porosity is almost lost. As 500 ^{o}C is just before the transition temperature at which crystallization happens, as seen in **Figure 4.19**, higher annealing times present an extremely intense grain growth, thus these first steps of densification tend to diminish the size of pores.

PFM studies conducted in these samples show the lack of piezoresponse signal confirming the incipient degree of crystallinity of these films, since the crystallization occurs above 550 ^{o}C.

- **Raman Spectroscopy Results**

Raman spectroscopy studies were carried out to compliment the investigation and identification of the rhombohedral $BiFeO_3$ phase present in the films. **Figure 4.20** presents the Raman spectra of BFO porous P30 films annealed at 550, 600 and 650 ^{o}C for 5 min.

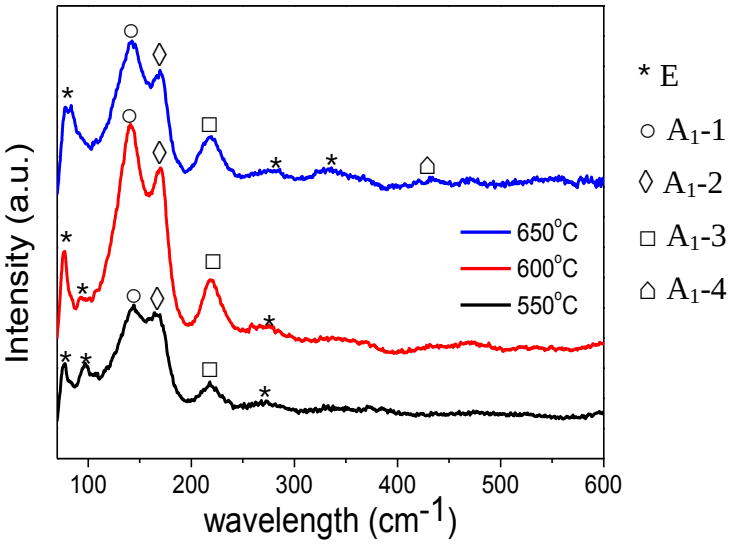

Figure 4.20 Raman spectra of BFO porous P30 films annealed at 550, 600 and 650 ^{o}C for 5min.

The allowed active phonon modes for the rhombohedral symmetry of BFO can be represented by: $\Gamma=4A_1+9E$, where 4 modes of A_1-symmetry and 9 degenerate modes of E-symmetry are predicted by group theory.[77] In the films under study, A_1-1, A_1-2 and A_1-3 modes present strong scattering intensity, while A_1-4 and all the E phonons are of weak and medium intensity respectively. In addition, peaks appearing at wavenumbers lower than 200 cm^{-1} result from Bi dislocations within the perovskite structure, whereas those with wavenumber above 200 cm^{-1} imply the tilting of the oxygen octahedra.[4,78] However, not all modes are always visible. Polarized Raman scattering studies by Fukumura *et al.*[79] and Kothari *et al.*[80], for single-crystal and polycrystalline bulk BFO respectively, revealed all 13 active modes, since phonon detection depends on polarization orientation. In our case horizontal polarization with backscattering geometry was used.

Porous BFO P30 films annealed at 650 ^oC present 6 of the phonon modes: A_1-1, A_1-2, A_1-3, A_1-4 and 4 E-symmetry modes (**Figure 4.20** and **Table 4.5**). For 600 ^oC annealing temperature only six active modes were detected. For 550 and 600 ^oC annealing temperatures the second E mode is present, whereas for 650 ^oC it disappears. However, the latter case shows the symmetry of A_1-4. Raman spectrum for 550 ^oC presents lower peak definition, possibly due to incipient crystallization. Although for the case of 600 ^oC more modes are present, the peak intensity is hindered, probably due to the appearance of other BFO symmetry phases.[37,81]

Table 4.5 presents all the detected phonon modes for BFO porous P30 films annealed at three different temperatures, together with the respective modes and its frequencies reported by Kothari *et al.*[80], Fukumura *et al.*[79], Singh *et al.*[77] and Yuan *et al.*[82], for comparison. The first group's studies were conducted for bulk polycrystalline BFO prepared via solid state reaction technique. The second group studied bulk single crystal BFO and the last two groups epitaxial thin films. These discrepancies between the obtained results may be related to the different nature of the films and the presence of residual secondary phases.

Table 4.5 Positions of the detected phonon modes (given in cm^{-1}) and their symmetries for BFO porous P30 films annealed at different temperatures. The respective modes as registered by four different studies are also presented for comparison.

Phonon Mode	**P30 550°C**	**P30 600°C**	**P30 650°C**	**Kothari *et al.*** [80]	**Fukumura *et al.*** [79]	**Sighn *et al.*** [77]	**Yuan *et al.*** [82]
E	75	76	77	71	77	-	-
E	94	90	-	98	136	-	-
A_1-1	140	140	140	135	147	136	153
A_1-2	160	167	165	167	176	168	178
A_1-3	215	216	212	218	227	211	224
E	267	271	271	255	265	275	270
E	-	-	324	322	375	-	-
A_1-4	-	-	426	430	490	425	-
E	-	-	-	598	525	587	618

- **PFM Studies**

In **Figure 4.21**, the topography and PFM images of BFO porous P30 films annealed at 600 °C for different scanning areas, 5 μm x 5 μm, 3 μm x 3 μm, 2 μm x 2 μm and 1 μm x 1 μm, are presented. A uniform ferroelectric domain distribution is observed for all images.

In order to ensure the genuine ferroelectric origin of the appearing domains, topography and PFM image correlation is required. The green contour in the case of 2 μm x 2 μm scanning area corresponds to a ferroelectric domain with upward polarization orientation, while the yellow one to a downward. The respective areas in the topography image are also highlighted, revealing topography uniformity for the specific area. Thus, in a highly homogeneous part of the film surface, ferroelectric domains with opposing orientations can be observed, which is a strong evidence for the claiming ferroelectric behaviour. These results also attest the crystallinity of the BFO porous films annealed at 600 °C.

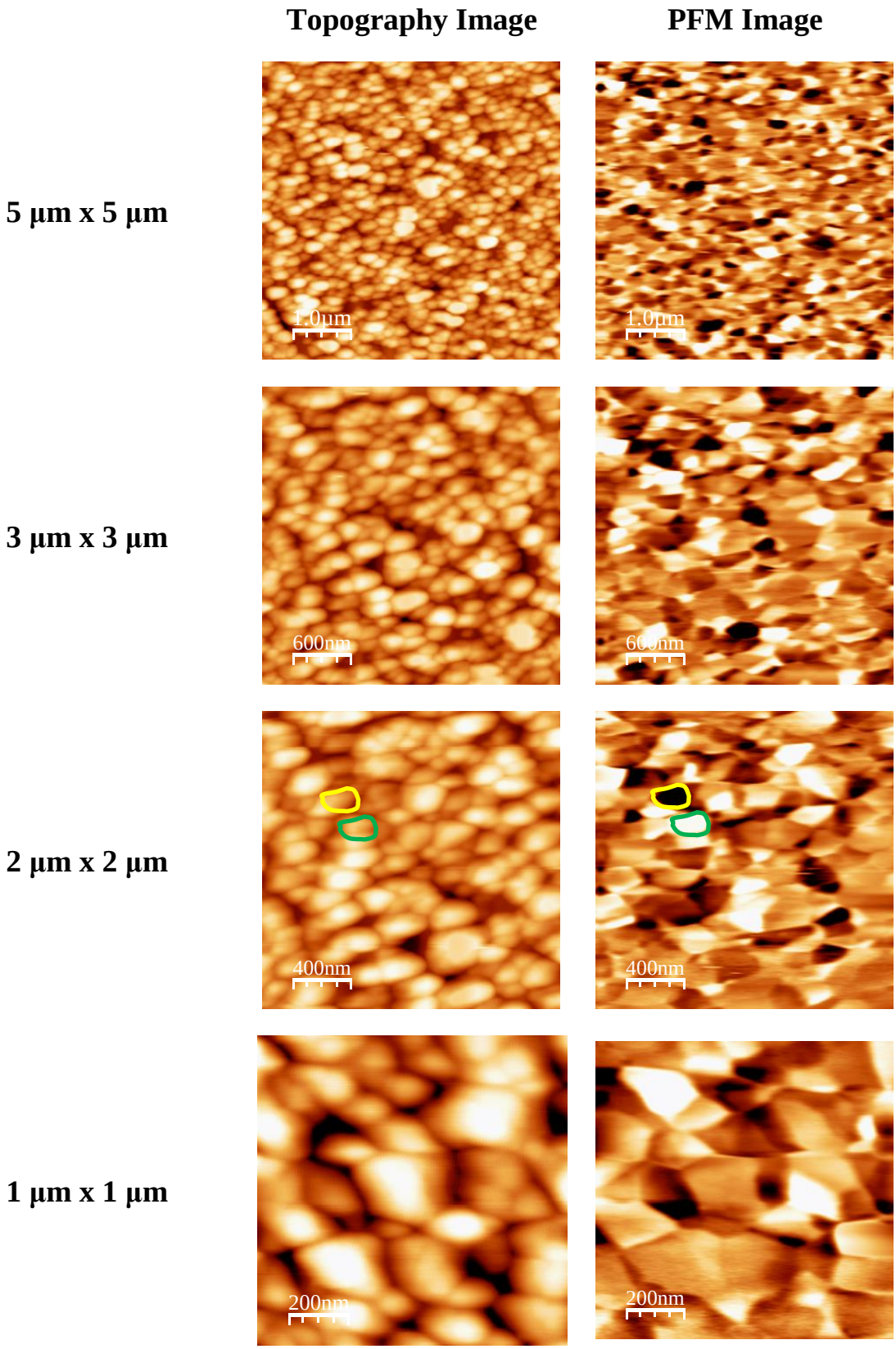

Figure 4.21 Topography and PFM images of BFO porous P30 films for different scanning areas.

4.2.3 Effect of Withdrawal Velocity on Multiferroic Properties

The solution with template mass of 24 mg was chosen for the withdrawal at different velocities, since it presented the best porous microstructure. In **Table 4.6**, the withdrawal velocities and the respective film thicknesses are presented.

Table 4.6 Dip-coating withdrawal velocities and respective film thickness for porous BFO films, annealed at 600 ^{o}C.

Sample Identification	Withdrawal Velocities (mm/min)	Thickness (nm)
P5	5.58	70 ± 12
P10	10.58	140 ± 10
P29	29.58	170 ± 9
P45	45.66	210 ± 11
P100	100	225 ±8
P150	150	240 ± 6
P180	180	280 ± 8

In **Table 4.12**, the SEM cross-section images for porous BFO P5, P10, P29, P45, P100, P150 and P180 films are shown. This task presented lots of difficulties, mainly due to peeling effect of the fragile film off the substrate surface. Images P29 and P150 were taken with perpendicular positioning of the sample. However the rest of the images were taken with an 8^{o} rotation angle of the sample holder, relatively to the perpendicular position required for the capture of cross-section image. The rotation was used in order to show the peeling effect, which makes difficult the focus on the significantly thin film. The inclination only causes a small divergence in the real film thickness, since cos (8^{o})≈0.99, which corresponds to a much smaller error comparing to the irregularity in the film thickness.

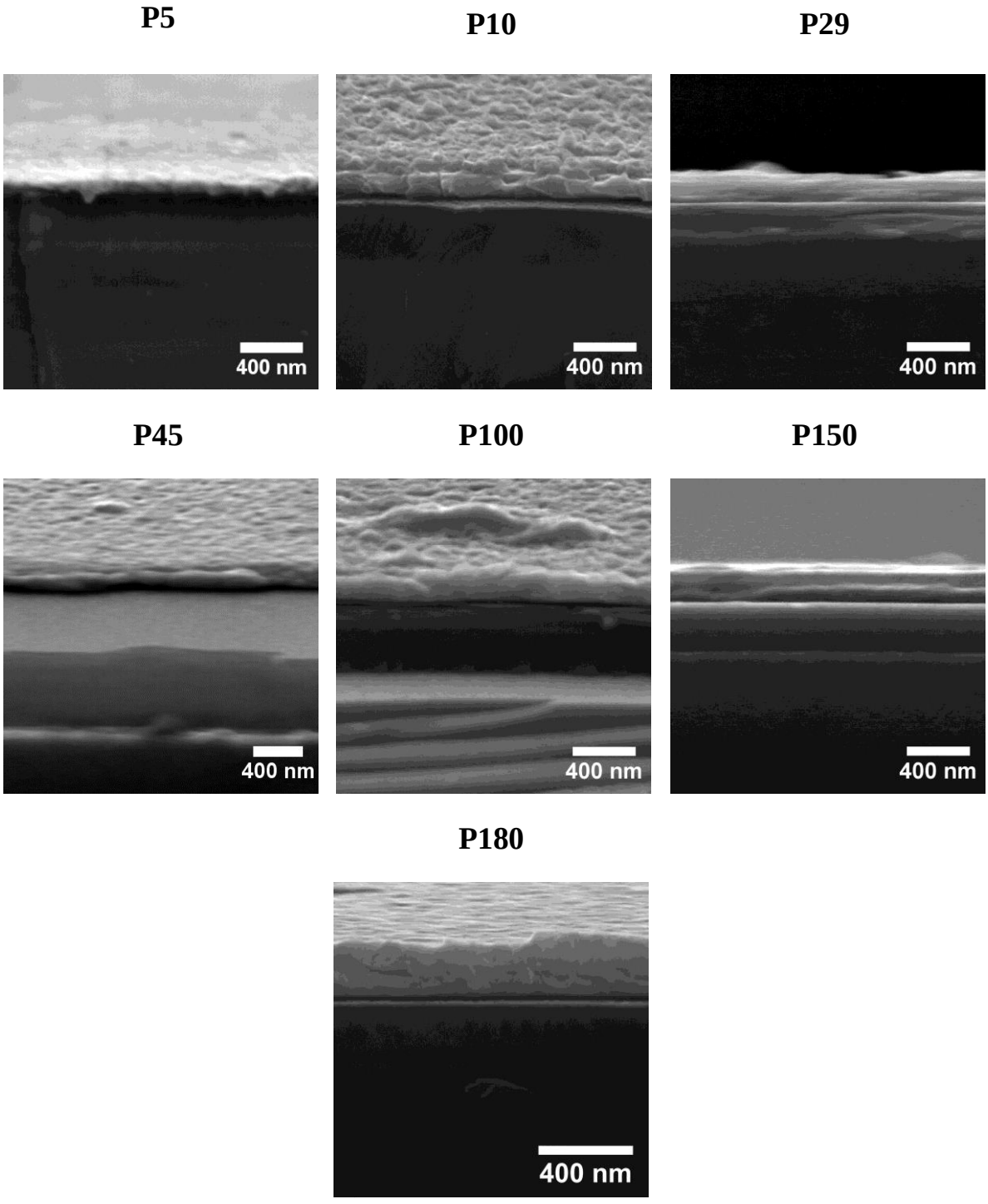

Figure 4.22 Cross-section SEM images of BFO porous P5, P10, P29, P45, P100, P150 and P180 films, annealed at 600 ^{o}C for 5 min. Increasing film thickness can be observed for increasing withdrawal velocity.

In **Figure 4.23**, the effect of the withdrawal velocity on the film thickness of the BFO porous films is presented. All samples show increase of thickness with increasing withdrawal velocity, confirming the right branch of the draining regime, as discussed in Section 2.6.2 and also observed for the dense films (Section 4.1.1).

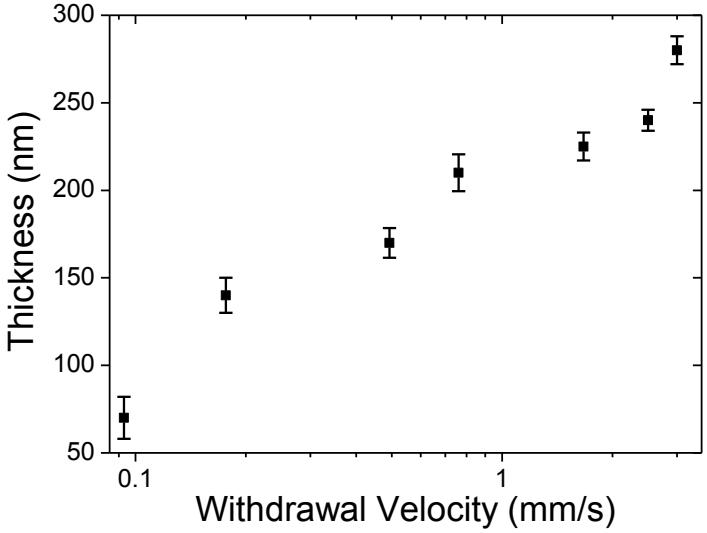

Figure 4.23 Withdrawal velocity effect on thickness for the porous thin films P5, P10, P29, P45, P100, P150 and P180, revealing increase of the film thickness with increasing withdrawal velocity.

- **XRD Results**

In **Figure 4.24**, the XRD patterns for BFO porous P5, P29, P45 and P150 films annealed at 600 ^{o}C are presented. Films P5 present less characteristic peaks of the $BiFeO_3$ rhombohedral phase, in combination with the occurrence of parasitic phases, close to 29, 38 and 44 2θ ^{o}. Comparing sample P5 with the respective dense D5 film (**Figure 4.4**, Section 4.1.2), one can observe the appearance of the same peaks, a fact that could lead to the conclusion that very low withdrawal velocities require a thorough investigation of the entire procedure, in order to achieve homogeneous, impurity-free thin films.

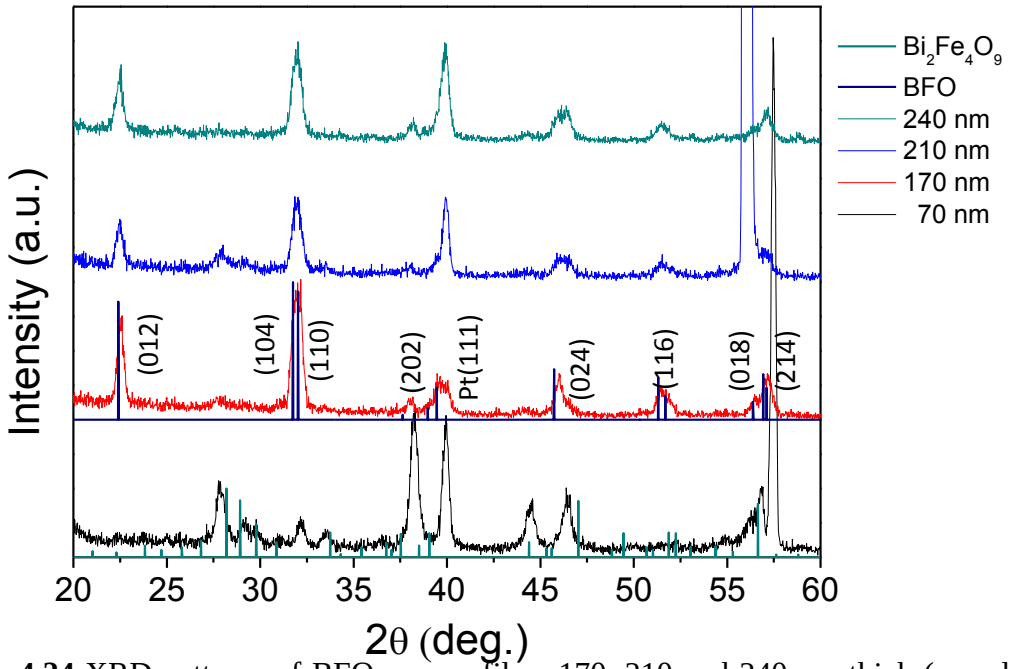

Figure 4.24 XRD patterns of BFO porous films 170, 210 and 240 nm thick (samples P5, P29, P45 and P150 respectively) annealed at 600^{o}C.

- **PFM Studies**

In **Figure 4.25**, the topography and PFM images for the BFO porous P29, P45, P150 and P180 films annealed at 600 ^{o}C are presented. The amplitude of the ac voltage applied and the frequency were the same as the other studies, 5 V and the 50 kHz respectively.

All PFM images show relatively high frequency of presence of ferroelectric domains, resembling extremely with the dense films presented in Section 4.1.3. Only the case of P5 films shows large non-polarized regions, mainly due to the presence of BFO impurities, as well as surface or thickness irregularities, a fact that also provoked deformation in the topography image. It should be mentioned that there were some regions, especially for the thinner films, where the PFM signal was much weaker. In addition, zones with larger grains or inhomogeneous distribution of grains performed enhanced piezoelectric response, often surrounded by regions with zero induced polarization, as seen in PFM images of films P5 and P29.

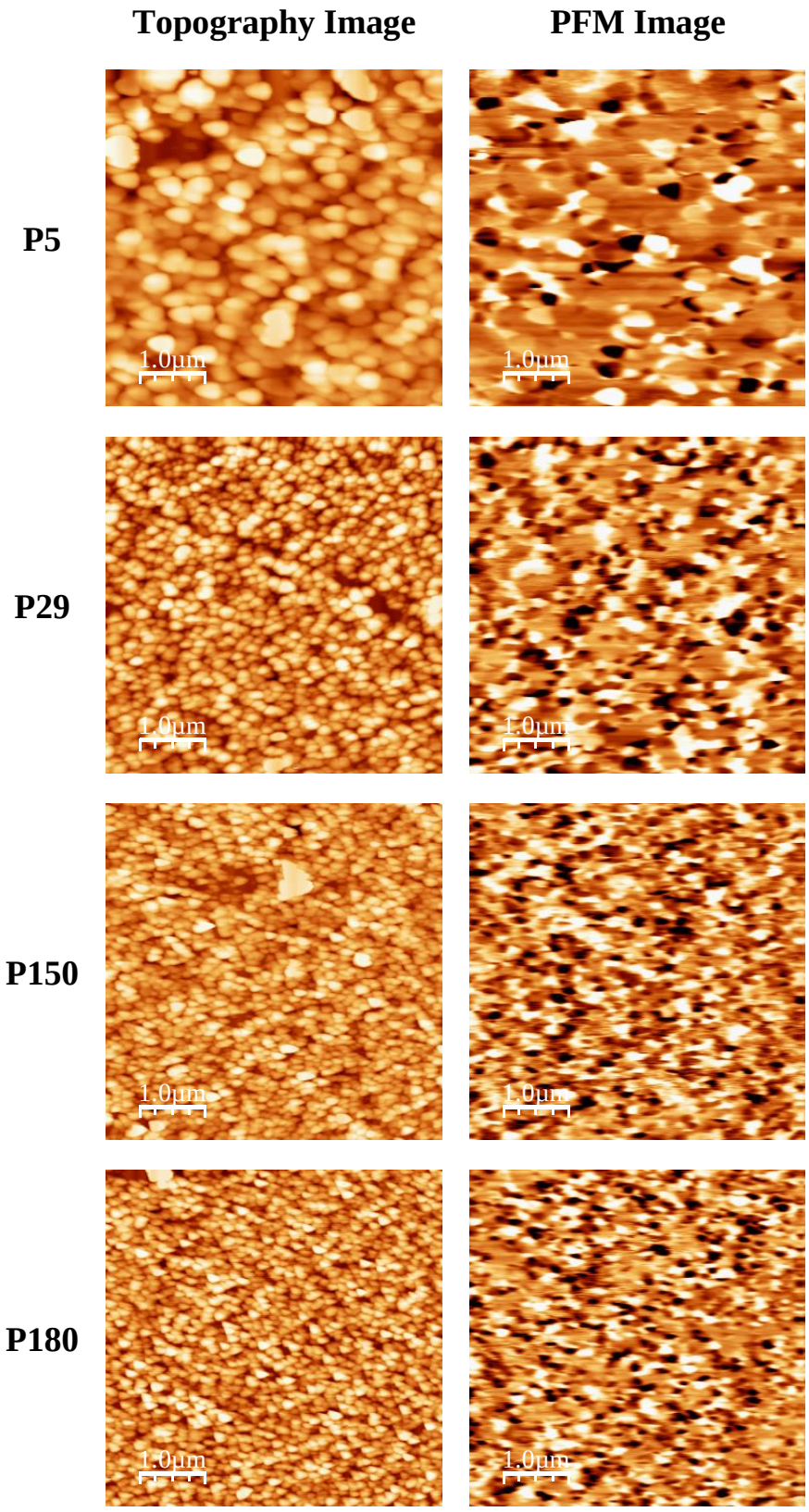

Figure 4.25 Topography and PFM images for 5 μm x 5 μm scanning area of BFO porous P5, P29, P150 and P180 films with different thickness.

In **Figure 4.26**, the local piezoelectric hysteresis loop measurements for BFO porous P5, P29 and P150 films annealed at 600 ^{o}C are presented, indicating increase of saturation polarization with increasing withdrawal velocity, as it was also observed for the BFO dense films (Section 4.1.3). It should be mentioned that the porous films P5 presented impurities, which also accounts for such low piezoresponse.

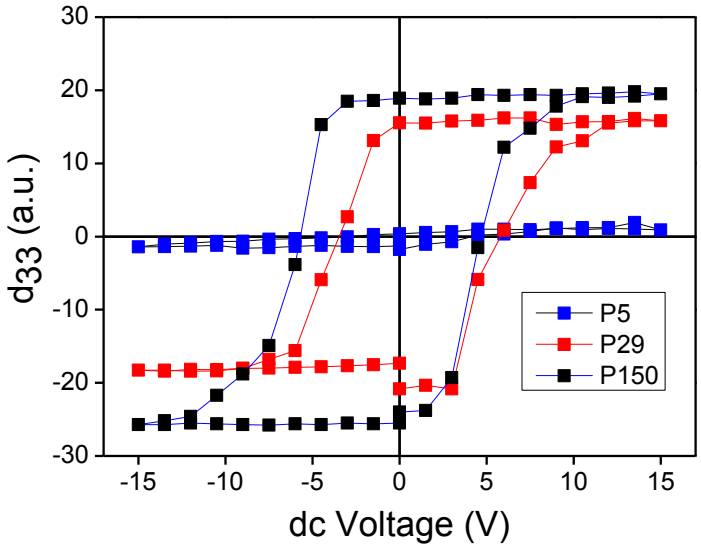

Figure 4.26 Local polarization hysteresis loops for BFO porous P5, P29 and P150 films, annealed at 600 ^{o}C. Increasing thickness resulted in increase of the piezoelectric coefficient.

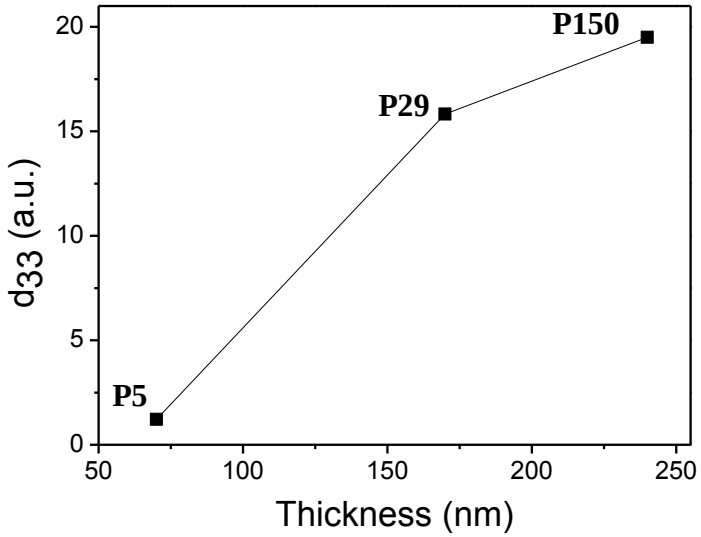

Figure 4.27 Piezoelectric coefficient d_{33} as a function of the BFO porous film thickness.

- **Magnetic Characterization Results**

Table 4.7 summarises the magnetic response measurements for the BFO porous P5, P29 and P150 films, together with the relevant thicknesses. The respective porosity surface for the total volume for each sample was calculated. The pores were considered as spheres, with the respective diameter, as measured by the SEM micrographs presented in **Figure 4.28**. An approximation of the total surface area of the porous network was made by calculating the pore density of the surface and admitting that the same distribution takes place for the entire film volume. As expected, increase of the total porosity surface is observed for increasing thickness. The pore sizes and the surface pore density of the films do not present large deviation. Larger volume due to higher thickness for P150 films results in higher than the double of the porosity area of P5 films.

Table 4.7 Antiferromangnetic susceptibility, remanent magnetization and the respective thicknesses and porosity surface for BFO porous P5, P29 and P150 films, annealed at 600 ^{o}C.

Sample Identification	**Thickness (nm)**	**Pore Size (nm)**	**Porosity Surface Area (cm^2)**	**χ_{AF} (10^{-10} emu/Oe)**	**μ_r (10^{-5} emu)**
P5	70 ± 12	37 ± 1.9	0.28 ± 0.01	3.89 ± 0.2	3.44 ± 1.5
P29	170 ± 9	38 ± 3.5	0.52 ± 0.008	4.27 ±0.2	6.13 ± 1.5
P150	240 ± 6	39 ± 3.6	0.66 ± 0.007	7.03 ± 0.2	17.3 ± 1.5

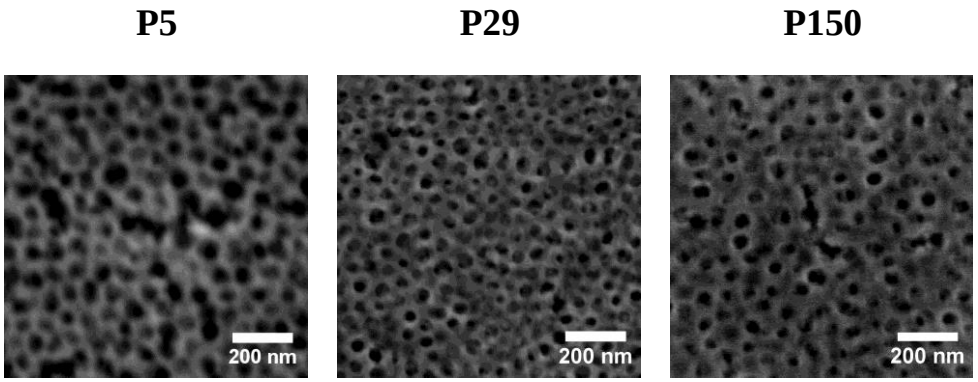

Figure 4.28 SEM micrographs of BFO porous P5, P29 and P150 films.

As shown in **Figure 4.29**, the magnetization curves reveal increase of magnetization saturation for increasing thickness (**Figure 4.30** (a)). This outcome is explained by the increase of the porosity surface (**Table 4.7** and **Figure 4.30**(b)), induced be the increased porous network for the cases of thicker films. Since no normalization by mass of film was made, in a sense that a more relative value of magnetization would have been measured if such a subtraction had been made, thicker films presented higher absolute magnetization than the thinner ones. BFO porous P150 films with a thickness of 240 nm present a porous network of 1.99 cm^2 total area, which is 330992 times larger than the surface area of a dense sample with the same dimensions and as discussed in Section 4.2.1 it presents higher magnetic response.

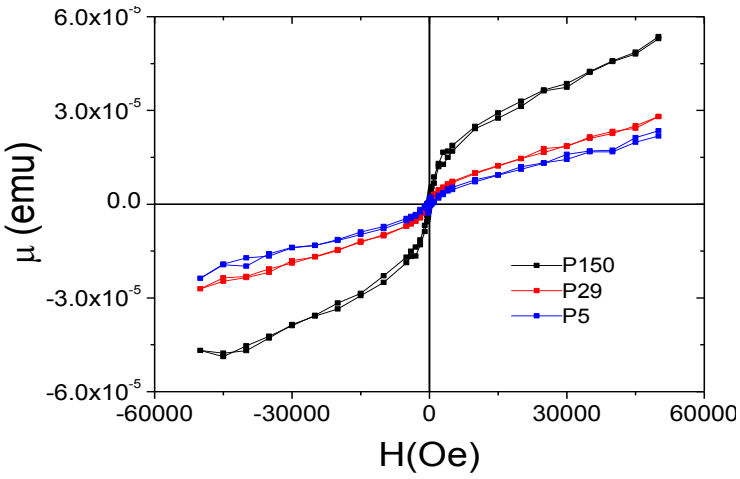

Figure 4.29 Magnetic moment measurements under varying magnetic field at 300K for porous samples with increasing thickness P5, P29 and P150, annealed at 600°C.

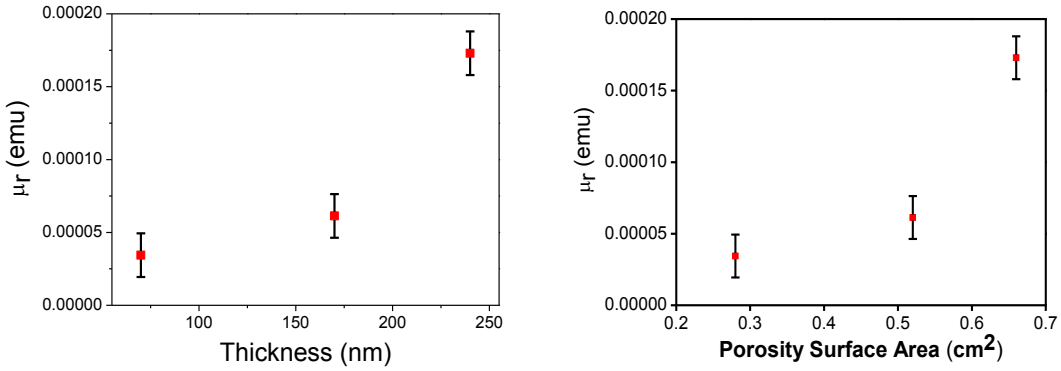

(a) (b)

Figure 4.30 Remanent magnetization as a function of (a) thickness and (b) porosity surface for porous samples with increasing thickness P5, P29 and P150.

Summarising for the thickness and porosity study of the porous films, increase in the withdrawal velocity led to increase in the film thickness. The high surface area present in the porous films results in increase in the remanent magnetization, due to the uncompensated magnetic moments occurring at cases with surface anisotropies and elevated roughness.

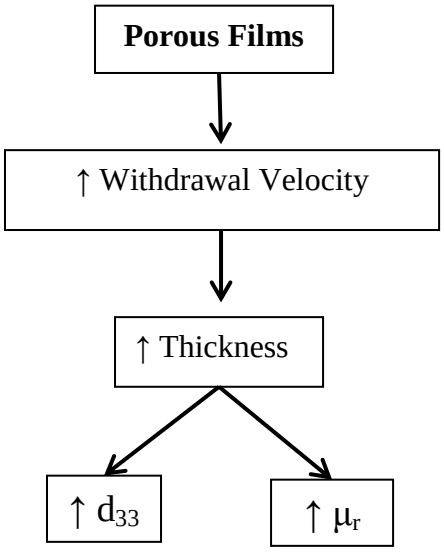

Figure 4.31 Schematic representation of the withdrawal velocity effect on thickness and multiferroic properties for the series of porous films.

4.2.4 Effect of Sol-gel Concentration on Microstructure and FerroelectricProperties

The observation of loss of porosity order with increasing annealing temperature (Section 4.2.2) led to a sol-gel concentration increase study. Crystallization process resulted in large gaps between the BFO grains, with a random arrangement. A well-ordered porous network is essential, principally for the possible functionalization procedure and the obtainment of properties which are not subjected to irregular conditions. In addition, the investigation of inhomogeneous samples is always much more elaborate, requiring more accurate characterization techniques and more complicated theoretic background.

- **XRD Results**

The XRD patterns for BFO porous P0.3, P0.4 and P0.5 films with solution concentrations of 0.3 M, 0.4 M and 0.5 M respectively annealed at 600 ^{o}C are presented in **Figure 4.32**. All the samples present the characteristic peaks of the rhombohedral phase of BFO, with a slight difference in the intensity of the peaks. The peak close to 28 2θ ^{o} for the films P0.4 is probably due to the presence of $Bi_2Fe_4O_9$.

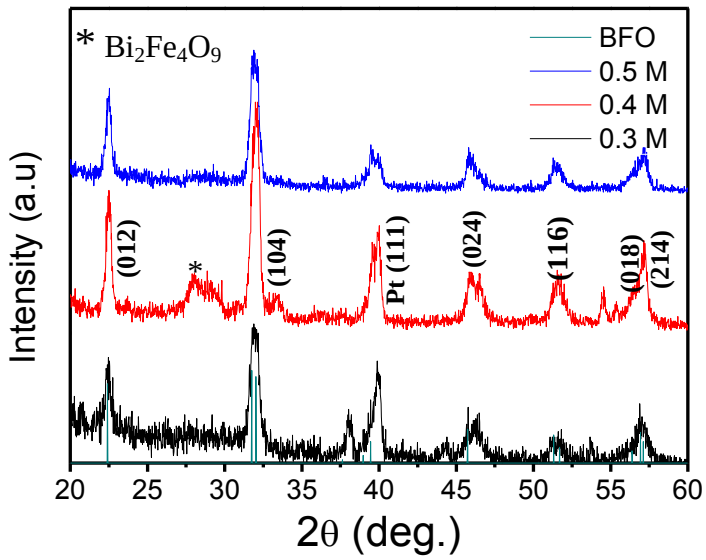

Figure 4.32 XRD patterns for BFO porous P0.3, P0.4 and P0.5 films annealed ta 600 ^{o}C.

In **Figure 4.33**, the SEM micrographs for BFO porous P0.3, P0.4 and P0.5 films are presented, with 0.3 M, 0.4 M and 0.5 M solution concentrations respectively and annealed at 400 and 600^{o}C. The solution template mass was chosen to be 30 mg. Although the case of 24 mg template mass showed better results, it was avoided for the current study, since it corresponded to the lowest template quantity and could have provoked more extreme changes. The withdrawal velocity for all the samples was at 29.58 mm/min. The samples were annealed at 400 ^{o}C for 5 min and subsequently at 600 ^{o}C, also with 5 min duration.

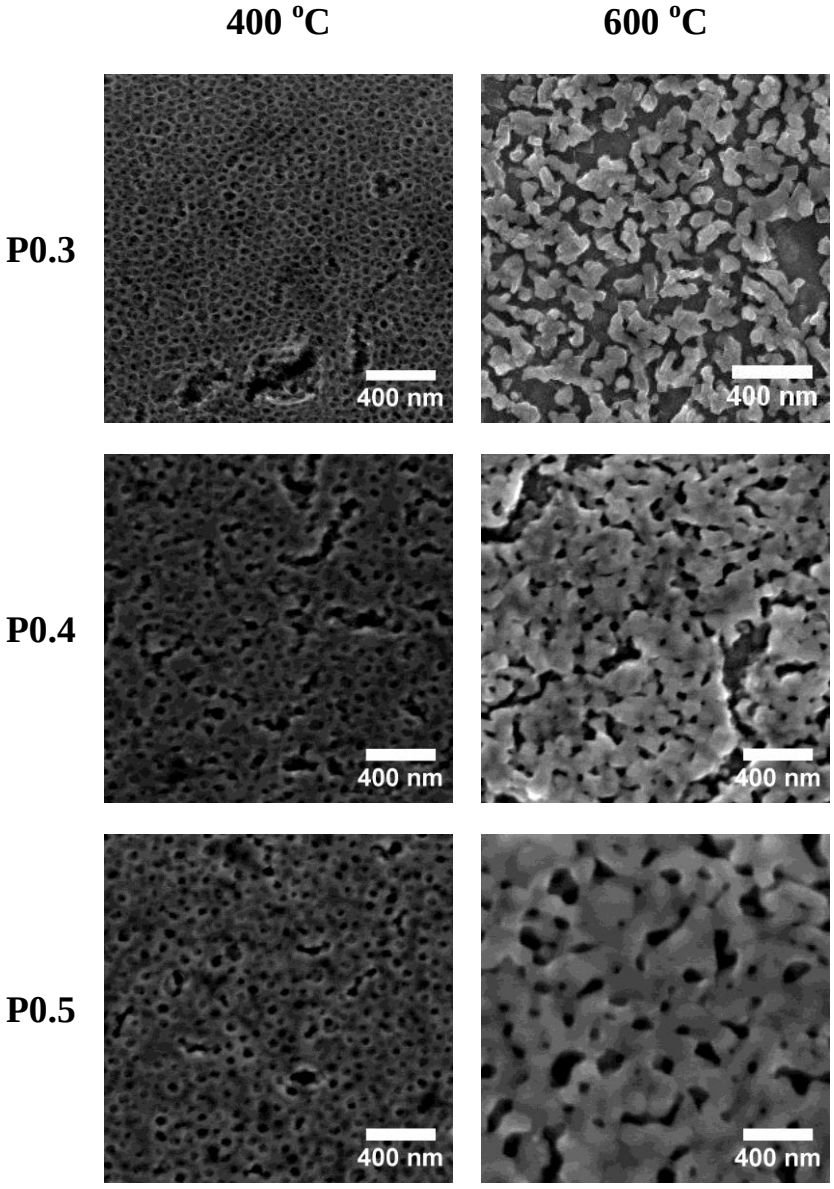

Figure 4.33 SEM micrographs for BFO porous P0.3, P0.4 and P0.5 films, annealed at 400 ^{o}C and 600 ^{o}C. Films P0.5 present a more dense structure with enhanced porosity order.

Increase of the inorganic precursor concentration led to the formation of more dense microstructure, decreasing substantially the gap generation observed in the porous P0.3 films, as discussed in Section 4.2.2. Sample P0.5 at 600 ^{o}C shows a porous structure with an increase in the average pore size from 40 to 44 nm, yet with a high degree of deviation. Further annealing temperature studies should be carried out, in order to explore the effect of different annealing profiles on the porous structure.

- **PFM Studies**

In **Figure 4.34**, the topography and PFM images for BFO porous P0.3, P0.4 and P0.5 films are presented. All films present a similar domain configuration. However, for films P0.4 and P0.5 there is a slight grain deformation in the topography image.

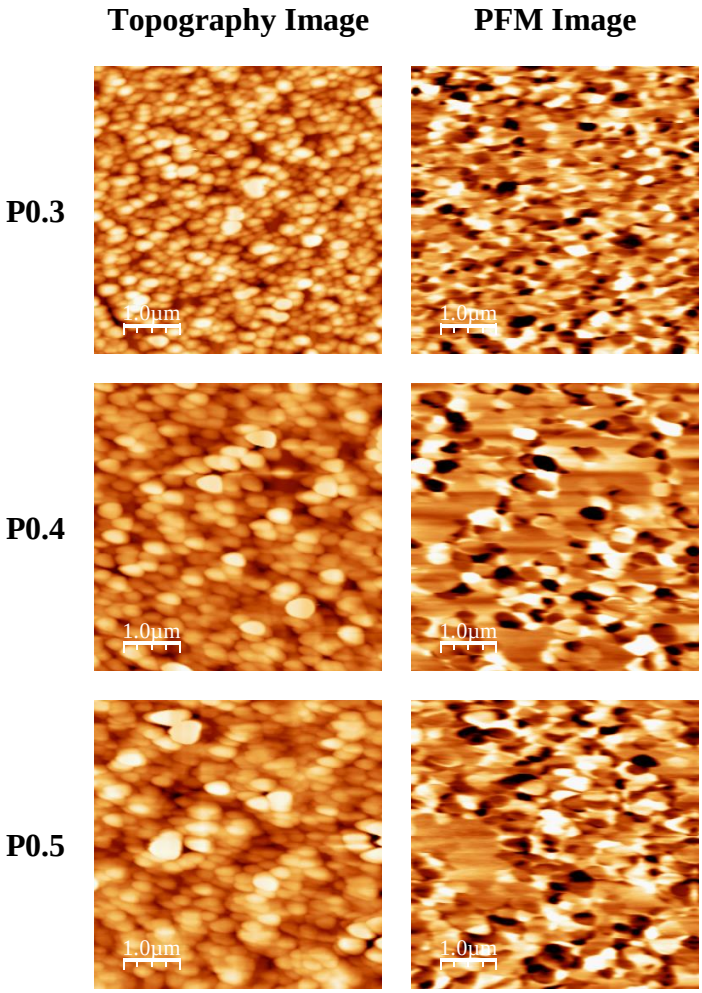

Figure 4.34 Topography and PFM images for porous P0.3, P0.4 and P0.5 films, annealed at 600 ^{o}C.

The local polarization hysteresis loops for the porous films with increasing sol-gel concentration P0.3, P0.4 and P0.5 are presented in **Figure 4.35** (a). A clear increase in the saturation polarization can be observed with increasing inorganic precursor quantity in the solution. This result is extremely important, since by increasing the solution concentration a more controlled order of the porous structure can be obtained with a simultaneous increase in the piezoresponse.

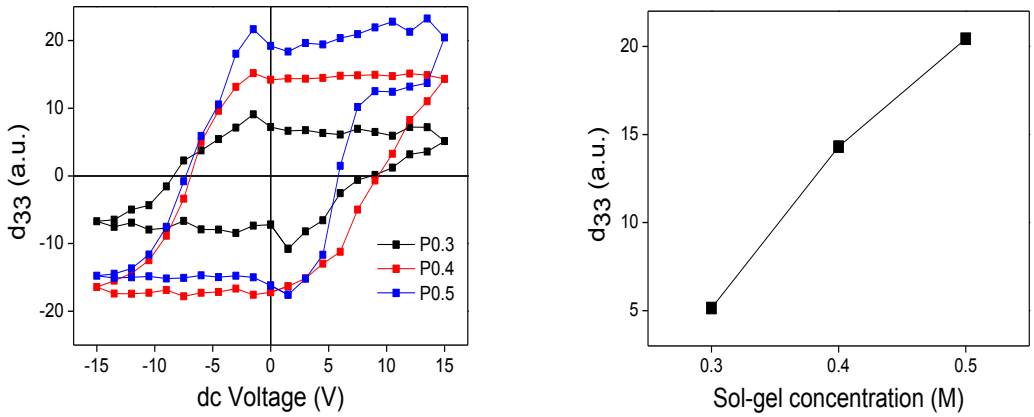

Figure 4.35 (a) Local polarization hysteresis loops of BFO porous P0.3, P0.4 and P0.5 films with increasing sol-gel concentration and annealed at 600 ^{o}C. (b) Piezoelectric coefficient as a function of sol-gel concentration, revealing increase of piezoresponse with increasing sol-gel concentration.

Summarising for the study of sol-gel concentration in the porous films, enhanced porous distribution and structure was achieved, in combination with an increase in the piezoelectric coefficient d_{33}.

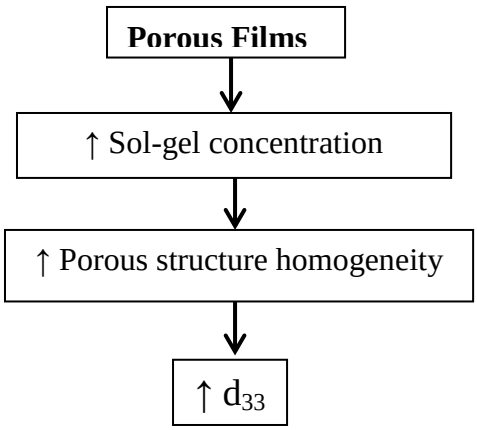

Figure 4.36 Schematic representation of the sol-gel concentration effect on porous structure and ferroelectric properties for the series of porous films.

4.2.5 Magnetic Force Microscopy Studies

The weak ferromagnetic behaviour of BFO difficilitates the magnetic domain visualization via Magnetic force Microscopy (MFM), No report of such characterization has been made before, apart from the case of composites, primarily a combination of the ferroelectric-antiferromagnetic BFO with ferromagnetic materials. By the application of an external electric field, magnetoelectric coupling takes place, mainly at the interface of the two phases, which makes possible the emergence of magnetic domains.[32,74]

In order to explore whether electric field-induced magnetization could occur, MFM studies were carried out for BFO D180 and P24 films annealed at 600 ^{o}C, with simultaneous application of dc voltage of 4 V. As mentioned in Section 2.7.3, a combination of tapping and non-contact mode is required for such measurements. The topography image is first taken by tapping mode, which is a hybrid type of topography imaging, a combination between contact and non-contact mode. The cantilever-tip vibrates at the resonance frequency and the amplitude is maintained constant during surface-tip interaction, causing vertical variations and making possible the surface monitoring. However, for the magnetic force detection the tip is elevated at sufficient distance from the surface (non-contact lifting mode operation), depending on the roughness of the sample. For the current study, non-contact measurements took place at 200 nm.

In **Figure 4.37**, the topography and MFM images are shown for a dense sample deposited at 180mm/min (D180) and a porous sample with 24 mg of solution template mass and 29.58 mm/min withdrawal velocity (P24). The last image is a tapping mode topography image of sample P24, without the use of magnetic detection mode. The tip elevation, required for the latter measurement, in most cases results in large drifts in the topography image, as can be observed in the second topography image. It was chosen in order to show the high resolution of tapping mode for surface imaging, comparing to the contact mode of PFM technique.

In the MFM images domains with opposing orientation were detected. The 200 nm tip distance of the surface excludes the case of topography artefacts. However, most probably the domains' nature is ferroelectric, since the conductive tip can sense the attractive electrostatic forces from the electric field induced surface charges. In addition, the domain geometry is very similar to the ones obtained by PFM characterization. In order

to ensure the origin of the identified response in the MFM images, a tapping mode cantilever-tip without the magnetic coating was subsequently used. The results showed resembling domain configuration, however are not presented here, as scanning of the same area is extremely difficult to be achieved when changing the tip. Last but not least, a possible magnetoelectric coupling, presumably occurring at the domain walls and grain boundaries, resulted in domains slightly larger than the ferroelectric ones.

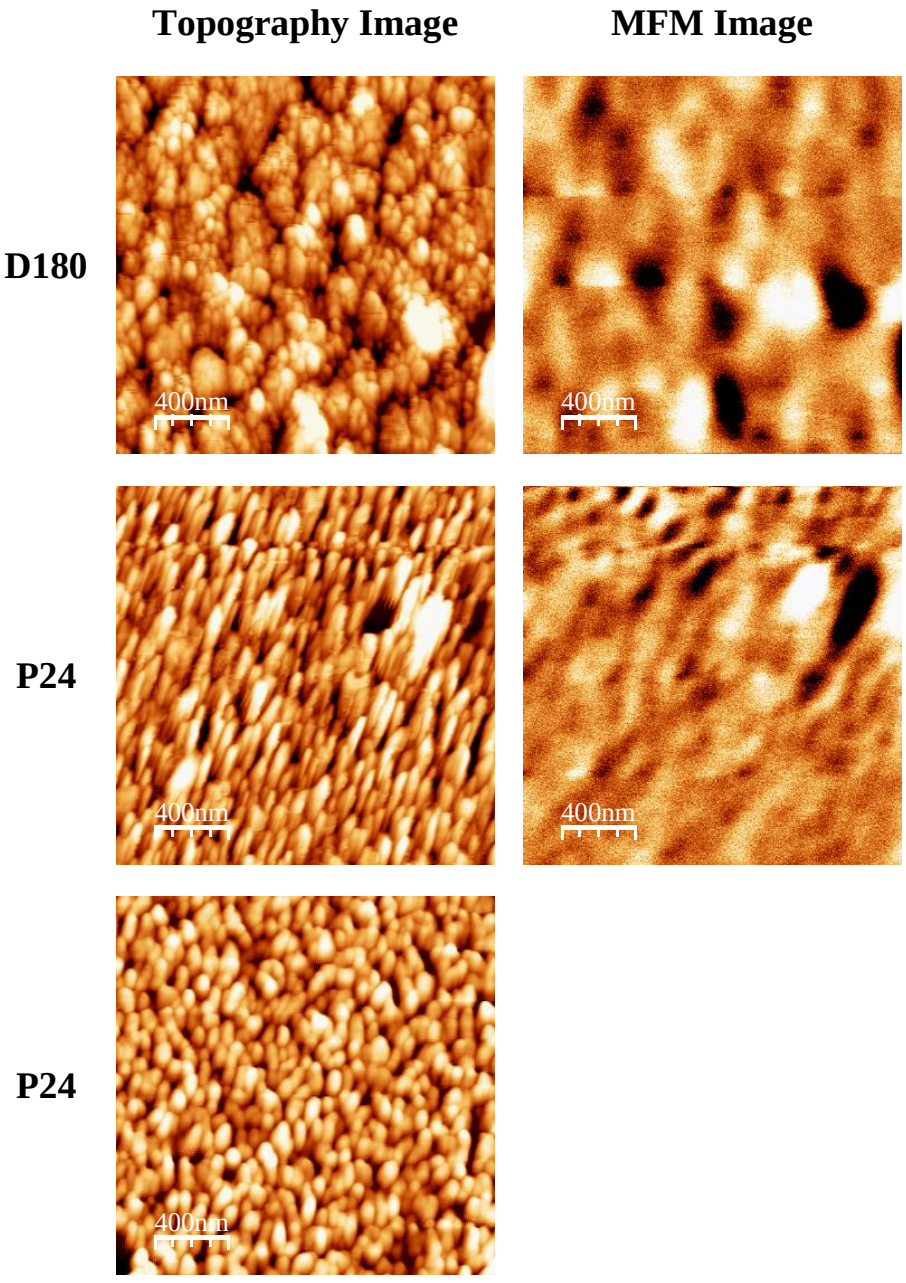

Figure 4.37 Topography and MFM images for samples D180 and P24. The last topography image was taken by the use of tapping mode, without the interleave mode required for the MFM imaging.

CHAPTER 5

Conclusions and Future Work

5. Conclusions and Future Work

A series of BFO dense films with varying withdrawal velocities were produced, serving as means of comparison for the porous thin films. For low withdrawal velocities the films presented porosity features, yet by increasing velocity dense structure was obtained. Increasing withdrawal velocity resulted in increasing film thickness. Phase impurities were detected for the dense films D5 with the lowest film thickness. Piezoresponse Force Microscopy (PFM) characterization was conducted, revealing the expected ferroelectric domains. By the same technique, local piezoelectric hysteresis loops were obtained, showing increase of polarization saturation with increasing film thickness. Lastly, magnetic moment measurements were carried out by the use of Superconducting Quantum Interference Device (SQUID), presenting decrease of remanent magnetization with increasing thickness. A schematic representation in **Figure 5.1** summarises the above results.

Nevertheless, further studies for the obtainment of higher film densification should be made, so that a more correct comparison with the porous case could be carried out. Finally, after conferring a dense structure, macroscopic measurements of the piezoelectric hysteresis loop should be done, in order to be compared with the local ones.

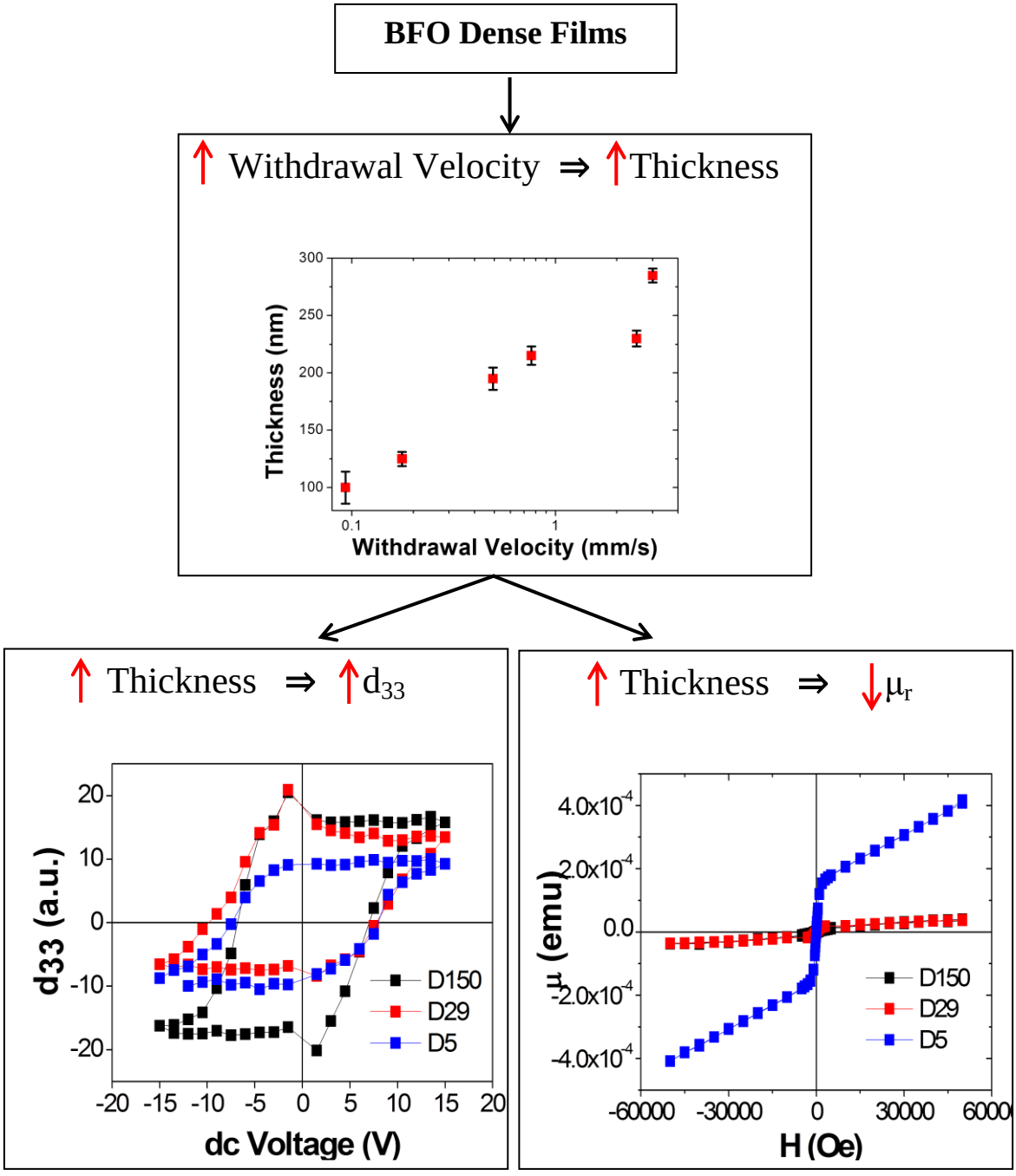

Figure 5.1 Schematic representation of the results obtained in this work for the sol-gel prepared BFO dense films. Increasing withdrawal velocity led to increasing film thickness, which resulted in the increase of the piezoelectric coefficient and decrease of the remanent magnetization.

A porous network in $BiFeO_3$ thin films was introduced by using a polymeric template. By varying the template concentration, the size and ordering of porosity was tailored. Homogeneity and lack of cracks in the films were successfully achieved, by decreasing solution template mass, for a given solution concentration. Thermal treatment studies revealed loss of porous network ordering at elevated annealing temperatures, required for the obtainment of crystallization and enhanced multiferroic properties. BFO porous films with low film thickness presented the formation of impurities. Increasing dip-coating withdrawal velocity led to the production of films with increasing thicknesses. Local piezoelectric hysteresis loops showed increase of the effective piezoelectric coefficient with increasing thickness. SQUID characterization presented increasing remanent magnetization with increasing porosity.

The most important future study for the porous matrices is that of the microstructure regulation at elevated annealing temperatures. This could be faced by better control of the correlation of the quantities of the inorganic precursors and the template in the solution, as well as by the use of different solvents. In addition, a series of annealing profiles should be studied, such as nitrogen atmosphere and slower and longer thermal treatment processes.

At last but not least, the functionalization of the porous matrices by the introduction of preferably a ferromagnetic material, could lead to enhanced multiferroic properties and gigantic magnetoelectric coupling. Anyhow, that is the main purpose for the investigation of such intelligent architectures.

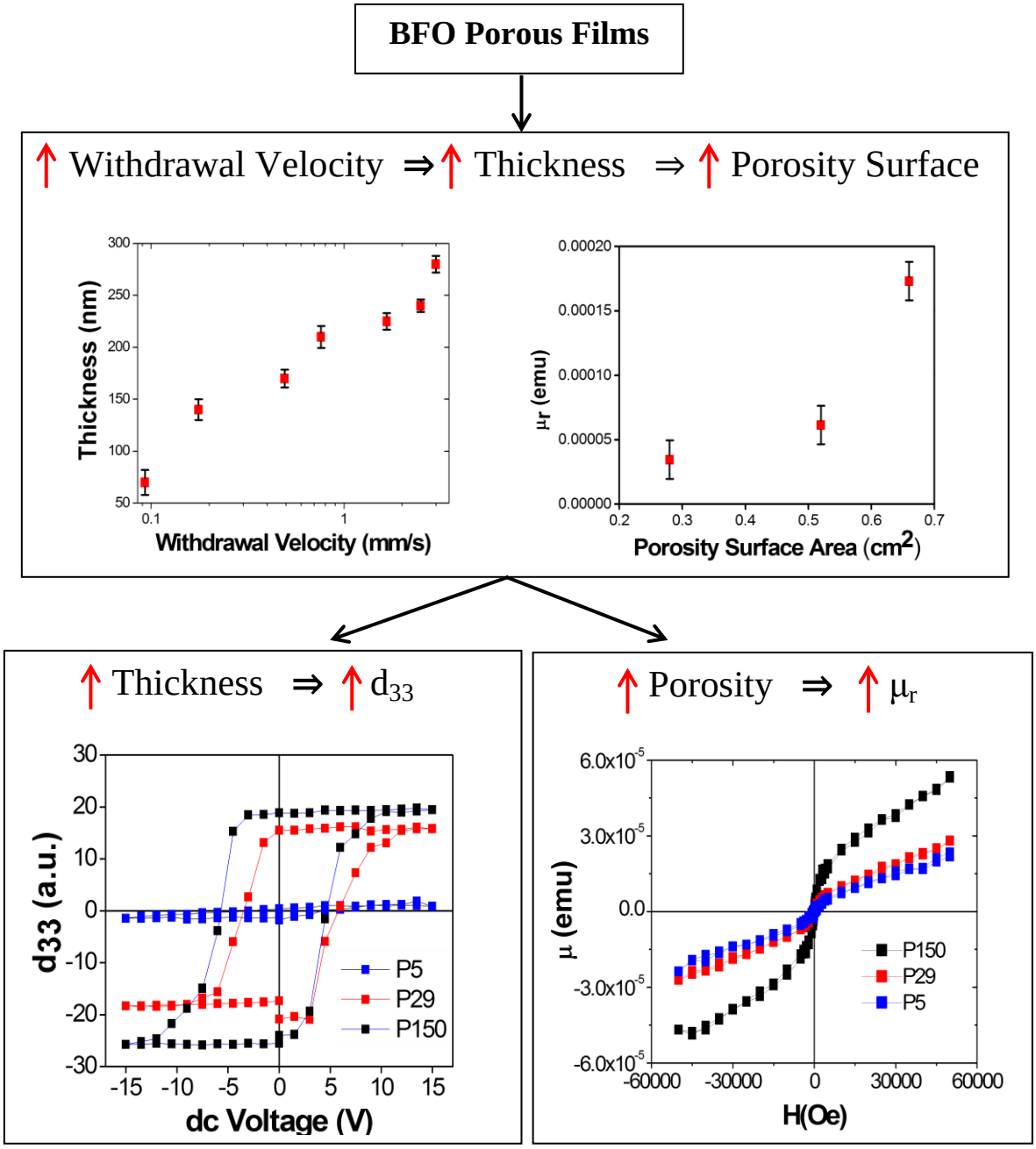

Figure 5.2 Schematic representation of the results obtained in this work sol-gel prepared BFO films. Increasing withdrawal velocity led to increase in the thickness and the porosity surface area, which resulted in increasing piezoelectric coefficient and remanent magnetization.

References

References

[1] G. Suyal, N. Setter, *Journal of the European Ceramic Society* **2004**, *24*, 247.

[2] V. Stancu, M. Lisca, I. Boerasu, L. Pintilie, M. Kosec, *Thin Solid Films* **2007**, *515*, 6557.

[3] J. Nogués, I. K. Schuller, *Journal of Magnetism and Magnetic Materials* **1999**, *192*, 203.

[4] Q. Xu, X. Zheng, Y. Yang, D. Wu, M. Xu, *Solid State Communications* **2011**, *151*, 624.

[5] http://www.pocketables.com/2011/08/whats-the-next-step-in-the-evolution-of-the-computer.html, **2013**.

[6] G. E. Moore, *Proceedings of the IEEE* **1998**, *86*, 82.

[7] "International Technology Roadmap for Semiconductors," can be found under http://www.itrs.net/, **2012**.

[8] Y. Wang, J. M. Hu, Y. H. Lin, C. W. Nan, *NPG Asia Materials* **2010**, *2*, 61.

[9] L. W. Martin, R. Ramesh, *Acta Materialia* **2012**, *60*, 2449.

[10] W. Eerenstein, N. D. Mathur, J. F. Scott, *Nature* **2006**, *442*, 759.

[11] N. A. Spaldin, S. W. Cheong, R. Ramesh, *Physics Today* **2010**, *63*, 38.

[12] J.-M. HU, J. MA, J. WANG, Z. LI, Y.-H. LIN, C. W. NAN, *Journal of Advanced Dielectrics* **2011**, *01*, 1.

[13] J. F. Scott, in *Ferro- and Antiferroelectricity: Order/Disorder Versus Displacive* (Eds.: N.S. Dalal, A. BussmannHolder), Springer-Verlag Berlin, Berlin, **2007**, p. 199.

[14] Kleemann W., *American Physical Society* **2009**, *2*, 105.

[15] M. Pizzol, M. Thomsen, M. S. Andersen, *Science of The Total Environment* **2010**, *408*, 5478.

[16] H. Black, *Environmental Health Perspectives* **2005**, *113*.

[17] K. M. Rabe, C. H. Ahn, J. M. Triscone, *Physics of Ferroelectrics: A Modern Perspective*, Springer, Berlin, Heidelberg, New York, **2007**.

[18] D. Damjanovic, *Reports on Progress in Physics* **1998**, *61*, 1267.

[19] S. M. Yang, J. G. Yoon, T. W. Noh, *Current Applied Physics* **2011**, *11*, 1111.

[20] A. Gruverman, S. V Kalinin, *Journal of Materials Science* **2006**, *41*, 107.

[21] S. V. Kalinin, A. N. Morozovska, L. Q. Chen, B. J. Rodriguez, *Repoprts on Progress in Physics* **2010**, *73*, 67.

[22] S. Jesse, H. N. Lee, S. V Kalinin, *Review of Scientific Instruments* **2006**, *77*.

[23] C. J. Howard, H. T. Stokes, *Acta Crystallographica: Section A (Wiley-Blackwell)* **2005**, *61*, 93.

[24] J. William D. Callister, *Materials Science and Engineering: An Introduction*, John Wiley & Sons, Inc., New York, **2007**.

[25] N. A. Spaldin, *Magnetic Materials: Fundamentals and Applications*, Cambridge University Press, United States of America, **2003**.

[26] C. Liu, F. Yun, H. Morkoc, *Journal of Materials Science-Materials in Electronics* **2005**, *16*, 555.

[27] K. F. Wang, J. M. Liu, Z. F. Ren, *Advances in Physics* **2009**, *58*, 321.

[28] M. Fiebig, *Journal of Physics D: Applied Physics* **2005**, *38*, R123.

[29] J. Wang, J. B. Neaton, H. Zheng, V. Nagarajan, S. B. Ogale, B. Liu, D. Viehland, V. Vaithyanathan, D. G. Schlom, U. V Waghmare, N. A. Spaldin, K. M. Rabe, M. Wuttig, R. Ramesh, *Science* **2003**, *299*, 1719.

[30] H. Zheng, J. Wang, L. Mohaddes-Ardabili, M. Wuttig, L. Salamanca-Riba, D. G. Schlom, R. Ramesh, *Applied Physics Letters* **2004**, *85*, 2035.

[31] H. Zheng, J. Wang, S. E. Lofland, Z. Ma, L. Mohaddes-Ardabili, T. Zhao, L. Salamanca-Riba, S. R. Shinde, S. B. Ogale, F. Bai, D. Viehland, Y. Jia, D. G. Schlom, M. Wuttig, A. Roytburd, R. Ramesh, *Science* **2004**, *303*, 661.

[32] F. Zavaliche, H. Zheng, L. Mohaddes-Ardabili, S. Y. Yang, Q. Zhan, P. Shafer, E. Reilly, R. Chopdekar, Y. Jia, P. Wright, D. G. Schlom, Y. Suzuki, R. Ramesh, *Nano Letters* **2005**, *5*, 1793.

[33] H. Zheng, Q. Zhan, F. Zavaliche, M. Sherburne, F. Straub, M. P. Cruz, L.-Q. Chen, U. Dahmen, R. Ramesh, *Nano Letters* **2006**, *6*, 1401.

[34] L. Yan, Z. Wang, Z. Xing, J. Li, D. Viehland, *Journal of Applied Physics* **2010**, *107*, 64105.

[35] R. Jahns, A. Piorra, C. Kirchhof, D. Meyners, J. L. Gugat, M. Krantz, M. Gerken, R. Knochel, E. Quandt, *Journal of the American Ceramic Society* **n.d.**, 1.

[36] M. Valant, A. K. Axelsson, N. Alford, *Chemistry of Materials* **2007**, *19*, 5431.

[37] G. Catalan, J. F. Scott, *Advanced Materials* **2009**, *21*, 2463.

[38] R. Safi, H. Shokrollahi, *Progress in Solid State Chemistry* **2012**, *40*, 6.

[39] Q. He, E. Arenholrz, A. Scholl, Y. H. Chu, R. Ramesh, *Current Opinion in Solid State and Materials Science* **2012**, *16*, 216.

[40] T. Zhao, A. Scholl, F. Zavaliche, K. Lee, M. Barry, A. Doran, M. P. Cruz, Y. H. Chu, C. Ederer, N. A. Spaldin, R. R. Das, D. M. Kim, H. Baek, C. B. Eom, R. Ramesh, *Nature Materials* **2006**, *5*, 823.

[41] F. Zavaliche, R. Ramesh, M. P. Cruz, R. R. Das, D. M. Kim, C. B. Eom, *Applied Physics Letters* **2005**, *87*, 252902.

[42] H. Bea, M. Bibes, A. Barthelemy, K. Bouzehouane, E. Jacquet, A. Khodan, J.-P. Contour, S. Fusil, F. Wyczisk, A. Forget, D. Lebeugle, D. Colson, M. Viret, *Applied Physics Letters* **2005**, *87*, 72503.

[43] C. Ederer, N. A. Spaldin, *Physical Review B* **2005**, *71*, 060401.

[44] D. Lebeugle, D. Colson, A. Forget, M. Viret, A. M. Bataille, A. Gukasov, *Physical Review Letters* **2008**, *100*, 227602.

[45] I. Sosnowska, T. P. Neumaier, E. Steichele, *Journal of Physics C: Solid State Physics* **1982**, *15*, 4835.

[46] T.-J. Park, C. Papaefthymiou, A. J. Viescas, A. R. Moodenbaugh, S. S. Wong, *Nano Letters* **2007**, *7*, 766.

[47] R. Mazumder, P. S. Devi, D. Bhattacharya, P. Choudhury, A. Sen, *Applied Physics Letters* **2007**, *91*, 062510.

[48] M. Daraktchiev, G. Catalan, J. F. Scott, *Ferroelectrics* **2008**, *375*, 122.

[49] J. Přívratská, V. Janovec, *Ferroelectrics* **1997**, *204*, 321.

[50] U. Gradmann, *Hyperfine Interactions* **1995**, *95*, 15.

[51] C. Pinettes, C. Lacroix, *Journal of Magnetism and Magnetic Materials* **1997**, *166*, 59.

[52] H. Schmidt, *Structure and Bonding* **1992**, *77*, 119.

[53] C. J. Brinker, G. C. Frye, A. J. Hurd, C. S. Ashley, *Thin Solid Films* **1991**, *201*, 97.

[54] S. M. Attia, J. Wang, G. M. Wu, J. Shen, J. H. Ma, *Journal of Materials Science & Technology* **2002**, *18*, 211.

[55] C. Sanchez, C. Boissiere, D. Grosso, C. Laberty, L. Nicole, *Chemistry of Materials* **2008**, *20*, 682.

[56] M. Faustini, B. Louis, P. A. Albouy, M. Kuemmel, D. Grosso, *Journal of Physical Chemistry C* **2010**, *114*, 7637.

[57] C. J. Brinker, Y. F. Lu, A. Sellinger, H. Y. Fan, *Advanced Materials* **1999**, *11*, 579.

[58] D. Grosso, F. Cagnol, G. Soler-Illia, E. L. Crepaldi, H. Amenitsch, A. Brunet-Bruneau, A. Bourgeois, C. Sanchez, *Advanced Functional Materials* **2004**, *14*, 309.

[59] M. Antonietti, B. Berton, C. Goltner, H. P. Hentze, *Advanced Materials* **1998**, *10*, 154.

[60] P. Ferreira, R. Z. Hou, A. Y. Wu, M. G. Willinger, P. M. Vilarinho, J. Mosa, C. Laberty-Robert, C. Boissiere, D. Grosso, C. Sanchez, *Langmuir* **2012**, *28*, 2944.

[61] G. Binnig, H. Rohrer, *IBM Journal of Research and Development* **1986**, *30*, 355.

[62] I. Amato, *Science* **1997**, *276*, 1982.

[63] D. M. Eigler, E. . Schweizer, *Nature* **1990**, *344*, 524.

[64] IBM Research, "Scanning Tunneling Microscope," can be found under http://www-03.ibm.com/ibm/history/ibm100/us/en/icons/nanotechnology/, **1990**.

[65] G. Binnig, C. F. Quate, C. Gerber, *Physical Review Letters* **1986**, *56*, 930.

[66] H. Birk, J. Glatzreichenbach, Lijie, E. Schreck, K. Dransfeld, *Journal of Vacuum Science & Technology B* **1991**, *9*, 1162.

[67] A. Gruverman, O. Auciello, H. Tokumoto, *Journal of Vaccum Science & Technology B* **1996**, *14*, 602.

[68] A. Gruverman, O. Auciello, H. Tokumoto, *Annual Review of Materials Science* **1998**, *28*, 101.

[69] E. Soergel, *Journal of Physics D: Applied Physics* **2011**, *44*, 464003.

[70] S. Kalilnin, A. Gruverman, *Scanning Probe Microscopy - Electrical and Electromechanical Phenomena at the Nanoscale*, **2007**.

[71] A. Kholkin, A. Gruverman, *Reports on Progress in Physics* **2006**, *69*, 2443.

[72] G. Catalan, H. Béa, S. Fusil, M. Bibes, P. Paruch, A. Barthélémy, J. F. Scott, *Physical Review Letters* **2008**, *100*, 27602.

[73] I. Coondoo, N. Panwar, A. Tomar, I. Bdikin, A. L. Kholkin, V. S. Puli, R. S. Katiyar, *Thin Solid Films* **2012**, *520*, 6493.

[74] F. Zavaliche, T. Zhao, H. Zheng, F. Straub, M. P. Cruz, P.-L. Yang, D. Hao, R. Ramesh, *Nano Letters* **2007**, *7*, 1586–1590.

[75] L. M. Bronstein, D. M. Chernyshov, G. I. Timofeeva, L. V Dubrovina, P. M. Valetsky, A. R. Khokhlov, *Langmuir* **1999**, *15*, 6195.

[76] F. I. Allen, P. Ercius, M. A. Modestino, R. A. Segalman, N. P. Balsara, A. M. Minor, *Micron* **2013**, *44*, 442.

[77] M. K. Singh, H. M. Jang, S. Ryu, M.-H. Jo, *Applied Physics Letters* **2006**, *88*, 42903.

[78] A. Z. Simoes, E. C. Aguiar, A. H. M. Gonzalez, J. Andres, E. Longo, J. A. Varela, *Journal of Applied Physics* **2008**, *104*, 104115.

[79] H. Fukumura, H. Harima, K. Kisoda, M. Tamada, Y. Noguchi, M. Miyayama, *Journal of Magnetism and Magnetic Materials* **2007**, *310*, 367.

[80] D. Kothari, V. Raghavendra Reddy, V. G. Sathe, A. Gupta, A. Banerjee, A. M. Awasthi, *Journal of Magnetism and Magnetic Materials* **2008**, *320*, 548.

[81] R. Palai, R. S. Katiyar, H. Schmid, P. Tissot, J. Clark, J. Robertson, S. A. T. Redfern, J. F. Scott, *Physical Review B* **2008**, *77*, 014110.

[82] G. L. Yuan, S. W. Or, H. L. W. Chan, Z. G. Liu, *Journal of Applied Physics* **2007**, *101*, 24104.